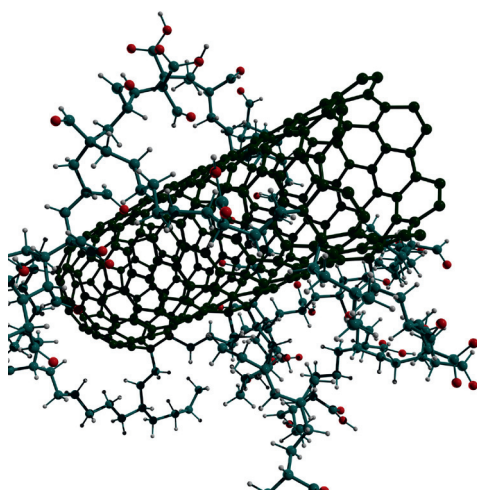L

A Spectroscopic Study of Polymer - Carbon Nanotube Composites
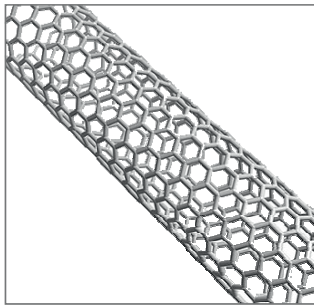

Andreas Müller

A spectroscopic study of
polymer - carbon nanotube composites

ANDREAS MÜLLER

"A new scientific truth does not triumph by convincing its opponents and making them see the light,

but rather because its opponents eventually die,

and a new generation grows up that is familiar with it."

Max Planck**,** 1920

Preface

The work presented in this Licentiate thesis has been carried out at Luleå University of Technology (LTU) in the Materials Physics group at the department of Engineering Sciences and Mathematics under supervision of Professor Alexander Soldatov.

I thank my supervisor at LTU, Professor Alexander Soldatov, for the subject, his patience and invaluable advice and support. Without all this, the presented work would not have been possible.

Further I would like to express my gratitude to Dr. Brigitte Vigolo and Prof. Edward McRae for pleasant discussions and all their contributions to the publications.

My lab colleague, Mattias Mases, I thank for his help, discussions and company.

I am very grateful to all the people and especially all the good friends who crossed my way during the years spent in Luleå and who made it an unforgettable time.

Finally, I would like to thank my family, my parents Gerda and Siegfried Müller and my sister Simone Müller for their support and making my studies possible.

Thank you!

Abstract

Since the identification of carbon nanotubes (CNTs) by Ijima in 1991, this material has become a subject of great interest and effort in science because of the outstanding physical properties it exhibits. CNTs can be thought of as graphene sheets rolled into seamless cylinders of various diameters and in principle infinite length. Depending on the number of concentrically arranged tubes, CNTs are termed single-walled (SWCNT), double-walled (DWCNT), and multi-walled (MWCNT) CNTs. Moreover SWCNTs exist as semiconducting or metallic types, depending on the orientation of the hexagonal lattice relative to the tube axis, as classified by the chiral indices (n, m). Their extraordinary mechanical, electrical, thermal, and optical properties render them very attractive for a wide range of applications including advanced composite materials. However synthesis of CNT-based composite materials still remains a big challenge. In particular it remains to overcome the difficulties in achieving good nanotubes dispersion within the matrix material. The fact that present synthesis routes produce SWCNTs in a bundled state due to van der Waals intertube interaction is another serious hurdle, as SWCNT bundles do not exhibit the excellent properties of their individual components. Thus special treatment has to be applied in order to break these bundles. In an ideal composite material, the individual SWCNTs would be homogeneously dispersed in the matrix. A second issue is the interaction between the CNTs and the host: to improve the load transfer between host and filler covalent linking between the two components is desirable. One approach to solve these problems is functionalization of the CNT source material prior to its incorporation into the polymer matrix. Optimization is required to maximize the transfer from the polymer to the CNTs but minimize the number of wall defects created by the covalent grafting of the functional groups on the CNT sidewalls. Moreover appropriate functional groups have to be chosen to assure compatibility with the polymer being used.

Synthesis of the polymethyl methacrylate (PMMA) composite material used here, based on functionalized SWCNTs, was reported recently and its study revealed inhomogeneities in the CNT distribution within the polymer and associated degradation in the mechanical properties suggested as being attributed to the presence of CNT agglomerates. Since Raman spectroscopy, as a mostly non-destructive analysis method, has proven to be a powerful tool for studying both pure CNT materials and CNT-based composites, it was used in this work along with supporting methods (scanning electron microscopy (SEM) and focused ion beam (FIB)) for extended characterization of the composite material, including analysis of the source SWCNT material before and after functionalization. Employment of different laser excitation energies (1.96eV and 2.33eV) allowed to separately probe metallic and semiconducting CNTs in the composite samples. The CNT distribution in the samples was illustrated by Raman spectral mapping of the G^+-peak intensity as a function of position, thus elucidating the presence of CNT agglomerates of different size and shape. At both photon energies, spectral line scans across the boundary regions were performed revealing a substantial drop in intensity of G^+ CNT

Raman mode and an increase of the D/G^+-intensity ratio. Examination of the D/G^+-intensity ratio of the SWCNT material before incorporation into the composite showed a higher value for functionalized than for the raw SWCNTs. Furthermore, the metallic nanotubes exhibited a higher degree of functionalization. Raman spectral imaging revealed some inhomogeneities of the CNT distribution in the composite material: the spectra of the areas with good CNT dispersion in the composite exhibit a higher D/G^+-intensity ratio than in areas with CNT agglomerates indicating that functionalized CNTs are preferentially dispersed in the polymer matrix while non functionalized ones tend to group together in agglomerates. Furthermore significant laser heating of the SWCNTs in composites has been revealed resulting in a downshift of the G^+-peak position which was much more pronounced in agglomerates than in the areas with dispersed CNTs and detected at the very lowest laser irradiances. SEM/FIB dual beam technique was employed as a supplementary analysis tool. The composites microstructure in CNT agglomerates as well as in the dispersed area was investigated by acquisition of SEM crossectional images confirming the different local CNT concentrations.

APPENDED PAPERS

Paper I

Multiscale Characterization of Single-Walled Carbon Nanotube/Polymer Composites by Coupling Raman and Brillouin Spectroscopy
B. Vigolo, B. Vincent, J. Eschbach, P. Bourson, J. F. Marêché, E. McRae, A. Müller, A. Soldatov, J. M. Hiver, D. Abdesselam and D. Rouxel
Journal of Physical Chemistry C **2009**, 113, 17648.

Paper II

Raman study of inhomogeneities in carbon nanotube distribution in CNT-PMMA composites
A. Mueller, B. Vigolo, E. McRae and A. Soldatov
Physica Status Solidi (b) **2010***, 247, 2810.

Paper III

Raman study of CNT – PMMA composites: some functionalization and thermal effects
A. Mueller, B. Vigolo, V. Mamane, Y. Fort, E. McRae and A. Soldatov
Submitted for publication to *Journal of Physical Chemistry C*.

TABLE OF CONTENTS

1. INTRODUCTION

Carbon nanotubes are, besides fullerenes and graphene, one of the nano-structured forms of carbon. First observations of multi-walled carbon nanotubes (MWCNT) date back to 1952, although not noticed by most of the scientific community at that time [1]. Almost 40 years had to pass untill S. Iijima published TEM images of the concentrically aranged carbon layers in MWCNTs and two years later discovered the existence of single-walled carbon nanotubes (SWCNTs) [2, 3]. The extraordinary structural and physical properties of CNTs in general and SWCNTs in particular, caused a great interest in scientific community and an "explosure" of research in the field worldwide.

SWCNTs were not only a perfect playground for fundamental science since they constitute in principle a one dimensional electrical conductor but have also been envisioned for a plethora of different applications. Due to their small diameters and either metallic or semi-conducting behavior, they are good candidates for future integrated circuits with molecule-sized components, field emission sources, molecular sensors and/or probes.

Furthermore, they have been regarded as the perfect filler materials for composites since they combine very good mechanical properties with high electrical and thermal conductivity. Although nowadays composite materials routinely used on an industrial scale and can be found in commercial products like hockey sticks or rotors of wind power plants, the full potential of CNTs in this area is yet to be reached. One of the biggest problems to overcome is poor dispersion of SWCNTs in the composite's matrix material since the former tend to agglomerate and stick to each other. Furthermore, once the CNTs are incorporated in the host material a strong interaction between the two is desired to maximize the new material's properties. One approach to address these problems is functionalization of the CNT source material prior to its incorporation to the composite. Thus the dispersion might be facilitated by attaching right functional groups to the CNTs' surface and, furthermore, the material can be strengthened via formation of covalent bonds between the CNT filler and the matrix..

Unfortunately, making a material is not the only job to be done. In order to improve a material step by step, structure – property relationships have to be investigated by the available analytical tools. With respect to carbon nanotubes Raman spectroscopy is nowadays maybe the most important technique since it is not only quick and requires comparatively easy sample preparation but also provides invaluable information about probed CNTs (for example, nanotube diameter) without need of expensive and more complicated methods like TEM.

In this work a composite material based on functionalized SWCNTs in a polymethyl methacrylate (PMMA) matrix has been investigated by Raman spectroscopy. Through our study particulary important questions for composite materials research were addressed - dispersion of the CNTs in PMMA and interaction between filler and matrix material.

1.1. THESIS OUTLINE

The first chapter of the thesis starts with a short overview of the structures of different allotropic modifications of carbon, namely diamond, graphite (graphene), fullerenes and carbon nanotubes with special emphasis on the latter. Physical properties of CNTs are reviewed and compared to other functional materials. The chapter continues with description of CNT synthesis methods, a general introduction to Raman spectroscopy and its application to CNTs and followed by presentation of composite materials based on carbon nanotubes.

Chapter 3 presents the CNT materials used in this study, the synthesis process of the composite material, and the Raman setup used for this work. The setup of a FIB/SEM system which was used for complementary experiments is briefly described.

It follows by the chapter *Results and discussion* which starts with description of the Raman investigation on the SWCNT source material followed by a comparison of Raman spectra of the studied SWCNT systems, namely, the as-produced SWCNTs (source material) before and after functionalization and different areas in the composite material. This is followed by presentation of an investigation of the SWCNTs' dispersion in the matrix and an analysis of the I_D/I_{G+} ratio to elucidate the role of functionalization. In the next part laser heating effects in the composite are discussed before concluding the chapter with a complementary FIB/SEM study. Finally a summary, conclusions and suggestions for future work are given.

2. THEORY AND LITERATURE OVERVIEW

2.1. CARBON AND ITS MANY FACES

After today's scientific knowledge carbon was not the first element formed after the big bang, that was hydrogen. Nevertheless, compared to all other elements of the periodic table, carbon occupies a special place in a sense that an entire subcategory of chemistry, the organic chemistry, deals only with its reactions and compounds. As expressed by the term "organic" chemistry, carbon is an elemental ingredient for all living species since it builds up the skeletal structure. Furthermore, carbon exists as an element in various allotropic modifications which exhibit completely different properties. Diamond is, for example, the hardest natural material known to mankind and carbon in this form as an electrical isolator and transparent for the visible light. Graphite, on the contrary, is a very good electrical conductor, black and often used as a solid lubricant. This wide variety of different forms with different properties is the reason that today carbon is present in all areas of everyday's life. It can be in form of hydrocarbons, in fuels or polymers, as graphite in pencils or as diamond in jewellery.

The following part will provide a short overview over the element carbon itself and its allotropic modifications.

The element carbon

Carbon is after hydrogen, helium and oxygen the fourth common element in the milky way and in our solar system where it can be found in stars, planets and stellar nebulae [4-6]. It is formed in most stars by nuclear synthesis out of 3 helium nuclei during the triple-alpha-process [7].

The earth consists of approximately 0.087 % of carbon. One can distinguish between inorganically bound carbon in the lithosphere (mostly in form of carbonates), hydrosphere (dissolved CO_2) and atmosphere (CO_2) and organic carbon in the biosphere. The relative ratios are as follows [8]:

Lithosphere	>	Hydrosphere	>	Atmosphere	>	Biosphere
100000		100		2		1

The modifications of carbon can be classified by the hybridization state of the carbon atoms in sp^3, sp^2 and sp (and hybridization states in between). Accordingly, the carbon atoms can form four, three or two bonds thus leading to the allotropic modifications described below.

2.1.1. *CARBON ALLOTROPES*

Diamond

The 3D- representative is well-known Diamond which consists of a 3D-network of sp^3-bonded carbon atoms (figure 1) with the result to be the hardest existing material. Besides, Diamond is highly heat conductive, a perfect isolator, transparent and because of its high optical density/refractive index causing many inner reflections of light inside a polished crystal the most wanted material for jewelry [4].
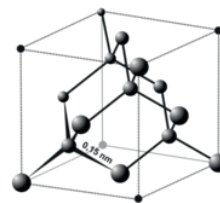

Figure 1. The unit cell of diamond.

Graphene

Graphene is strictly speaking one single layer of carbon atoms in a hexagonal honeycomb lattice and therefore the two dimensional form of carbon (figure 2). Thus every atom is bonded to three partners which results in a sp^2-hybridization. Although well known as a theoretical model, it was only in 2004 that graphene entered widely the experimental science when A. Geim und K. Novoselov discovered a cheap and simple way for the sample preparation [9]. However, it should also be mentioned that Boehm et al. synthesized graphene already in 1962 [10]. Several types of graphene are commonly distinguished in literature, those are single layer graphene (SGL), bilayer graphene (BLG) and few layer graphene (FLG, up to 9 graphene layers). Due to its electronic structure and low dimensionality graphene has a huge potential for future electronics [11].
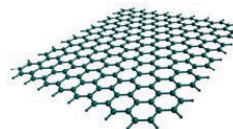
Figure 2.The structure of grapheme.
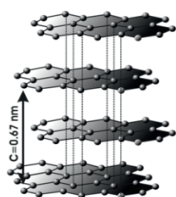
Graphite

Figure 3. The structure of graphite.

Graphite is quasi 2D-form of carbon with infinite number weakly bound 2D- graphene sheets stacked one upon the other (figure 3). Each planar graphene sheet is build out of hexagonally arranged carbon atoms. This structure makes it a solid lubricant since the individual sheets are only weakly held together and can slide relatively to each other in their plane. Furthermore that propriety and its black color makes is a perfect material to produce pencils. Besides graphite is unlike diamond electrically conductive [4].

Fullerenes

Buckminster Fullerenes, also called Buckyballs, are the 0D, modification of carbon. This molecular allotrope of carbon was experimentally discovered in the form of C_{60} buckyball in 1985 by H. W. Kroto, J. R. Heath, S. C. O'Brien, R. F. Curl and R. E. Smalley [12]. Fullerenes are hollow highly symmetric carbon-cage clusters build up from hexagonal and pentagonal rings. Incorporation of the latter ones results in the needed curvature. The smal-

Figure 4. Buckyball $C_{60.}$

lest stable fullerene, C_{60}, exhibits the same arrangement of the polyhedra as a football and is of less than one nanometer in diameter (figure 4). The carbon atoms in fullerenes have a mixed between sp^2 and sp^3 hybridization because each carbon atom on the "ball" is involved in formation both single and double bonds with the neighbours. Fullerenes can build a crystal and can even be polymerized under high pressure, excitation by electrons or photons or in a plasma discharge [13, 14].
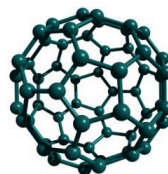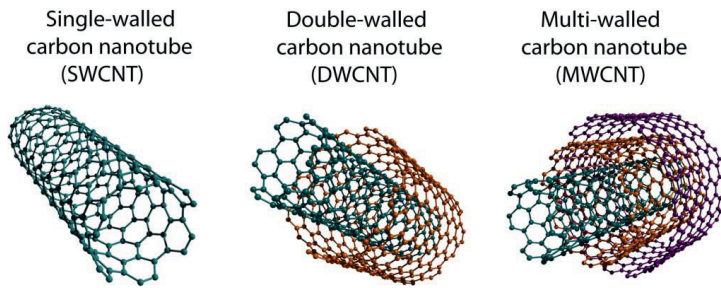
Carbon nanotubes

The first proof for the existence of carbon nanotubes was probably found by the two Russian scientists Radushkevich und Lukyanovich who published TEM images of MWCNTs in 1952 in the journal Physical Chemistry of Russia [1]. Over the next years several other works incorporated similar images, i.e. the works of Boehm or Oberlin and Endo [15, 16]. The latter ones described additionally the nowadays widely accepted growth model of CNTs. It is to assume that CNTs were generated routinely during research on carbon fibers but just not noted. Up to date the oldest CNTs were found in damascene swords [17]. However, it was not until 1991 that CNTs came into the focus of many scientists, initiated by a report of Iijima. And although he was not the first to image CNTs in general, he was the first showing single-walled CNTs [2, 3].

Those two works in combination with the anticipated possibilities for applications started what one could term the "Carbon nanotube hype". As a result a huge effort was undertaken by numerous scientific groups to uncover the secrets of the CNTs and put them into good use. Besides countless scientific articles CNTs reached nowadays the stage of industrial production, e.g. by the Bayer AG. First commercial applications are at the moment sports goods (snowboards, arrows, hockey sticks), AFM tips but also rotors for wind power plants [18-20]. Despite these achievements there remain questions to be answered and problems to be solved one of which is the chirality controlled synthesis of CNTs and another one how to fully exploit their unique properties in novel materials like composites.

2.1.2. *STRUCTURE AND PHYSICAL PROPERTIES OF CARBON NANOTUBES*

The structure of CNTs [21]

Carbon nanotubes can be considered as graphene sheets rolled into cylinders with diameter from less than one to some nanometers and caped at the ends with half-fullerenes. There are two types of carbon nanotubes one has to distinguish. Single-wall carbon nanotubes consist of only one tube whereas multi-wall carbon nanotubes consist of several tubes which are packed concentrically in each other. A special kind of those MWCNT is a double-wall carbon nanotube which is build of just two tubes (figure 5).

Figure 5. Different types of carbon nanotubes.

A graphene sheet which is rolled together into a nanotube consists of hexagonal arranged, sp^2-bonded carbon atoms. Figure 6 illustrates this idea.
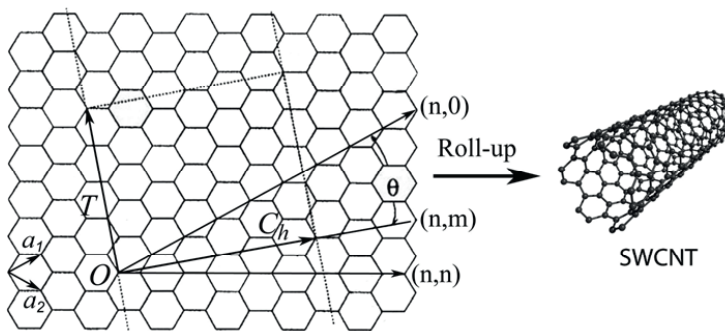
Figure 6. Scheme of a graphene sheet (with chiral vector C_h and chiral angle θ) which is subsequently rolled up to form a nanotubes.

The graphene sheet is rolled up along the chiral vector C_h which is expressed in the real space unit- vectors of the hexagonal lattice **a₁** and **a₂** and completely defines the nanotube's geometry (diameter, chirality).

$$C_h = na_1 + ma_2 \quad (1)$$

The angle between the chiral vector and the unit-vector a_1 is called the chiral angle θ and defined by the equation:

$$\cos(\theta) = \frac{C_h \cdot a_1}{|C_h| \cdot |a_1|} \quad (2)$$

The diameter of a CNT with chiral indices (n, m) can be calculated as follows:

$$d_t = a\sqrt{n^2 + m^2 + nm} \quad (3)$$

Depending on their chiral indices (n, m) carbon nanotubes are classified in three sub-groups. A (n, n) - nanotube is called an armchair tube. Its chiral angle, which is the angle between C_H and a_1, is 30°. The (n, 0)-configuration is called zigzag and exhibits an angle of 0°. All tubes with an angle in between and so with C_h(n, m) are chiral nanotubes. This nomenclature originates from the shape of a tubes' cross- sectional ring (figure 7). Because of the hexagonal symmetry there are no angles higher than 30°.
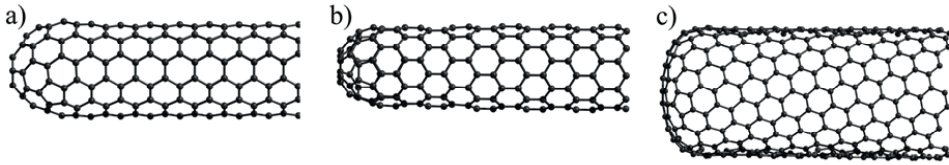
Figure 7. Classification of carbon nanotubes: a) armchair nanotube (n,n); b) zig-zag nanotube (n,0); c) chiral nanotube (n,m).

Table 1. Classification of carbon nanotubes.

Typ	θ	C_h	shape of crossection	
armchair	30°	(n,n)	⌒⌒⌒	cis-type
zig-zag	0°	(n,0)	∧∧∧∧	trans-type
chiral	0° < θ < 30°	(n,m)		mix of cis & trans

Carbon nanotubes can be semi-conductive or metallic depending on their chirality whereas metallic tubes obey the equation:

$$\frac{(2n + m)}{3} = Integer \quad (4)$$

Therefore two thirds of all CNTs are semiconductive and the other third metallic. Multi-wall carbon nanotubes are always metallic.

To provide an overview for the different chiralities of SWCNTs, a chirality map is commonly used (figure 8). Besides mapping the CNTs according their chiral indices (n, m) and diameters, it also assigns them metallic or semi-conducting character.
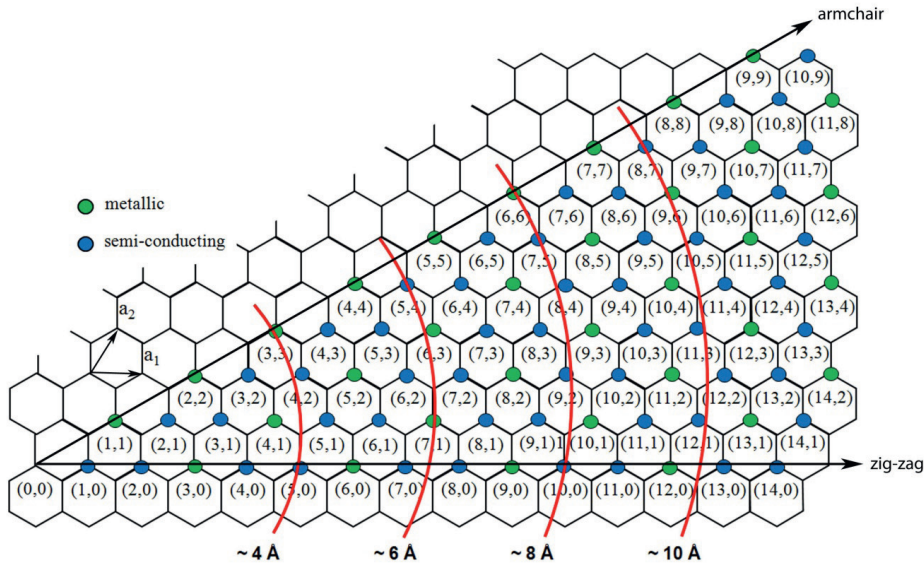
Figure 8. Chirality map of single-walled CNTs. Red lines serve as guide for the eye and cut CNTs of different chiral indices but of almost the same diameter.

CNTs can be closed by so-called end-caps (in principle half-fullerenes) on one side. The other side is often attached to either the catalyst particles or a substrate, unless special purification treatments are performed.

Mechanical properties [22]

Carbon nanotubes exhibit extremely small diameters down to about 1nm and up to tens of nm for multi-wall CNTs. Their length can be smaller than 1μm but CNTs with length of several mm were reported. Therefore CNTs have possible aspect ratios over 10000 (a human hair with that aspect ratio and a diameter of 70 μm would have a length of 70 cm) which is one reason why they are so attractive for use of fillers in composite materials.

On the mechanical side carbon nanotubes exhibit extraordinary properties though they can slightly change from SWNTs to MWNTs. For example an elastic modulus in the order of 1 TPa which is five times the value of steel which is around 210 GPa were both obtained from numerical calculations and various experimental tests [22]. The tensile strength of MWNT was tested to be up to 63 GPa but there are papers estimating even values up to 150 GPa [22]. With a density of 1.3 – 1.4 g/cm^3 [22] carbon nanotubes exhibit a specific strength of 48,5kN m/kg. Thus carbon nanotubes are the only material

which could for example be used for cables for an elevator from earth to space [13]. The reason for these extraordinary mechanical properties is the atomic structure which is build off covalent C-C bonds.

The following table gives some numbers of different CNT types and also of some commercial fibers for comparison.

Table 2. Mechanical and structural properties of different CNT types and some functional materials [22].

	SWNT	DWNT	MWNT	Carbon fiber	Steel	Kevlar
Young's modulus [GPa]	640		1060	150 - 950	190 - 210	130
Tensile strength [GPa]		23 - 63	63	4-7	0,5 - 2	3 - 4
Density [g/cm^3]	1,3 – 1,5	1,5	1,8 - 2	1,7 – 2,2	7,75 – 8,1	1,44
Diameter[nm]	ca . 1	ca. 5	ca. 20	60 – 100		>5000

Electrical properties

Because of their one- dimensional shape and their symmetry nanotubes exhibit a very particular electronic structure. Dependent on their chiral vector C_H they can be semi-conducting or metallic. If n-m is a multiple of 3 for an (n,m)- nanotube, this tube is metallic, if not it is semi-conductive. Very high current densities of about 10^6 A/cm^2 (even $6 \cdot 10^6$ for metallic tubes) were reached in carbon nanotubes due to nearly ballistic (low scattering) propagation of charge in these quasi-one dimensional systems [22].

The following table gives some numbers of CNTs and also of the two best metal conductors for comparison.

Table 3. Electrical conductivity of different CNT forms and other good electrical conductors [22].

	Individual or bundled CNTs	CNT films or fibers	Silver	Copper
el. conductivity [S/m]	10^6	10^4 - 10^5	59.6×10^6	63.01×10^6

Thermal properties

Due to their large aspect ratio and strong sp^2 carbon bonds carbon nanotubes are expected to be very good heat conductors along their axis due to "ballistic" phonon flow (in analogy to the electric current/charge flow) but are insulators in their radial direction. It

is estimated that nanotubes are able to transmit up to 6600 W/K/m at room temperature thus being even better heat conductors than diamond! Carbon nanotubes have an estimated temperature stability up to 2800°C in vacuum and 750°C in air [22].

The following table contains data on thermal conductivity of CNTs, diamond and also some other good thermal conductors for comparison (table 4).

Table 4. Thermal conductivity of different CNT types and other materials [22].

	SWCNT	MWCNT	Carbon fibers	Silver	Copper
therm. conductivity [W/mK]	6600 (theor.)	3000 (exp.)	8 - 1100	429	401

2.2. CNT SYNTHESIS METHODS [21, 22]

While MWCNTs can be synthesized without the use of catalysts (using the arc discharge method), the formation of SWNTs necessitates the presence of catalytically active nano-particles. The latter ones are commonly transition metals like Fe, Co or Ni or mixtures of them like Ni/Y, Co/Mo or Fe/Ru. As carbon feedstock either a solid carbon source is used as for arc discharge and laser ablation or carbonaceous gases, e.g. CO, EtOH or Acetylene as in the case of chemical vapor deposition approaches. The three most widely used synthesis methods are:

2.2.1. ARC DISCHARGE

Two catalyst loaded or doped graphite rods, acting as well as electrodes, are vaporized by an electric arc which is formed between them. Whereas the anode is consumed during the process a deposit containing SWCNTs is formed on the cathode. SWCNTs are also found in the deposit in the reactor chamber. Arc discharge is a high temperature process with carbon evaporation temperatures of 4000-5000 K.

2.2.2. LASER ABLATION

For the laser ablation technique a graphite rod loaded with a metal catalyst is used as well. In contrast to the arc discharge method the carbon is vaporized by strong laser irradiation. The resulting SWCNTs are trapped by a cold trap. To obtain higher yields the ablation process takes place in a heated oven.

2.2.3. CHEMICAL VAPOR DEPOSITION

The CVD method relies on the decomposition of carbonaceous gases on catalytic nano-particles. The catalyst particles are either formed during the process or can be synthesized in a separate procedure. Since the CVD method allows for a superior control of the synthesis conditions as growth temperature, carbon supply rate, catalyst particle size and also allows for patterned substrates more control over the produced CNTs is possible.

However all current synthesis techniques always yield a mixture of diameters and chiralities and therefore metallic and semi-conducting SWCNTs.

2.3. RAMAN CHARACTERIZATION OF CNTS

As carbon nanotubes have dimensions in the order of nanometers special analysis methods have to be applied to study such materials. Many different techniques are presently used in carbon nanotube research, namely imaging methods like SEM, FIB, TEM, AFM, STM and spectroscopic methods like photoluminescence, infrared, near-infrared and Raman spectroscopy. The latter will shortly be introduced on the following pages.

2.3.1. RAMAN SPECTROSCOPY: METHOD OVERVIEW

In this work the main technique for the study of CNT - composites, was Resonant Raman Spectroscopy. It provides much information about an investigated system, does not need a complex sample preparation and is a relative fast technique.

Theory [23, 24]

Raman spectroscopy is named after its inventor or perhaps discoverer, as it is based on a physical phenomenon, Sir Chandrasekhra Venkata Raman who discovered this phenomenon in 1928 [25].
Shortly explained Raman Spectroscopy is the study of vibrational, rotational and other low-frequency modes in a system excited by an external energy source (usually a laser). It relies on inelastic scattering of the incoming photons which interact with the material under investigation. Specifically, the incident photons excite molecules in the material into a virtual energy state with extremely short lifetime thus the molecules almost instantaneously relax back to the "normal" energy level with emission of a photon. The emitted photon can have either a lower frequency thus the molecule ends up in a *higher* energy state, i.e. phonon is created by the photon (Raman Stokes process/scattering), or a higher frequency, i.e. the molecule ends up in a *lower* energy state, i.e. phonon is absorbed by the photon (Raman Anti-Stokes process/scattering). The frequency shift/energy difference between the incident and scattered photon is called Raman shift and is characteristic for a given material. Probability of the Raman processes is extremely low (10^{-6}) thus the major part of the photons scatter elastically, i.e. their energy does not change (Rayleigh scattering). Figure 9 gives a schematic idea of the basic mechanisms involved. Since the Raman phenomenon is very weak it is difficult to obtain good Raman spectra.
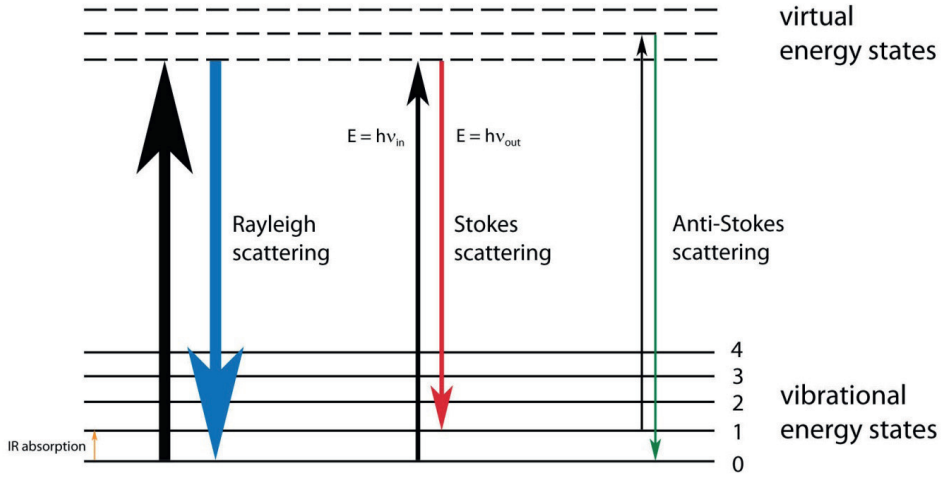
Figure 9. Energy level diagram showing the Raman processes. Line thickness indicates qualitatively the probability of different processes.

Since the Anti-Stokes photons will have higher energy than the incident photon, the corresponding peak in the Raman spectrum will appear on the left hand side of the Rayleigh scattering peak (negative energy shift) while the Stokes peak will be on the right hand side (positive energy shift). The Stokes peak intensity is higher than that of the correspondent Anti-Stokes peak as the number of molecules in the ground state determining the Stokes processes will normally be bigger than thermally excited which govern the Anti-Stokes processes. By comparing the relative intensities of Stokes and Anti-Stokes signal at different experimental conditions it is possible to determine the temperature of the molecules (material under investigation). If temperature rises sufficiently high the Anti-Stokes signal intensity may even exceed the Stokes signal.

The Raman signal intensity can be described by the following equation:

$$I_R = \frac{2^4 \cdot \pi^3}{45 \cdot 3^2 \cdot c^4} \cdot \frac{hI_L N (v_0 - v)^4}{\mu v (1 - e^{-hv/kT})} \cdot [45(\alpha_a)^2 - (\gamma_a)^2] = \frac{C_h \cdot a_1}{|C_h| \cdot |a_1|} \tag{4}$$

c   = speed of light
h   = Planck's constant
I_L = excitation intensity
N   = number of scattering molecules
v   = molecular vibrational frequency (hertz)
v_0 = laser excitation frequency (hertz)
μ   = reduced mass of the vibrating atoms
k   = Boltzmann's constant
T   = absolute temperature
α_a = mean value invariant of the polarizability tensor
γ_a = anisotropy invariant of the polarizability tensor

13

A typical Raman spectrum is shown in (figure 10) exhibiting Stokes, Anti-Stokes peaks with their relative shifts with respect to the laser (Rayleigh) line - a peak with the zero Raman shift, i.e. having the same wavelength as the exciting (incident) photons.
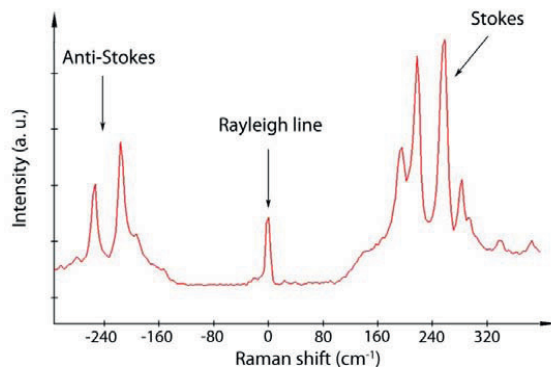
Figure 10. Raman spectrum showing Stokes, Anti-Stokes and Rayleigh signal.

It is important to note that the Raman intensity is proportional to the number of scattering molecules and thus the concentration of the scatterers in the illuminated volume.

Number of molecules ↗ → Raman intensity ↗

However one should be aware that in order to obtain quantitative information about the concentration of Raman scatterers a calibration of the Raman cross-section of the material under investigation has to be performed.

Furthermore, peak - intensities should be normalized to an internal standard when compared with each other. Raman spectra of carbon nanotubes are commonly normalized to the maximum intensity of the G-band (see further in the text) which has usually the highest intensity in a Raman spectrum of CNTs.

2.3.2. RESONANCE RAMAN SPECTROSCOPY OF CARBON NANOTUBES

If the photon energy of the excitation source matches a specific electronic transition energy of the molecule to investigate, the excited energy state of the molecule is not virtual but a real excited electronic state, unlike for normal Raman spectroscopy. Thus the vibrational modes associated with that transition exhibit a greatly increased Raman scattering intensity. This process is called resonance Raman (RR). Resonant Raman spectroscopy is based on this phenomenon and has an advantage of orders of magnitude signal increase. In case of carbon nanotubes we can achieve the RR regime if laser excitation energy will match that of the electronic transition energy (difference in electronic energy levels) of CNTs. A so-called Kataura plot (figure 11) exhibits the electronic transition energies of different nanotube species (n,m) dependence on their diameter [26].
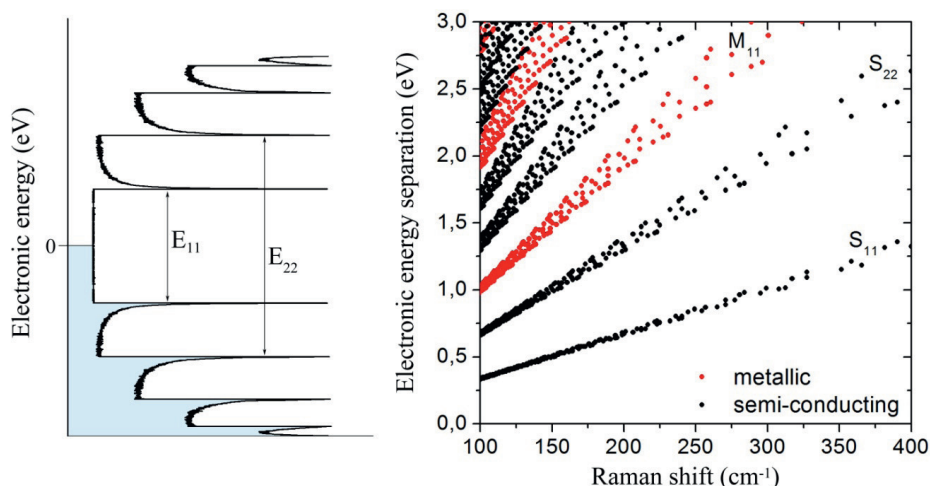
Figure 11. Left: Example for the 1D DOS of a metallic single-walled CNT. „First" and „second" van Hove transitions E_{11} and E_{22} are marked. Right: Kataura plot of van Hove transition energies of different types of SWCNTs relative to their RBM frequencies. Both graphics are based on freely accessible data from reference 27.

Figure 12 shows a typical resonant Raman spectrum of semiconducting carbon nanotubes. There are 3 regions of special importance:

The so-called G band is situated in the spectral region around 1600 rel. cm^{-1}. It is due to atomic vibrations in axial and circumferential tube direction. It is often used for scaling and normalization. The G-band is usually composed of two peaks. One caled G^+ which stands for tangential vibrations (highest peak on the right side of the G-band) and G^- corresponding to axial vibrations (lower peak on the left). While the G^+-peak has always a lorentzian shape the G^--peak is either a lorentzian for semi-conducting tubes or has a

so-called Breit-Wigner-Fano-shape. The G-band position does not depend on the incident laser wavelength.
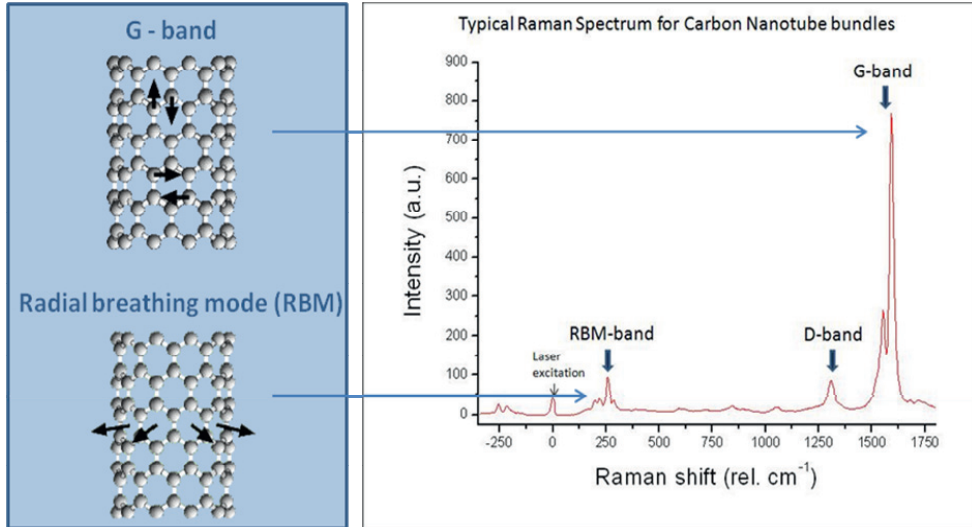
Figure 12. Resonant Raman Spectrum of carbon nanotubes (right panel) with corresponding atomic vibrations (left panel).

The D-band appears in the spectral region around 1330 rel. cm^{-1}. It is due to defects in the tube surface. Thus it is possible to determine whether a special treatment damages or alters the surface of nanotubes by studying the D-band. Further the D-band position depends on photon energy of the incident light where it shows downshifts with decreasing photon energy.

In the spectral region around 100 – 450 rel. cm^{-1} one can see the band due to the radial breathing mode (RBM). The radial breathing mode is due to atomic vibrations in radial tube direction and its frequency is diameter dependent. Specifically, a RBM peak at frequency ω_{RBM} is related to the tube's diameter d according to the following equation:

$$\omega_{RBM} = \alpha/d_t + \beta \qquad (5)$$

where α and β are empirical parameters. This equation also takes into account interactions between CNTs in the bundle [28, 29]. Therefore in case of many nanotubes contributing simultaneously to the Raman spectrum, for example CNT bundles, the RBM-band is comprised of the signal from the tubes with different diameters where the RBM peaks from the large diameter tubes are situated at lower relative wavenumbers/lower frequency and from the smaller diameter tubes at higher relative wavenumbers/frequencies. As it is resonant Raman spectroscopy one can never probe

all the tubes present in the sample but only those which are in resonance with the used excitation source (laser).

By selecting a laser excitation wavelength, corresponding to certain electronic transitions, it is then possible to probe nanotube species of interest in a sample and from their RBM spectra to assign their chiral indices (n,m)/determine their molecular structure. For example, it is possible to probe only semi-conducting nanotubes or metallic ones. For more information about the assignment of chiral indices see reference [30].

Different effects on Raman spectra of carbon nanotubes

Pressure and strain effects

If carbon nanotubes are exposed to pressure or strain the bond lengths and angles change resulting in a change of the phonon frequencies. Translated to the Raman spectra of CNTs this means that for increasing pressure the RBM-band as well as the G-band shift towards higher frequencies. Larger diameter tubes are more affected than smaller diameter ones [31, 32].

Besides pressure, CNTs are very sensitive to an applied uniaxial strain via perturbation of the electronic structure of CNTs – the D-, G- and G'-bands upshift on contraction (similar to high-pressure effect) and downshift under tensile uniaxial strain. Specifically, a downshift of > 2 cm^{-1} for tensile strain rates of 0.06 % whereas the shift can be as high as 40 cm^{-1} for 1.6 % strain. In contrary, the RBM frequency was found independent on applied strain whereas its intensity has been found to change drastically with uniaxial strain which has been attributed to a change in the resonance conditions due to altering electronic transition energies [33].

Chemical doping effects

Like pressure or strain, chemical doping of CNTs can be deduced from Raman spectroscopy experiments on single-walled carbon nanotubes. In contrast to the above mentioned effects (pressure and strain) which distort the CNTs' lattice directly, influence of chemical doping is a little bit more complicated. Depending on the doping species electrons are transferred to the CNT (*n* doping) or "sucked out" of it (*p* doping). The former can be achieved using, for example, alkali metals (Rb, Cs), the latter – by using halogens (Br$_2$) as dopants, respectively. While for low doping levels an upshift of the G-band is observed for both kinds of doping, higher doping levels lead to a downshift in the case of *n* doping and an upshift in the case of *p* doping [34, 35].

Temperature effects

Spectral features of Raman spectra of carbon nanotubes demonstrate also dependence on temperature [36-40].

For nanotubes unperturbed by surrounding environment it has been shown that the observed temperature dependence of the RBM fequency ω_{RBM} is mostly due to a softening of the intratubular carbon-carbon bonds. In case of CNT bundles an additional contribution of equal magnitude stemming from softening of intertube (van der Waals) interactions has to be taken into account. In contrast, thermal expansion of the CNTs adds only a little [36]. Consequently, the CNT environment is of significant importance for the temperature dependent behavior of the Raman spectra. While for as-grown suspended CNTs only bond softening contributes to the temperature dependence [37] this is not the case for individual CNTs dispersed by the aid of a surfactant. In the latter case the expansion of the CNTs surrounding will result in a pressure exerted on the surfactant-embedded CNTs, i.e. upshift of G-band, counteracting the temperature effect (downshift of G-band) [39, 40]. The following empirical equation relating temperature differences to spectral peak shifts of the G^+ band has been established experimentally [37]:

$$\Delta T = \Delta\omega(G^+)/-0{,}0258 \qquad [K]=[cm^{-1}]/([cm^{-1}]/[K]) \qquad (6)$$

Temperature also affects the intensity of the RBM Raman mode of CNTs due to changes in the resonance Raman conditions. The reason is shifts of the van Hove singularities in the CNT electronic density of states (DOS) resulting in changes of the transition energies E_{ii}. As in the case of G-band for RBM frequency shifts two scenarios have to be considered. CNTs in a certain environment feel temperature induced pressure effect in addition to the expected "pure temperature" RBM shift. - A surfactant expands and exerts an increased pressure on the coated CNTs while a CNT in a bundle will be exposed to reduced pressure due to a softening of the intertube interactions.

Laser irradiation effects

As evidenced by the resonant Raman effect of CNTs itself, CNTs can absorb incident radiation energy efficiently. Since not all of the absorbed energy is reemitted (what gives the Raman signal for example), the rest goes into CNT phonons causing heating effects. Experiments have shown that even suspended CNTs cannot dissipate this additional energy quick enough to avoid heating (evidenced by temperature induced downshifts of the G-band) [41]. Moreover, by using the resonance effect it is possible to preferentially heat tubes selected by the laser excitation frequency. In combination with high laser fluences and oxygen containing atmosphere the excited CNTs can be damaged and even destroyed [42, 43].

The CNTs environment plays one more time a crucial role here - individual CNTs which were placed on a surface acting as a heat sink showed less laser heating than freely suspended CNTs. CNT bundles proved more prone to laser heating than individual tubes

since in that case only a minority of the tubes has contact with the thermally conducting substrate while the remaining tubes are "insulated" by the other heat absorbing CNTs in the bundle.

Since laser heating effects may in principle accompany any Raman measurement on CNTs they can lead to obscuring or enhancing other effects (pressure, charge transfer, temperature) and should therefore always be considered in Raman experiments on nanotubes.

2.4. FUNCTIONALIZATION OF CARBON NANOTUBES AND CNT BASED COMPOSITES

2.4.1. GENERAL ASPECTS

A composite material or short composite is a natural or engineered material combining the different physical or chemical properties of two or more constituent materials aiming to enhance a specific ensemble of properties in the composite for special applications. A composite usually consists of a matrix material (e.g. polymer, metal or ceramic) which provides the bulk and the basic properties. The second ingredient, equally important, is the filler material, e.g. particles, fibers, meshes or woven mats. The filler exhibits superior characteristics, compared to the matrix material, for the property which is intended to be augmented. Apart from the individual characteristics of the two constituent materials at least two more factors are essential for making a good composite. The first is the dispersion or distribution of the filler in the matrix material, the second one being the interplay between them.

As mentioned before composite materials are one of the most promising fields for the application of carbon nanotubes (CNTs) because their unique structure and extraordinary mechanical, electrical and thermal properties suggest them to be the perfect filler material [44-48]. Among CNTs, single-walled carbon nanotubes (SWCNTs) occupy a special position. Consisting of just one graphene sheet rolled into a seamless tube, their diameters range from a few to less than one nanometer, and this results in very high aspect ratios and truly one-dimensional (1D) electronic character. Although there are many studies reporting significant improvement of various properties of composite systems fabricated by CNT incorporation, the full potential of CNTs has still not been reliably and reproducibly attained [44-48].

Two problems in particular arise during the synthesis of CNT-based composites which must be overcome. Firstly, the dispersion of the filler within many matrixes is still a challenge since SWCNTs form bundles due to strong van der Waals attraction and the bundles themselves tend to agglomerate even further. Homogeneously dispersed SWCNTs within the composite are essential in order to maximally benefit from their presence, be it electrical conductivity which necessitates a percolated network of the CNTs or improved mechanical properties for which a high matrix-CNT interface is required. A second issue is the interactions between the CNTs and the host matrix. For optimal load transfer between host and filler, covalent linking between the two components is desirable. However optimization is required to both maximize the load transfer from polymer to CNTs and minimize the number of wall defects created by the covalent grafting of the functional groups on the CNT sidewalls. Optimization is further required as concerns the choice of the functional group to make it compatible with the polymer being used [44-48].

One approach to solve these two problems is functionalization of the CNT source material prior to incorporation into the host [44, 45, 47, 49]. Roy et al. reported, for

instance, an increased load transfer by the use of CNT grafting by collagen which resulted in a greater critical shear stress [50]. Others prepared carboxylic functionalized MWCNT/polyimide composites reporting much better CNT dispersion and CNT-matrix interaction, both reflected in improved mechnical properties [51, 52]. In spite of these works which do indeed indicate some improved mechanical characteristics linked to the presence of the CNTs, the two above-mentioned difficulties are still serious hurdles to be overcome in a predictable and controlled manner.

2.4.2. APPLICATION OF RAMAN SPECTROSCOPY AS CHARACTERIZATION TOOL

For characterization of CNT-based composite systems, Raman spectroscopy is an analysis technique of interest since it requires only little or no sample preparation and may be non destructive. Moreover, Raman spectroscopy has been, and still is, extensively used to study different effects on pristine CNTs, such as those of functionalization[51, 53, 54] or of debundling treatments[55], temperature effects[36, 37, 41] as well as pressure or strain effects [31-33]. This knowledge of CNTs may be exploited in analyzing composite systems incorporating CNTs. Several research groups have employed Raman spectroscopy to measure interfacial shear strength and load transfer[50, 56-58] or to analyze doping by the matrix of the CNT fillers[59] while others have investigated the physical state of the CNTs, e.g. their structural integrity[60] after incorporation, the dispersion behavior[56, 61, 62], CNT orientation[63] or the CNT interaction with the matrix material [64].

2.4.3. LASER HEATING EFFECTS

As just pointed out Raman spectroscopy is of much value for the characterization of CNT based composites. Commonly, the spectral positions of one of the CNT Raman features, e.g. the G-band or D-band, which are known to be sensitive to outer influences (e.g. pressure, strain, charge transfer, temperature), are used for such studies [50, 56, 58, 61, 63, 65]. However, the spectral positions of the CNT Raman modes are also known to be sensitive to incident laser power density due to heating effects what can seriously complicate interpretation of Raman results [40, 41, 66]. Kao et al.[65] did report on laser heating of SWCNTs in an epoxy incorporating non-functionalized SWCNTs, showing more pronounced laser heating for the raw SWCNTs powder sample than for the SWCNTs incorporated in the CNT-epoxy resin composite. Apart from this study very little information of the laser heating effects in composite materials is available in the literature to date.

3. MATERIALS AND METHODS

3.1. CARBON NANOTUBE SOURCE MATERIALS

The SWNTs used for manufacturing the composites in this work were synthesized by the arc-discharge method (Carbolex Inc). The CNTs were used as-received (raw material) for the subsequent functionalization steps. The CNT raw material is from now on termed "as-produced" CNT/sample.

CNT functionalization was performed in a 3-step procedure (figure 13). On the first step methoxyphenyl groups were attached to the SWCNT surface following a free radical procedure leading to a low level of grafting (about 1 function per 70-100 carbon atoms) [67]. The obtained functionalized samples are termed from now on "SWCNT-PhOMe" or "functioanlized CNTs/sample. Subsequently the methoxyphenyl groups were modified using two steps in order to obtain SWCNTs grafted by phenolic ester groups (SWNT-PhEster) which are polymerizable and thus able to act as bridges between the SWCNT surface and the PMMA matrix. For Raman studies, functionalized CNTs after the first functionalization step were used. However, it has previously been found that the two additional steps affect only the end groups of the initially-grafted functions and do not have any further effect on the CNTs surface structure [68].
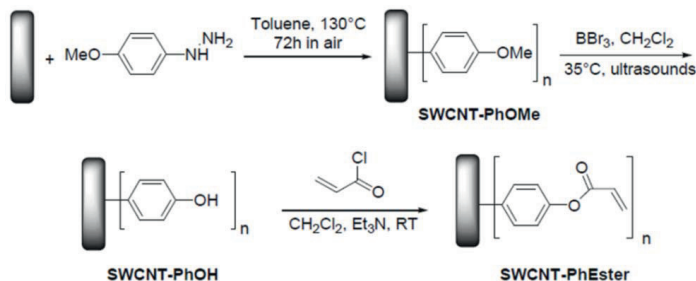

Figure 13. Functionalization procedure.

3.2. SWCNT-PMMA COMPOSITE MATERIAL

For the composite synthesis, the desired quantity of functionalized SWCNTs was dispersed in a MMA solution and radical polymerisation was directly initiated using benzoyl peroxide as initiator leading to PMMA. For homogeneization, the mixture was gently sonicated using a probe tip sonicator before polymerization initiation. The CNT concentration in the PMMA composite ranges from 0.013 to 0.6 wt% [67]. Both the functionalized CNTs as well as the composites were provided by our collaborators.

3.3. SPECTROSCOPIC CHARACTERIZATION (RAMAN)

Confocal Raman imaging system WiTec CRM 200

For all Raman measurements in this study we used a WiTec CRM 200 scanning confocal Raman/fluorescence microscope in backscattering geometry (figure 14). The system is equipped with a high quantum efficiency CCD detector for Raman spectra collection and an avalanche photo diode (APD) for fast Raman imaging. Three diffraction gratings with 150, 600 and 1800 groves/mm are available providing a spectral resolution up to 1 cm^{-1} (with the 1800 grating). The sample is placed on a two-axis piezo-table allowing for a scanning resolution of 2 nm.
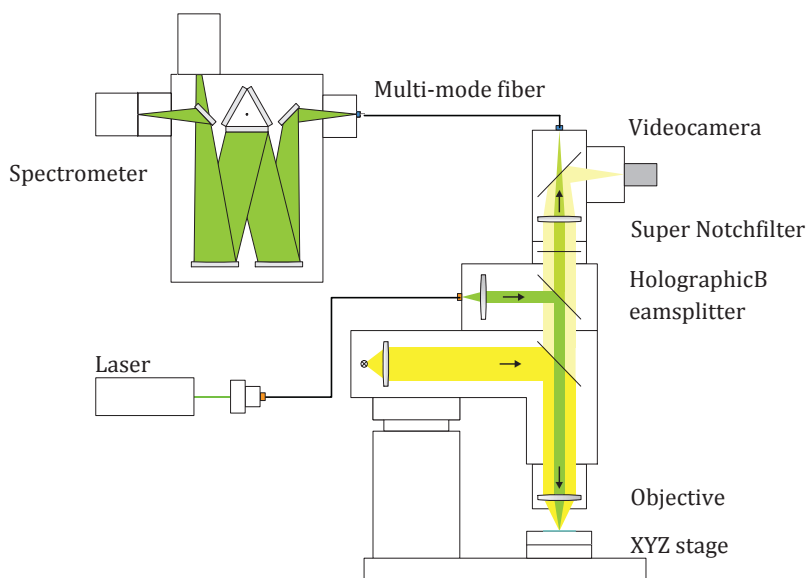
Figure 14. A schematic presentation of the CRM 200 system used in Raman experiments.

Excitation source

Two different lasers, a diode-pumped solid state (DPSS) laser with a wavelength of 532 nm and a HeNe laser with a wavelength of 633 nm (corresponding to 2.33 eV and 1.96 eV, respectively) were used in this work in order to preferentially probe semiconducting or metallic SWCNTs and thus be able to distinguish any different behavior due to the electronic structure of the nanotubes. In the experiments the laser power was measured directly on the microscope sample stage using LaserCheck, a portable power meter from Coherent.

Data acquisition modes

Three different spectral acquisition techniques provided by the WiTec software were applied in this work. The *single spectrum* technique was applied to collect a spectrum of a single spot on the sample. This mode was also used to perform line scans which will be explained in more detail further in the text.

The *image spectrum* technique takes several single spectra from an initially defined area. The resolution as well as the integration time for each single spectrum can be specified. As a result no spectral information is lost and the whole set of spectra can be further processed with different software filters producing plot of various spectral features. Typical measurement parameters were as follows.

Scanned area: 186 x 186 µm2   24 x 24 pixels/spectra

The *fast imaging* technique works similarly to the image spectrum technique with the important difference that only the signal of a specific pre-set wavelength which has to be set initially is collected. As a result a two dimensional graph plotting Raman intensity only at the specified wavelength is obtained. Scanning times can however be greatly reduced.

Scanned area: 186 x 186 µm2   24 x 24 pixels

3.4. FIB/SEM DUAL BEAM WORKSTATION

A focused ion beam dual-beam workstation is a combination of a focused ion beam (FIB) and a scanning electron microscope (SEM) which makes it possible to work on nanometer scale and, at the same instant, observe the operations performed by the FIB with the SEM. All basic characterisation abilities of a SEM and manipulation abilities of a FIB are included. Such a dual beam workstation is shown in figure 15.

Typical parts of the FIB instrument are a vacuum system, liquid metal ion source, ion column, stage, detectors, gas inlets, and computer with operation software. The ions (Ga^+-ions in the device implementation we used) are provided by the liquid metal ion source and are focused in the ion column which enables high lateral resolution and current density for the accurate manipulations. A motorized and highly flexible sample stage allows changing incident beam angle and position of the sample easily.
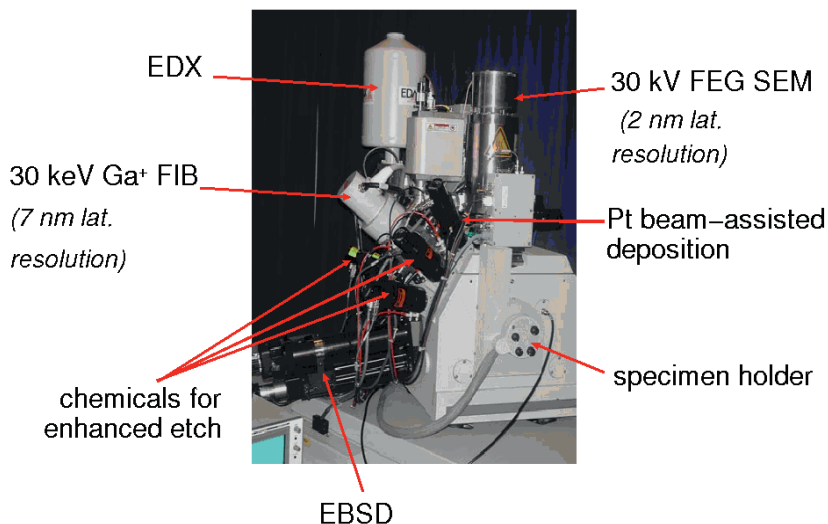
Figure 15. FEI Strata 235 Dual Beam FIB of the National Center for Electron Microscopy (NCEM), USA.

A FIB can locally etch the sample surface with submicron precision. Many variables and material properties affect the sputtering rate of the sample [69]. These include beam current (higher current remove more material), sample density, sample atomic mass, and incoming ion mass. The second application of FIB involving the gas precursor is the ion beam assisted material deposition of either conductive or insulator material on the sample surface on the very small scale. As for the SEM unit, the limitation for using this technique in CNT studies is the resolution which is approximately 3nm which is insufficient for the visualization of the individual SWNTs. Still it is possible to see SWNT bundles or MWNTs.

4. RESULTS AND DISCUSSION

The incorporation of carbon nanotubes in a host material, i.e. making a composite, usually results in improving mechanical, electrical or thermal properties of the host. As presented earlier (section 2.4.) it is imperative to achieve a good dispersion of the filler (CNTs in this case) in the composite. Moreover, if the mechanical properties of the matrix material are expected to benefit from incorporation of the CNTs, it is important to achieve strong interactions or even covalent linkage between the CNTs and the matrix in order to fully exploit the outstanding mechanical properties of the CNTs. A promising approach in this regard is functionalization of the CNT material prior to its incorporation into the matrix. The composite material of interest was manufactured from arc-discharge produced single-walled CNTs which were modified by a 3-step procedure (section 3.1.) before the SWCNT-PMMA composite was synthesized by radical polymerisation (section 3.2.). Unexpectedly, it was found that the mechanical properties were worsened comparing to pure PMMA .

This work was intended to explore the capability of Raman spectroscopy in terms of characterization of a CNT-based composite material, in particular with respect to the general distribution of CNTs in the composite, any differences between the distribution of functionalized and non-functionalized tubes and interaction between CNTs and matrix. FIB was used as a complementary tool for the investigation of the CNTs dispersion.

All studies were carried out on the as-produced CNT material (before functionalization), functionalized CNT material after the first functionalization step and, finally, on the composite. It should be mentioned that in the first functionalization step the side groups are attached to the CNTs surface. Subsequent steps only change the already attached side groups but do not alter the CNTs surface any further.

Most experiments were carried out with two laser excitations, 1.96 eV and 2.33 eV in order to independently probe metallic and semi-conducting tubes to detect potential differences in the CNTs behavior due to their different electronic structure.

4.1. RAMAN STUDY

4.1.1. CARBOLEX ARC-DISCHARGE CNTS

Raman scattering of carbon nanotubes is a resonance-enhanced process (section 2.3.2.), thus different CNT types can be probed via selection of laser excitation energies. In order to determine what kinds of SWCNTs are probed by two available laser energies, 1.96eV and 2.33eV, Raman spectra of the as-produced CNTs were acquired (figure 16) and correlated with the Kataura plot (figure 17).
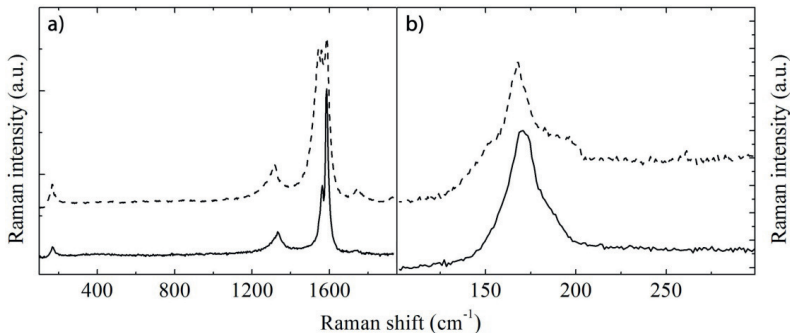
Figure 16. Comparison of Raman spectra of Carbolex arc-discharge carbon nanotubes excited with 1.96 eV (dotted lines) and 2.33 eV (full lines) laser excitation: a) whole spectra; b) the RBM-band.

As can be deduced from the G-band shape of figure 16, the CNTs' Raman spectra acquired with 1.96 eV excitation energy exhibit a broad Breit-Wigner-Fano peak shape which is indicative of metallic tubes. In contrast, using 2.33 eV photon excitation mostly semiconducting tubes are excited to be probed, which is evidenced by a much narrower G-band with Lorentzian peak shape. Additional confirmation is provided by the RBM-band. For both excitation energies the latter is located in the 150 – 210 cm^{-1} spectral window. A correlation with the respective transition energy on a Kataura Plot (figure 17) shows that for 1.96 eV metallic and for 2.33 eV semiconducting CNTs are in resonance.
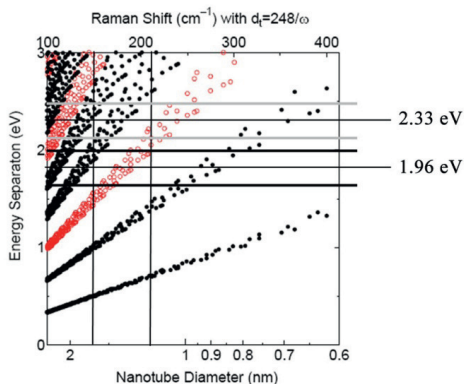

Figure 17. Theoretical Kataura plot. The two laser excitation energies (1.96 eV and 2.33 eV) and the CNTs diameter distribution of the Carbolex sample are indicated by horizontal and vertical lines respectively. Black dots stand for semiconducting, red dots for metallic SWCNTs.

4.1.2. CNT COMPOSITE

4.1.2.1. Comparison of different Raman spectra in the composite

Raman features of SWNTs are sensitive to chemical treatments and especially to covalent functionalization. It is well-known that the intensity of the D band due to the introduction of disorder in the SWNT sp^2 structure increases after functionalization. It has also been occasionally reported that a second disorder induced band can appear as an additional feature of the overall G band. For non functionalized SWNTs, the G band has two principal components, designated the G^- and G^+ bands (section 2.3.2.). The functionalization process may induce a high-frequency shoulder located at about 1600 - 1610 cm^{-1} and is referred to as the G^* band. A typical Raman spectrum of the as-produced arc discharge CNTs is shown in figure 18 in comparison to the other investigated systems, the functionalized CNTs and the CNT composite material. Additionally, a Raman spectrum of the pure PMMA is shown.

A typical spectrum of synthesized PMMA shows several bands attributed to vibrations of different groups. For the wavenumber range we are interested in, the C - O stretching band appears around 1710 cm^{-1} and the C - CH bending modes at 1500 and 1460 cm^{-1}. Asymmetric deformation of CH_2 is shown around 1334 cm^{-1}. For incomplete polymerization, there is an additional peak around 1640 cm^{-1} corresponding to C - C stretching in MMA. This bond is expected to be attacked through a radical polymerization mechanism, leading to the formation of PMMA during in situ polymerization. A very weak shoulder around 1640 cm^{-1} was only visible for the most concentrated samples, meaning that the polymerization is not affected by the presence of SWNTs.
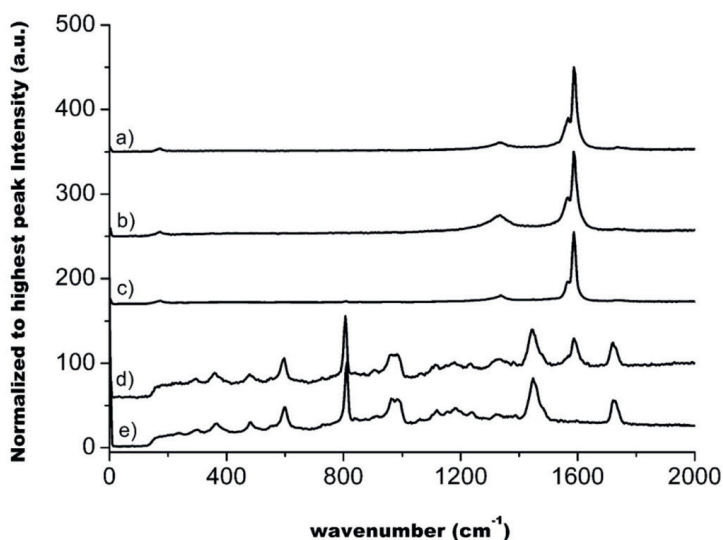

Figure 18. Typical Raman spectra obtained for the samples (excitation wavelength 532 nm): (a) as-produced SWNTs, (b) functionalized SWNTs, (c) aggregated SWNTs in composites, (d) dispersed SWNTs in composites, (e) pure PMMA.

It is important to note that PMMA itself manifests a Raman peak around 1334 cm^{-1}, in the D-band domain of the SWNTs. Raman spectroscopy probes here both the PMMA component of the composite and the SWNTs incorporated within it. If the combined contribution of PMMA and the CNTs D-band is considered this will be termed as D* (or D* peak/band) from now on. D-band term will only be used in case of pure SWCNT contribution. As mentioned, spectrum a in figure 18 is typical of as-produced SWNTs with a RBM band in the low frequency domain; the D band and the G band are around 1350 cm^{-1} and 1600 cm^{-1}, respectively. Spectrum b corresponds to the functionalized SWNTs used in the composites studied in this work. As expected in the case of chemically modified SWNTs, the D band intensity is increased compared to that of the pristine sample. In the composite there two types of Raman spectra have to be distinguished. Spectrum c is similar to that of as-produced SWCNTs. It shows only contribution from the SWCNTs but no signals attributed to PMMA are observed. Furthermore the absolute intensity of this kind of spectrum is much higher than for the second type, spectrum d. Besides a much lower absolute intensity this spectrum shows all signals from the PMMA (see spectrum e) and the G band of SWNTs which is visible around 1600 cm^{-1} in between two PMMA bands.

4.1.2.2. General distribution of CNTs - mapping of spectral features

Mapping of the SWNT distribution in the composite was done using the spectral imaging mode of the WiTEC CRM 200 confocal Raman microscope with an excitation wavelength of 532 nm and a spot size of approximately 10 μm. The laser scanned over a sample surface area of 186 × 186 μm2 and 24 × 24 Raman spectra were acquired with 10 s integration time each. Figure 19 shows the 2-D mapping of the Raman intensity of the G^+ component for typical surface areas of SWNT-PMMA composites. Assuming that there is no diameter-dependent CNT segregation in the composite, the intensity of this Raman mode is then proportional to the SWNT concentration at any given point (spot) in the samples, and therefore the G^+ intensity distribution represents that of the SWNTs in the composite.
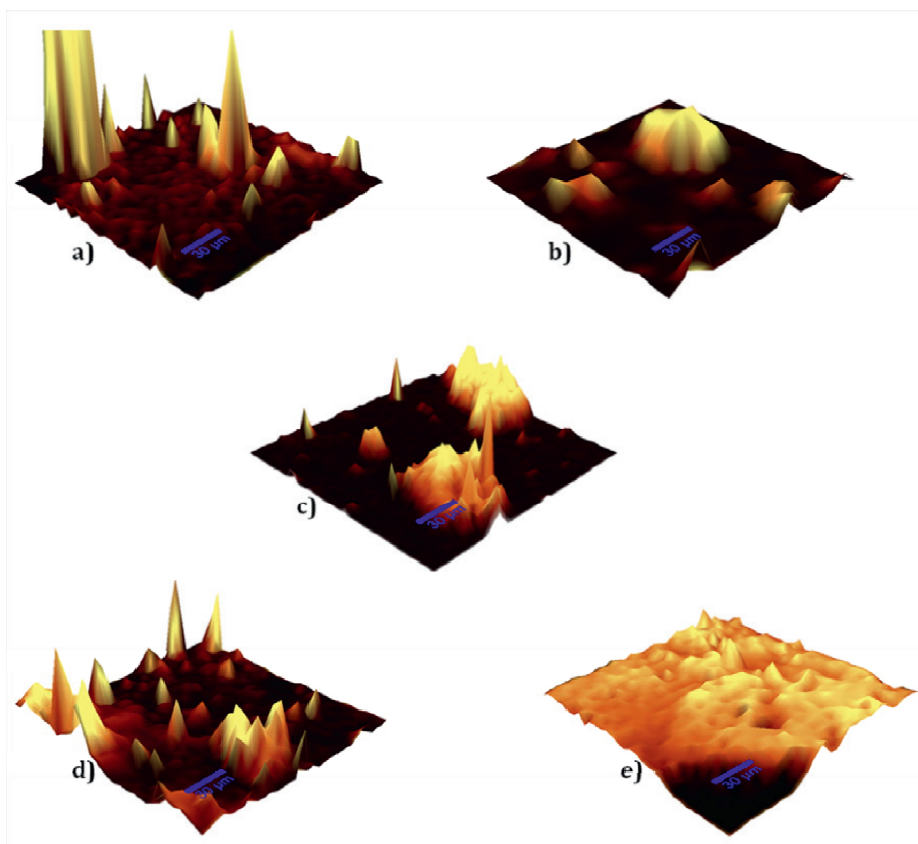

Figure 19. G^+ - intensity maps for a) 0.013 wt%, b) 0.023 wt%, c) 0.048 wt%, d) 0,097 wt% and e) 0,6 wt% CNT – PMMA composites, 2.33 eV laser excitation.

Spectral images were collected for composites with CNT concentrations of 0.013 wt%, 0.023 wt%, 0.048 wt%, 0.097 wt% and 0.6 wt%. Typical scans are shown in Figure 19. For low concentrations (below 0.6 wt%) multiple clusters (agglomerated CNTs) can be observed (yellow regions) showing much higher G^+- intensities than the surrounding (matrix) area were CNTs are dispersed in PMMA. Raman spectra taken in the clusters are typical of as-produced CNTs (figure 18) whereas spectra of the dispersed areas show both CNT and PMMA contribution. Aggregates of different shape and size, ranging from <10 μm diameter up to tens of microns are present in the samples with concentrations below 0.6 wt% which is also evidenced by optical images of the samples. Furthermore, some of the aggregates show gradually increasing G^+-intensities from the dispersed area to their center while others exhibit large abrupt intensity increases (ten or more times) in adjacent spots on Raman intensity maps (this might be an artifact caused by the spot size, i.e. for small agglomerates no gradual increases are observed).

Comparing the $I_{G+Aggregate}/I_{G+DispersedArea}$ ratio of the samples with low to those with high CNT loading we generally observed a decrease in $I_{G+Aggregate}/I_{G+DispersedArea}$ ratio (based on maximum intensities), see figure 20. For a loading of 0.6 wt% functionalized CNTs the ratio is 1 because no separation between aggregated and dispersed phase was observed.
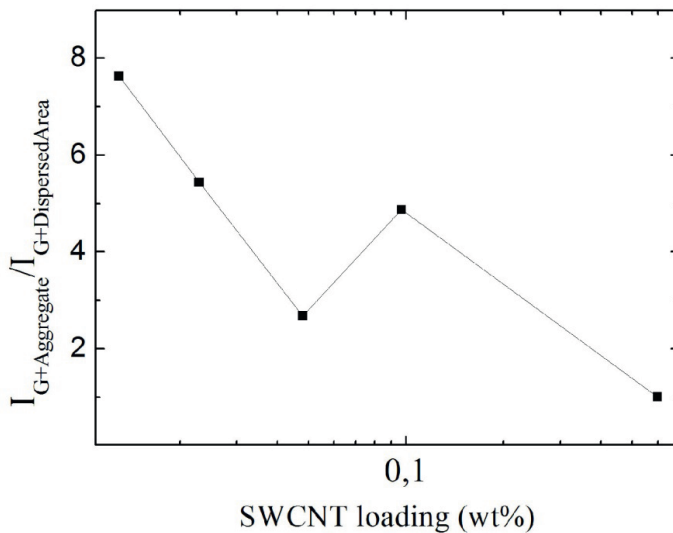
Figure 20. Dependence of intensity ratio G^+- intensity of a cluster/G^+ - intensity of matrix on CNT loading in the PMMA-CNT composites, for 2.33 eV laser excitation. The ratio for each sample is an average over more than 15 spectra taken for each (agglomerates and dispersed) area.

A rough estimate of the D/G^+-intensity ratio in both the dispersed area and the agglomerates for different CNT loadings was calculated from the maximum intensity values of the D^* (which includes the PMMA contribution) and G-band. This D^*_{max}/G_{max}-intensity ratio shows an overall trend from higher to lower D^*_{max}/G_{max} values when

going from low to high CNT concentrations (figure 21) as well as when going from dispersed area to agglomerate.
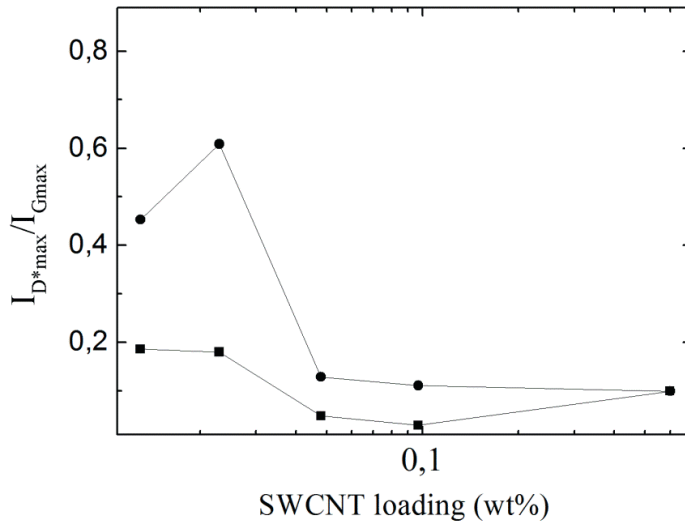

Figure 21. D^*_{max}/G_{max} intensity ratio dependence on CNT loading for aggregates (squares) and dispersed areas (circles) for 2.33 eV excitation. The ratio for each sample is the average resulting from more than 15 spectra taken for each (agglomerates and dispersed) area.

Notably, for 0.6 wt% CNT loading no aggregates and dispersed area could be distinguished. Accordingly the D^*_{max}/G_{max} -ratios for these concentrations coincide for dispersed area and agglomerates.

As one PMMA band is located within the D band zone, the analysis was first focused on the G band, the modifications of which can indeed help in the characterization of functionalization levels of the SWCNT surface. Figure 22 shows the G band of SWNTs belonging to the aggregates (figure 22a) and those dispersed within the matrix (figure 22b). According to the Kataura plot, only the semiconducting SWNTs are in resonance when using the green laser excitation (532 nm). The G band can then be fitted with two Lorentzian peaks as in the case of as-produced SWCNTs, one corresponding to the G- mode located at 1566 cm-1 and the other to the G+ mode at 1591 cm-1 (figure 22). For SWCNTs dispersed within the matrix, a shoulder (referred to as the G* band) at high wavenumber is added to the conventional G band. In this case, three Lorentzian peaks are required to fit the data. The additional peak is located around 1611 cm-1 in figure 22. A weak-intensity peak is observed around 1636 cm-1. It corresponds to the stretching of the C-C bonds of MMA monomers remaining in the composites as mentioned before. As a G* component is sometimes observed for defective SWCNTs after functionalization, modifications in the shape of the G band can be taken as manifestations of different states of

functionalization of the SWCNTs within the composites. Separation between non functionalized SWCNTs and functionalized SWCNTs has occurred during the polymerization process, the first type aggregating and the second type being dispersed within the PMMA.
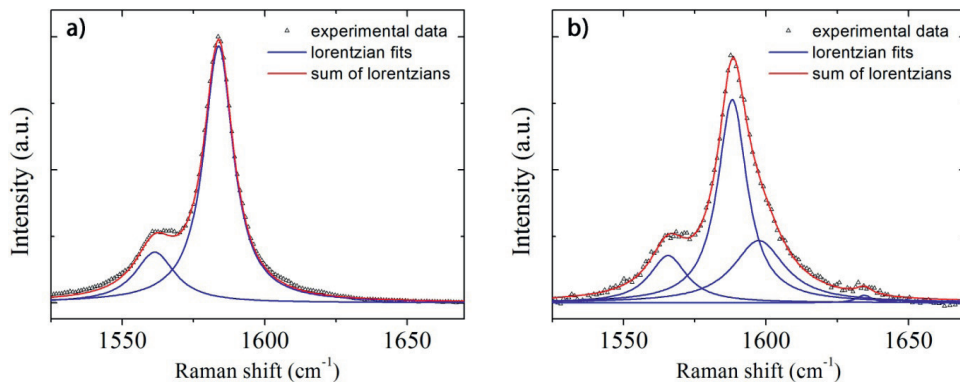
Figure 22. Peak fitting of the G-band in agglomerates (a) and dispersed area (b) of the SWCNT composites (2.33 eV excitation).

4.1.2.3. Boundary region cluster - matrix

The following section presents the investigation of the interface region between the SWCNT agglomerates and the areas with well dispersed nanotubes in CNT-PMMA composites by Raman imaging and spectral line scanning across these areas. As illustrated in figure 23, 2D spectral imaging allowed selecting large CNT agglomerates for further detailed examination. Raman line scans were performed starting within an agglomerate and ending in the dispersed area in order to study the boundary region. An example of such a scan - a resulting set of consecutive equally spatially separated Raman spectra - is presented in figure 23. A piezo scanner permitted 1 µm scan steps.


a)   b)
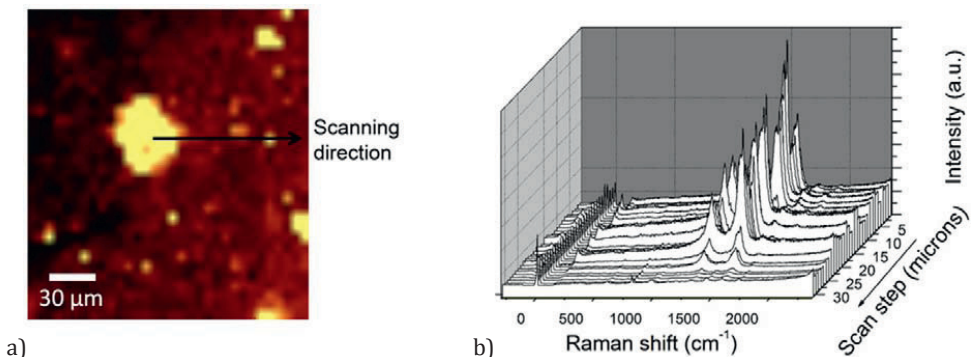
Figure 23. Raman spectral map of maximum G^+-intensity in CNT-PMMA composite (a) indicating CNT aggregates (bright spots). The blue arrow denotes direction of the spectral line scan (b) starting in the aggregate and ending in the dispersed area. Each spectrum in (b) corresponds to one step scan of one micron. Spectra collected at 1.96 eV photon excitation energy.

Raman spectra from different CNT aggregates in the composite were acquired. All line scans showed the general features illustrated in figure 23. Inside the agglomerated area no peaks related to the PMMA matrix are seen - only the CNTs contribute to the high intensity of the Raman spectrum. At some point a big drop in Raman intensity of the signal from CNTs occurs along with the appearance of peaks related to PMMA.

After acquisition, the Raman spectra were fitted by Lorentzian peak shapes. Typical peak fitting results of the Raman data from line scans in the aggregates of different sizes are presented in figure 24 for both the 1.96 eV and 2.33 eV excitation energies. It merits noting that the peak at 1330 cm^{-1} corresponds to a combination of the SWCNTs D-band and a small peak due to PMMA. From this point on, this combined peak will be denoted as D* to discern it from the pure D-band peak of CNTs. The G^+ peak intensity, the D^*/G^+-intensity ratio and the intensity ratio of the D* and the PMMA peak at 1450 cm^{-1} (D*/1450-intensity ratio) are plotted against the spatial position in figure 2. The D*/1450-intensity ratio was chosen because it reflects the contribution of the PMMA spectrum to the overall observed Raman spectrum of the composite. G^+ intensity and $D^*/1450$ ratio were normalized to their maximum values.

The Raman signal of CNTs (evidenced by the G^+-intensity in figure 24) is not only very inhomogeneous regarding different areas in the composite (agglomerated areas and dispersed areas) but also shows inhomogeneities in an agglomerated region itself in some cases (figure 24). However at some given step a large drop in G^+- intensity occurs accompanied by the appearance and decrease of the D*/1450-intensity ratio. At the same time the D*/G^+-intensity ratio increases. After a certain transition region all three ratios stabilize at new levels. This transition region is attributed (indicated by broken lines in figure 24) to the boundary interface area between the agglomerates and dispersed areas.
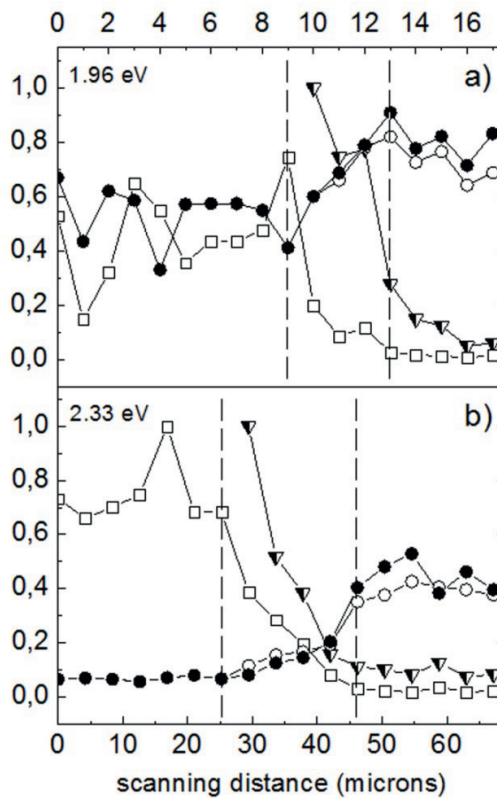
Figure 24. Raman data obtained from line scans through the aggregate/dispersed area boundary in different aggregates for a) 1.96 eV and b) 2.33 eV photon excitation energy. Symbols assignment: I_{G+} and $I_{D*}/I_{1450PMMA}$ (normalized to their maximum values) - empty squares and half filled triangles respectively; I_{D*}/I_{G+} - filled circles; I_D/I_{G+} (after subtraction of PMMA contribution) - empty circles. The interface regions between agglomerate (left side) and dispersed areas (right side) are indicated by vertical lines. Note different horizontal axis scale in a) and b).

The boundary interface area is found to be about 4 µm for an agglomerate of ~ 30 µm big while it is about 20 µm wide for an agglomerate of ~ 66 µm (figure 2a and 2b respectively) which is indicative of its dependence on the agglomerate size. With 1.96 eV photon energy we probe predominantly the metallic nanotubes in our sample while the se-

miconducting ones are in resonance with 2.33 eV photons. Analysis of the line scans across the boundary interface area does not reveal any significant difference in behavior of metallic vs semiconducting CNTs – both exhibit the same overall trends, i.e. drop of I_{G+} while increase of I_{D*}/I_{G+}. However, the metallic nanotubes show a higher level of I_{D*}/I_{G+} both inside the agglomerates and in the dispersed area. This could indicate a higher degree of functionalization with phenyl-ester groups of metallic compared to the semiconducting CNTs as was shown earlier [53, 54].
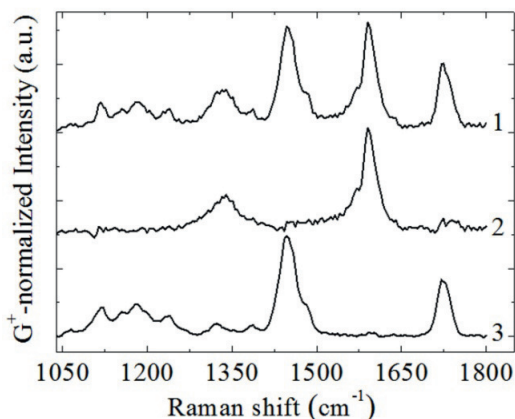
Figure 25. Raman spectra of composite dispersed area before (1) and after (2) subtraction of pure PMMA spectrum (3). Spectra collected with 2.33 eV photon excitation energy.

As mentioned above both SWCNTs and PMMA show a peak at around 1330 cm^{-1} (figure 25), complicating the interpretation of the D*/G$^+$-intensity ratio. Since no PMMA peaks are observable in agglomerates, it can be assumed that this peak is only due to the CNT – signal, thus reflecting the real D-band. However it is not trivial to separate the contribution of the CNT or PMMA signal to this peak in a boundary region or in the dispersed area of the composite as the PMMA contribution cannot be neglected in these cases. This raises the question if the observed increase of the D*/G$^+$-intensity ratio could simply be due to an increase of the PMMA contribution to the spectrum. To address this issue, the PMMA contribution was removed from the composite spectrum by subtraction of a reference PMMA spectrum (figure 25) followed by new peak fitting (This proceeding is based on the assumption that interaction between CNTs and PMMA molecules is negligible and the PMMA spectrum does not change significantly in the composite). The resulting corrected D/G$^+$-values are shown together with the uncorrected ones in figure 24 for both excitation energies. The corrected D/G$^+$-values are indeed lower than the uncorrected values which demonstrates that the PMMA contribution cannot be neglected for dispersed regions. However the corrected values are still significantly higher than those observed in agglomerated areas. It can thus be concluded that the observed increase of the D/G$^+$-intensity ratio going from agglomerated to dispersed regions is not due to only a higher PMMA contribution in the composite spectrum. With the corrected D/G$^+$-ratio

the line scans can now be fully interpreted. Firstly the drop of G$^+$-intensity indicates a decrease of CNT concentration from agglomerate to dispersed region. Furthermore the increase of the D/G$^+$-ratio indicates a higher defect level of the SWCNTs in the dispersed area. As functionalized CNTs are generally known to exhibit increased D-band intensities [53] this observation leads us to the conclusion that the fraction of functionalized CNTs is higher in the dispersed phase than in the agglomerates.
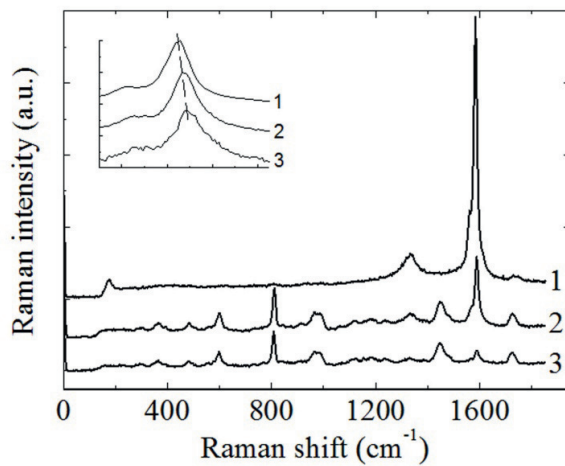
Figure 26. Raman spectra of CNT agglomerate (1) and two different spots (2, 3) in the dispersed area of composite collected at 15.6 kW/cm^2 with 2.33 eV photon excitation energy. Inset: G-band area of the spectra normalized to maximum G$^+$ intensity. The line drawn through G-band maxima is just guide to the eyes.

Further we observed inhomogeneities in the dispersed area itself as indicated by different G-band intensities relative to the PMMA peaks (figure 26).

Moreover these intensity variations are accompanied by a difference in the G$^+$-peak position – a more intense G-band exhibits a larger G$^+$-peak downshift from its position in the source CNT material. Actually this observation holds not only for the dispersed area but can be extended to the agglomerates exhibiting much larger G$^+$-downshifts.

These observations are investigated further in the sections 4.1.2.5. and 4.1.2.6.

4.1.2.4. D/G⁺-ratio: composite and source materials

In a further step the analysis of the D/G⁺ ratio was extended to include the CNT source material before and after functionalization.

Figure 27 shows Raman spectra of the raw SWCNT and the SWCNT-PhMeO samples for 1.96 and 2.33 eV excitation energies. Based on the peak-fitted Raman spectra at both energies, table 5 gives the ratio I_D/I_{G+}, of integrated D to G⁺ band intensity (the former sensitive to the number of defects induced by the chemical treatment, the latter being the tangential vibrational mode): As observed in the table, the first functionalization step increases the ratio by a factor of about three.
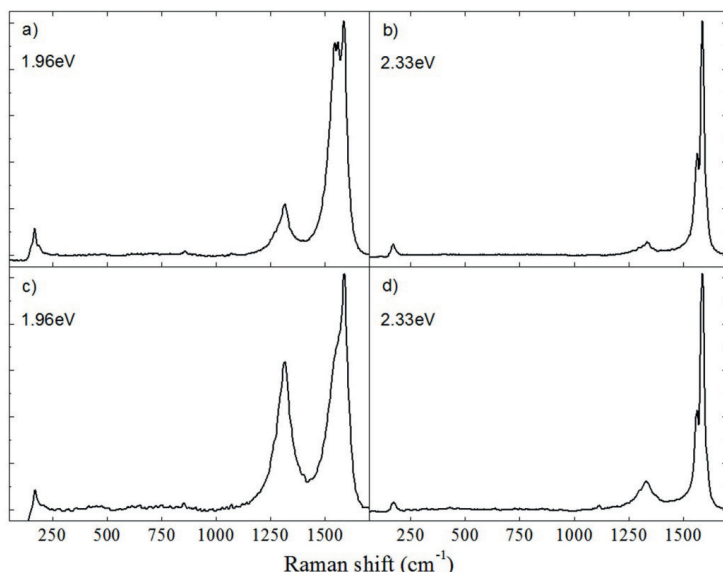
Figure 27. Raman spectra for raw SWCNT (upper panels) and SWCNT-PhMeO (lower panels) for the two used laser energies.

The functionalization procedure used allows obtaining SWCNTs that have indeed been chemically modified as expected. However, because of the high tendency of as-produced CNTs to agglomerate, it is very difficult to obtain uniformly-functionalized tubes in any given sample. Indeed, the high surface energy associated with the van der Waals forces tends to maintain the inter-tube binding and even functionalization can generally not fully separate the bundles. In this case, the outer walls of bundles´ outer tubes are strongly grafted, as volumetric adsorption experiments have shown [67]. A second point concerning the uniformity of functionalization is that earlier works carried out by our group[53] and elsewhere[34, 70, 71] have shown that metallic or small-diameter semiconducting tubes are preferentially functionalized. As a consequence of these two considerations, any functionalized SWCNT sample contains tubes bearing different functionalization levels according to the metallic or semiconducting nature of the individual tube as well as according to their position within a bundle.

It is well known that modifications of the SWCNT structure upon covalent functionalization can be evidenced by Raman spectroscopy. Several features are considered as signatures of this. If the degree of functionalization is high enough, the intensity of the D band with respect to that of the G^+ band is expected to increase due to the addition of sidewall defects created by the attachment of functional groups. In our case, the increase of I_D/I_{G+} being as high as a factor of 3 (table 5) allows asserting that we have efficiently grafted functions to the sidewalls of the raw samples. Such grafting may also affect the other spectral features through mass and charge transfer effects. Finally, the introduction of grafting-provoked defects may also induce a second disorder-induced band, designated G^*, appearing as a high-frequency shoulder of the G band, located at about 1605-1620 cm^{-1}. This disorder-derived band has occasionally been indicated for CNTs [72-74] but has been known for a considerably longer time in less organized carbonaceous materials [75, 76].

When the further-functionalized SWCNT-PhEster is integrated into the PMMA matrix, these CNTs will be dispersed according to the state of functionalization of the individual bundles or tubes. The more they are functionalized, the more their dispersion will be favored. As a result, the D/G^+-intensity ratio in the CNT-composite can provide information about the spatial distribution of the functionalized CNTs in the host.
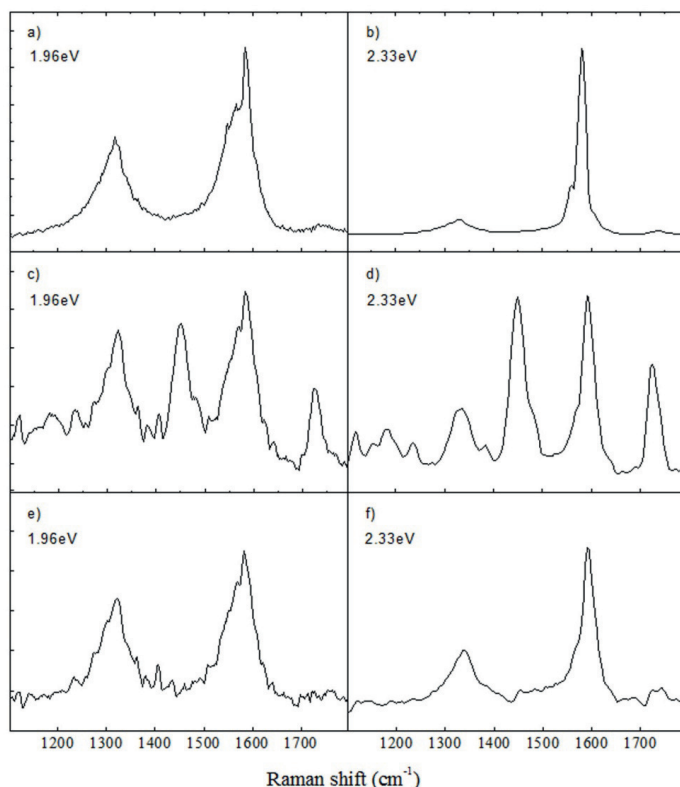
Figure 28. Raman spectra of composite agglomerated (a and b) and dispersed areas before (c and d) and after subtraction of the PMMA Raman contribution (e and f).

Figure 28 shows representative examples of the G-band region taken on the composite in CNT-agglomerated (top) and -dispersed (middle and bottom) regions. The middle panel of figure 28 clearly illustrates the preponderant contribution of the PMMA matrix in the Raman spectrum of the dispersed area. Table 5 shows average values of the integrated I_D/I_{G+} ratio determined for a typical agglomerated and dispersed composite area. It is interesting that analogous to raw and functionalized SWCNTs for which the latter manifest a higher D/G+-intensity ratio, the CNTs in the dispersed parts of the composite also manifest a I_D/I_{G+}, value greater than that of the agglomerated regions: Furthermore, for both laser energies, the highest values are observed for the composite dispersed areas, the highest value of all being for the 1.96 eV irradiation which probes the metallic tubes. For both energies, the ratio for the agglomerated areas is somewhat less than those of the functionalized CNTs before introduction into the polymer matrix.

Table 5. Average D/G+ integrated peak intensity ratios of investigated systems for 2.33 and 1.96 eV excitation energies.

| D/G+ intensity ratios for SWCNT systems	as-produced Carbolex	SWCNT-PhMeO	composite agglomerated area	composite dispersed area
2.33 eV	0.38	1.41	0.52	1.84
1.96 eV	1.23	3.68	2.02	3.90

It should be noted that those functionalized tubes integrated into the polymer matrix (SWCNT-PhEster) have undergone two additional steps with respect to the functionalized SWCNT-PhMeO. However, we have previously found[34] that the two additional steps affect only the end groups of the initially-grafted functions and do not have any further effect on the CNTs themselves. As indicated before, functionalization does not uniformly graft all the individual CNTs within a so-called "functionalized sample": there always remains a mix of functionalized and non-functionalized CNTs and CNT bundles. Thus the D*/G+ intensity ratio of this sample is actually an average over the different populations. D* is the disorder peak around 1350 cm^{-1} before subtraction of the PMMA "background". This distinction is relevant in the dispersed areas of the composite sample. The experimental I_D/I_{G+} results illustrated in Table 5 suggest that in the agglomerated regions of the composite, the fraction of non-functionalized CNTs is higher than in the functionalized CNT sample, i.e. I_D/I_{G+} is greater in the former than in the latter. The I_D/I_{G+} ratio of the dispersed composite region is higher than that of the functionalized sample since the fraction of functionalized tubes in the former is greater than in the latter. It is of interest to note that this behavior is true for both the metallic tubes probed by 1.96 eV excitation energy and for the semiconducting tubes probed by 2.33 eV irradiation.

This observation shows that functionalized SWCNTs are preferentially dispersed in the PMMA matrix as intended while preferentially the non- or lesser-functionalized fraction forms the aggregates.

4.1.2.5. G+ - peak shift in the composites

As discussed earlier in the text (section 2.3.2.) the G+-peak shift from its original position in the spectrum of functionalized nanotubes before their incorporation into a polymer matrix may provide information about interaction/coupling between the CNTs and the polymer molecules. The G-band in the Raman spectra which were acquired during spectral imaging of the composites was subsequently fitted by Lorentzian peak shape and the G+ component was plotted in a 2D map (the whole procedure was conducted by the WiTec software package).

When comparing the Raman maps plotting G+-intensity and G+-peak position, it was found that the G+ peak position is shifted to lower wavenumbers especially in agglomerates whereas this is not the case for the dispersed area. This downshift in agglomerates could be as big as 20 cm^{-1}. Figure 29 demonstrates an example of two Raman spectral maps - the G+-intensity distribution (manifesting the CNT concentration) and the G+-peak position. Areas of high CNT concentration are very closely correlated with those having a large downshift of the G-band. It should be noted that the G+-peak position in the Raman spectra taken from the dispersed area lies in the region where it is expected for pristine CNTs, i.e. around 1588-1590 cm^{-1}.
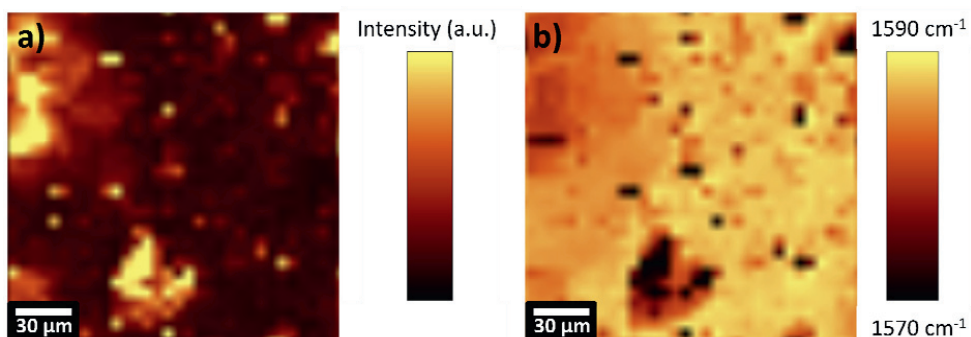
Figure 29. Raman maps of 0,097 wt% composite: a) plot of G+-intensities illustrating spatial distribution of CNTs. b) plot of G+-peak position illustrating spatial distribution of peak shift.

It is known that the G+-peak position is sensitive to pressure [33], temperature [32, 37, 38, 41], strain [61] or charge transfer [34] and possibly provides information about interactions between CNTs and the polymer host within a composite. However, it was unexpected that a G+-band downshift was always observed in areas showing a high CNT concentration (figure 29), i.e. areas with a lower fraction of functionalized CNTs. Logically such areas should show a lower interaction between the CNTs and the polymer matrix. Charge transfer is excluded as a possible reason for the observed downshift; pressure was also unlikely to be the reason as a downshift of the G-band would imply a pressure lower than atmospheric. There is no reason here why areas of highly agglomerated CNTs should show pressures lower than those of well dispersed CNT areas. Tensile strain

would also lead to a downshift of the CNT G-band but, again, it is unlikely that areas of agglomerated CNTs should experience more tensile strain than well dispersed areas.

4.1.2.6. Laser heating experiments

As mentioned, it was found some time ago that the G-band position of CNTs is influenced by temperature: higher temperature leads to a G-band downshift [31, 37, 38, 41, 43]. Therefore laser heating experiments were performed for the four previously-mentioned systems: raw CNTs, functionalized CNTs, agglomerated and dispersed composite areas using both a green laser (2.33 eV) and a red laser (1.96 eV) excitation source. Raman spectra were acquired at the same spot on the sample for different laser power densities starting from low to high energies. After peak fitting, the G$^+$-peak position values were plotted against laser power density and subsequently fitted by simple linear fits for laser power densities up to 20 kW/cm^2 (at higher power densities deviation from linear behavior was observed) to obtain peak shift rates. For every sample and both laser excitation at least two experiments at two different spots were performed.
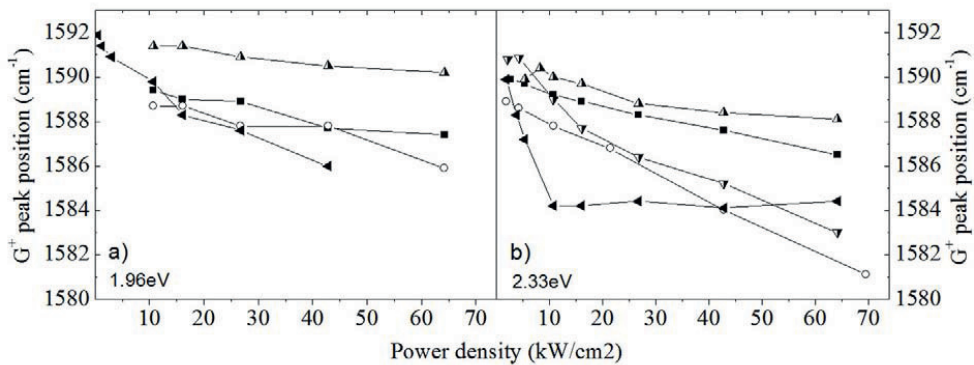
Figure 30. Results of representative laser heating experiments. Symbol assignment: as-produced CNTs – full squares, functionalized CNTs – open circles, composite aggregates – full left pointing triangles, composite dispersed area 1 – up-pointing half filled triangles, composite dispersed area 2 – down-pointing half filled triangles.

Figure 30 and table 6 show the results obtained. Let us first examine Figure 30. The only immediately obvious result illustrated here is that in all cases an increasing power density causes a G$^+$ downshift. At both laser energies, the smallest variation is noted for one of the dispersed areas within the composite and the greatest temperature sensitivity is noted for the agglomerated areas within the composite. Many more results have been utilized in establishing the average values given in table 6. These data represent the overall behavior in spite of significant sample-to-sample variations for a given type of the four "systems" studied. The heating rates are calculated from peak shifts based on the equation [37]:

$$\Delta T = \Delta\omega(G^+)/-0{,}0258 \qquad (1)$$

Within a given type of sample, the spot-to-spot variations differ by less than a factor of about three except for the spots examined in the agglomerated region of the composite

at the higher photon energy; raw and functionalized CNTs show nearly the same values (1.96 eV) or slightly higher values for functionalized tubes in the case of 2.33 eV excitation energy.

Table 6. Laser heating effect observed in different investigated systems for 1.96 and 2.33 eV excitation energies.

SWCNT systems	2.33 eV		1.96 eV	
	G$^+$-shift rate [cm^{-1}/ (kW/cm^2)]	heating rate [K/ (kW/cm^2)]	G$^+$-shift rate [cm^{-1}/ (kW/cm^2)]	heating rate [K/ (kW/cm^2)]
as-produced Carbo-lex	-0.077	2.98	-0.055	2.13
SWCNT-PhMeO	-0.127	4.92	-0.06	2.33
composite agglomerated area	-0.578	22.40	-0.089	3.45
composite dispersed area	-0.125	4.84	-0.031	1.20

For both excitations, the G$^+$-peak position shift of agglomerated regions is about 5-6 times stronger than in dispersed regions. Furthermore, as illustrated for the agglomerated area of figure 30, this strong shift observed for agglomerated regions can already start at a very low power density, e.g., less than 0.54 kW/cm^2 which was a lower limit to acquire a decent CNT Raman signal in the composite. In fact, we could not find a power-density sufficiently low in which for this part of the composite, the G$^+$-peak position was fully stabilized independent of the incident laser power density. It was found that shift rates of the dispersed regions are about the same as for raw and functionalized CNTs (2.33 eV) or smaller (1.96 eV). Table 6 and Figure 30 clearly illustrate that the shift rates are always higher for the higher photon laser light. Finally, we observed in all experiments using this excitation energy that the G$^+$-peak position against laser PD for agglomerates showed leveling starting at a PD > 10 kW/cm2.
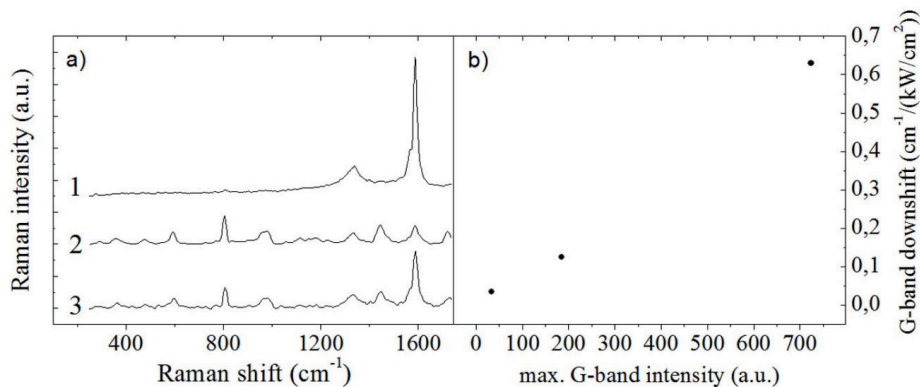
Figure 31. a)Raman spectra (2.33 eV) for agglomerate (1) and two different spots in dispersed area (2, 3). (b) Illustration of the correlation between the absolute Raman intensity and downshift of the G-band .

It seems that the shift rate increases with increasing G^+-intensity, i.e. local CNT concentration. This is illustrated in figure 31 where we have plotted the observed G-band shift rates in three points of the composite (see figure 31 for their Raman spectra), one in an agglomerate and two in two different positions in the dispersed phase, against their maximum G-band intensity.

We return to the plateau observed on figure 30 for the composite cluster region using green laser excitation. This was not observed in any other laser heating experiment done in this work. In an additional experiment, images of the probed spot on the composite surface were taken in between every power increase. It was observed (figure 32) that an ablation mark appeared at the same power density as the leveling of the G-band shift. Furthermore, Raman spectra (figure 32, left panel) show that at a certain laser power the absolute intensity of the signal goes down. This can only be caused either because a) the probed surface came out of focus due to ablation of material or b) the number of scatterers, i.e. nanotubes, decreased possibly through heat-induced damage on tubes or c) a mix of the two. The temperature of the nanotubes when the plateau started to appear was between 325 and 425 °C (estimated from G-band shift), well above the melting and boiling points of neat PMMA which are about 160 and 200 °C.
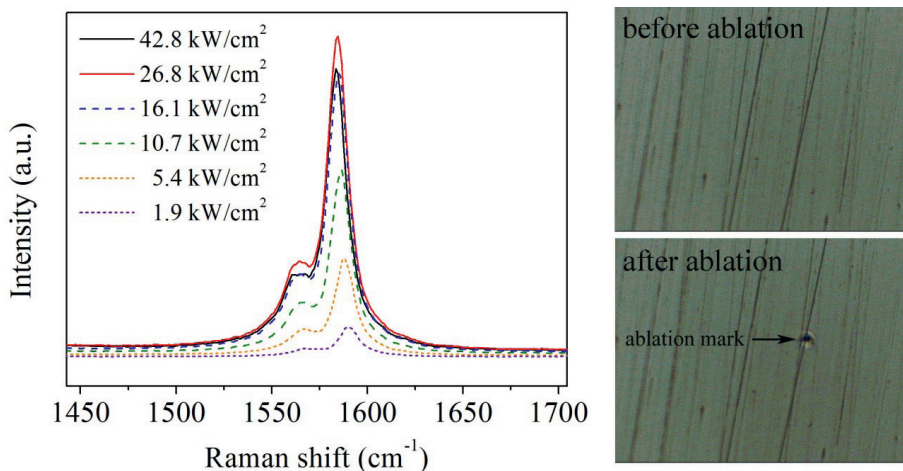
Figure 32. Raman spectra collected from a probed spot for increasing laser power densities (left panel); area of probed spot before and after the experiment (images on the right).

Concerning the G^+-shift there may be one small effect related to the stress imposed by the embedding the CNTs in the polymer host. Indeed, the G^+-peak positions of both agglomerated and dispersed areas at the lowest used laser PD are all located between 1589 and 1592,5 cm^{-1} whereas for raw and functionalized tubes the G^+-peak position is located around 1588-1590 cm^{-1}. This small upshift in the composite relative to pure CNT systems could, in agreement with Hadjiev et al. be explained by a small pressure applied to the tubes during the curing of the composite [56].

Taking into account all the considerations from section 4.1.2.5., we conclude that the greater downshift of agglomerated areas of the composite relative to dispersed areas can be attributed to laser induced heating effects.

While equation (1) holds only for pure SWCNT systems, it most probably also provides a rough first estimation in the composites. Examining figure 30 in the light of this equation, we observe that for the given representative samples shown, beyond a power density of 10 or 20 kW/cm^2, the temperature has risen by 200°C or more and continues to do so as the PD increases further. This is true in all cases except at 2.33 eV for the agglomerated region within the composite. Here, the decrease in G$^+$-band frequency is extremely rapid, i.e., the temperature has risen very quickly, well above the melting temperate of PMMA, which is between about 130° and 200° according to the reference cited and the exact state of the polymer. In all experiments using this excitation energy, the G$^+$-peak position against laser PD for agglomerates showed leveling (figure 30) starting at a PD > 10 kW/cm^2. We explain this by the fact that at the same time ablation of the probed surface was observed which inhibited any further temperature increase and thus any further downshift of the G-band. At the same time, the absolute intensity of the CNT Raman signal went down. A reason could be defocusing resulting from the ablation of material on the surface.

One might question whether functionalization plays a role in CNT heating. From our experimental data it becomes clear that this much higher heating rate in agglomerated regions cannot be due to the functionalization of the CNTs before incorporation in the composite since as-produced and functionalized CNTs show comparable peak shift values (table 6). Further, if one takes into account that the fraction of functionalized tubes is presumably higher in the dispersed composite area than in the agglomerated area, G$^+$-peak shift rates should also be higher in the dispersed area if it was due to functionalization. But this is not observed.

Laser-induced heating effects in carbon nanotubes have been noted in several previous works [37, 42, 66] but much less is known on thermal effects in CNT composite material. Interestingly Kao and Young [65] examined a composite material with an almost equal loading to ours (0.1%) and they employed a He-Ne laser of 633 nm wavelength. They found a lower shift rate for the composite than for the pure CNTs and their CNT heating rates are compatible with those of the dispersed composite area in our work.

To the best of our knowledge, such a huge spatial difference in the heating behavior in a composite has never been observed elsewhere. An interesting question is the physical origin of these different heating rates. The following factors are proposed. As CNTs are very good light absorbers, one explanation could be the better dispersion and lower concentration of CNTs in the dispersed area which means less absorbers per unit volume resulting in less heating. If, on the other hand, we take into account that CNTs in the dispersed area exhibit a higher fraction of functionalized tubes then they might be expected to be better coupled to the matrix and thus more efficiently dissipate their heat. Thirdly the physical state of the CNTs could also have some effect. It is known that individual CNTs show much better heat dissipation than bundled CNTs. In the composite material, the smaller bundle size or perhaps even the individualized state of some CNTs in the dispersed areas would result in a lower laser heating effect as well. However for

the moment we have no quantitative information on the bundle size in the dispersed area. It may well be that all these factors contribute simultaneously to some extent.
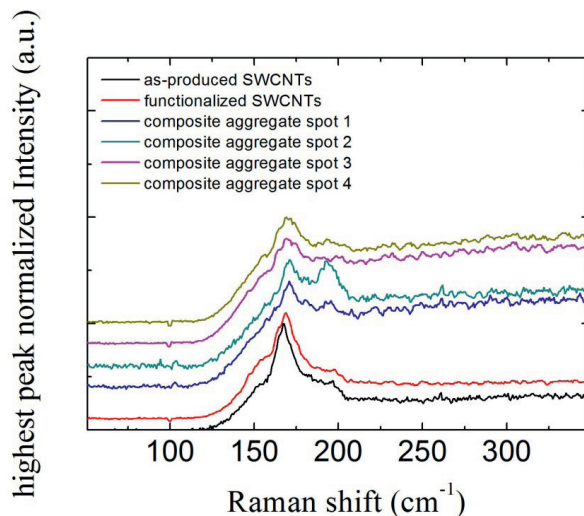
4.1.2.7. Comparison of RBM spectra

As pointed out earlier, functionalization leads to modifications of the tubes' surface. Differences in the degree of functionalization between different types of SWCNT might thus be observed via RBM-band. Furthermore, the RBM-band might indicate inhomogeneities with respect to the distribution of certain specific nanotube chiralities in the composite material. Therefore the RBM-bands of all four systems were recorded for both 1.96 and 2.33 eV excitation energies and the resulting spectra compared. Unfortunately, due to low CNT concentration in the dispersed area of the composite no RBM signal could be acquired thus this part of the composite characterization is limited to the agglomerated regions only.

For both laser excitation energies there is a slight difference in the shape of the RBM band between as-produced and functionalized tubes was observed (figures 33 and 34). Namely, the spectra from functionalized tubes exhibit an "upshift" of the RBM band compared to the as-produced tubes for both excitations and there is a slightly higher intensity around 160 cm^{-1} for 2.33 eV excitation which is an indication of change in resonance conditions for certain CNT species as a result of functionalization. Similarly, the RBM spectra of aggregates in the composite acquired with 2.33 eV excitation energy showed a slight difference to RBM spectra of as-produced material and the functionalized CNTs - a small "shoulder" appearing around 180 cm^{-1} indicating a better resonance conditions for the smaller diameter CNTs corresponding to this frequency range (figure 33). Using 1.96 eV excitation energy, very different RBM spectra were acquired from different spots/different agglomerates of the composite (figure 34). For example spot 2 shows a second peak at the place where in the as-produced material a big shoulder appears.
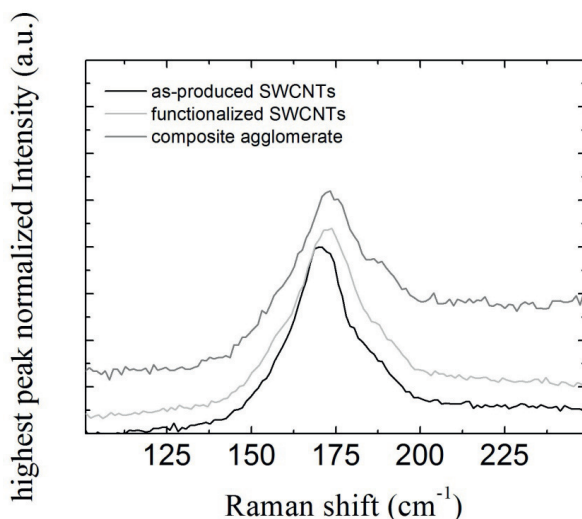
Figure 33. Comparison of RBM-spectra of the different systems taken with 2.33 eV excitation energy.

Figure 34. Comparison of RBM-spectra of the different systems taken with 1.96eV excitation energy.
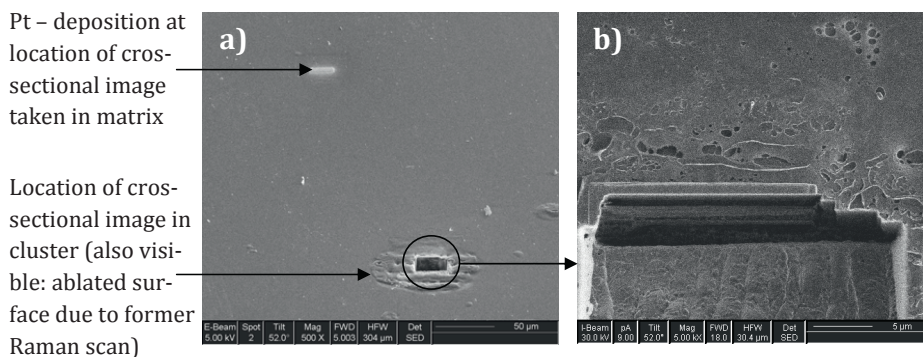
The observed differences in the shape of RBM spectra of different spots indicate that the composite is not only inhomogeneous regarding the CNT concentration but also regarding the distribution of the nanotube types. Further experiments would be necessary to ascertain this additional inhomogeneity in distribution of different CNTs species in the composite.

4.2. *FIB/SEM dual beam experiments*

4.2.1. CROSSECTIONAL IMAGING

Aim of this experiment was the acquisition of high resolution SEM images in different areas of the composite material, i.e. dispersed and agglomerated areas. Using a FIB it is possible to take crossectional images at different positions on the sample with submicron precision. Since the imaging plane in that case is perpendicular to the sample surface the inside of the material can be studied. Crossectional images were taken from the sample with 0.6 wt% CNT loading and from the sample with 0.097 wt% CNT loading in both the dispersed area and in an agglomerate.

For these experiments the composite samples were mounted on metal sample holders with copper double tape. Graphite paste was used to assure electrical connection between sample and metallic holder. After mounting, the sample was coated with a thin layer of graphite to minimize charge accumulation effects which would disturb both manipulations with the FIB and as well imaging via SEM. To be sure to take images from an aggregate the fact that the composite reacts strongly to light irradiation as well as electron irradiation showing heavy ablation was exploited. In a Raman experiment a square area on the sample surface was scanned causing ablation of the sample's surface toplayer (figure 35). Subsequently, this spot could be detected in the SEM. A platinum layer (1-2 µm thick) was deposited for protection of the underlying material against structural defects and curtaining effect. Then a rectangular hole was sputtered out of the surface to provide access for imaging. The surface of interest for imaging was subsequently polished (going from higher to lower ion currents, thus having a smaller beam diameter) to obtain a smooth, flat surface.

Pt – deposition at location of crossectional image taken in matrix

Location of crossectional image in cluster (also visible: ablated surface due to former Raman scan)

Figure 35. a)SEM image of CNT-composite surface after Pt-deposition in the dispersed area (upper left) and imaging of the agglomerated area (lower right); b) zoom to agglomerated area, spot after acquisition of crossectional image.

0.6 wt% composite sample

In a surface crack (which appeared due to electron beam irradiation) single-wall nanotube bundles with diameters between 20 and 40 nm could clearly be observed (figure 36).The crossectional image (figure 37) showed many small white dots distributed over the whole crossection. Those dots have diameters between 11 and 39 nm, the same as the nanotube bundles observed in the crack. In combination with the Raman data which shows uniform nanotube signal distributed over the composite area and thus uniform CNT concentration, those white dots are attributed to crossections of nanotubes cut by the FIB. Even if overall the nanotubes seem to be distributed evenly over the imaged area there are small agglomerated spots (red circle in figure 37).
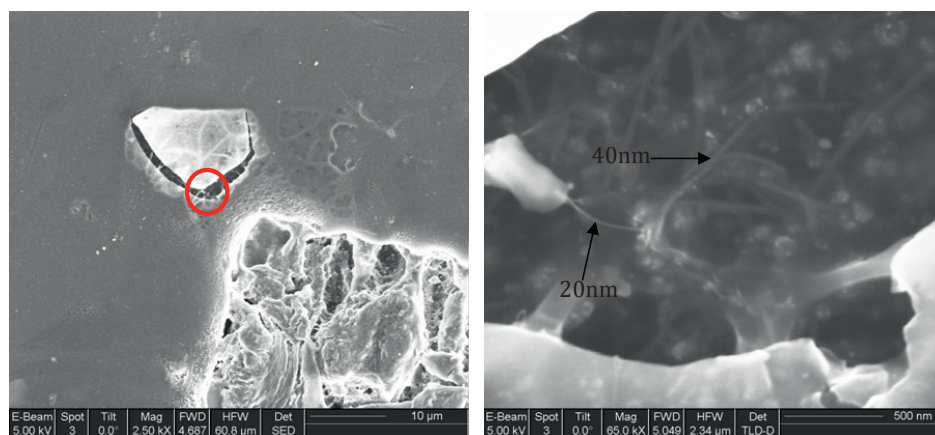
Figure 36. Left side **-** SEM image of surface crack which appeared during observation. Right side - CNT bundles of various diameters in the crack (marked by red circle on the left side).
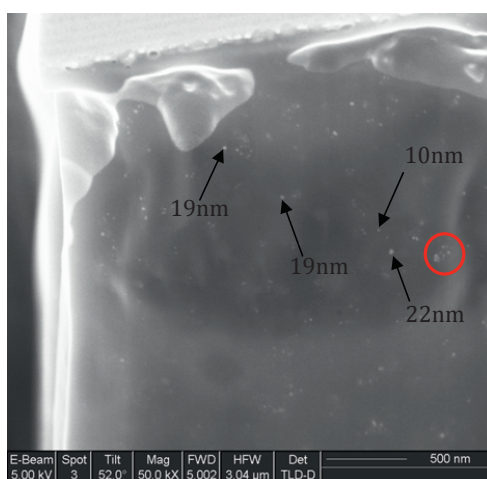
Figure 37. SEM image of crossection taken in the 0.6 wt% composite. CNTs are visible as white dots and the diameters of some bundles are indicated.

0.097 wt% composite sample – aggregate

The crossection image of an aggregate taken in the 0.097 wt% composite sample (figure 38) exhibits the small white dots which are attributed to cut nanotubes. Diameters are between 5 and 70 nm. The concentration of those spots is less than for the 0.6 wt% sample.
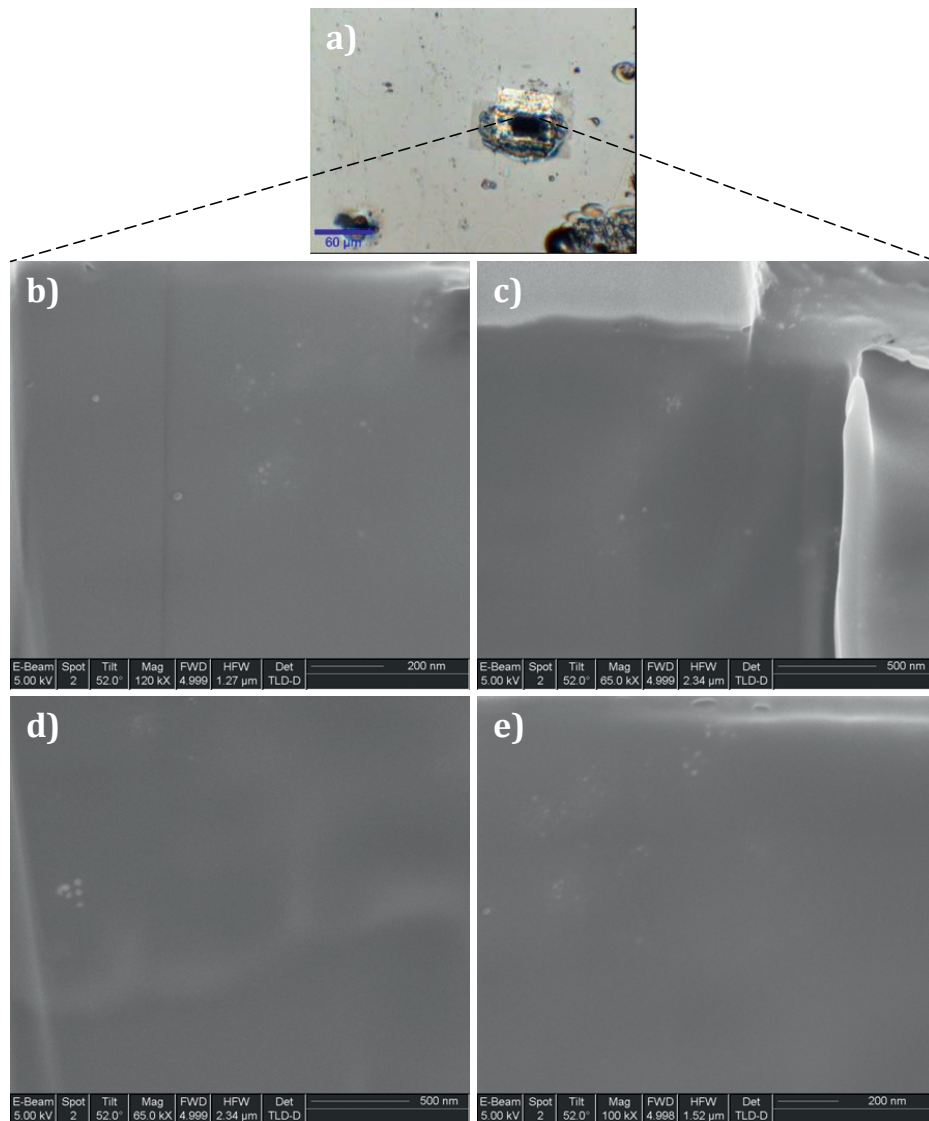
Figure 38. Images of crossections in an agglomerate taken in the 0.097 wt% CNT-composite: a) optical microscope image showing the location from which the crossectional images were taken. b-e) SEM images of crossection, CNTs appear as white dots.

0.097 wt% composite sample – dispersed area:

The crossectional images taken in the dispersed area in the 0.097 wt% composite sample showed surprisingly no sign of nanotubes (no white dots) (figure 39). One might assume that there were no CNTs in that area. However Raman mapping showed a signal of CNTs everywhere on the investigated area. Furthermore, Raman measurements taken after the FIB experiment at the same spot showed a CNT-signal as well.
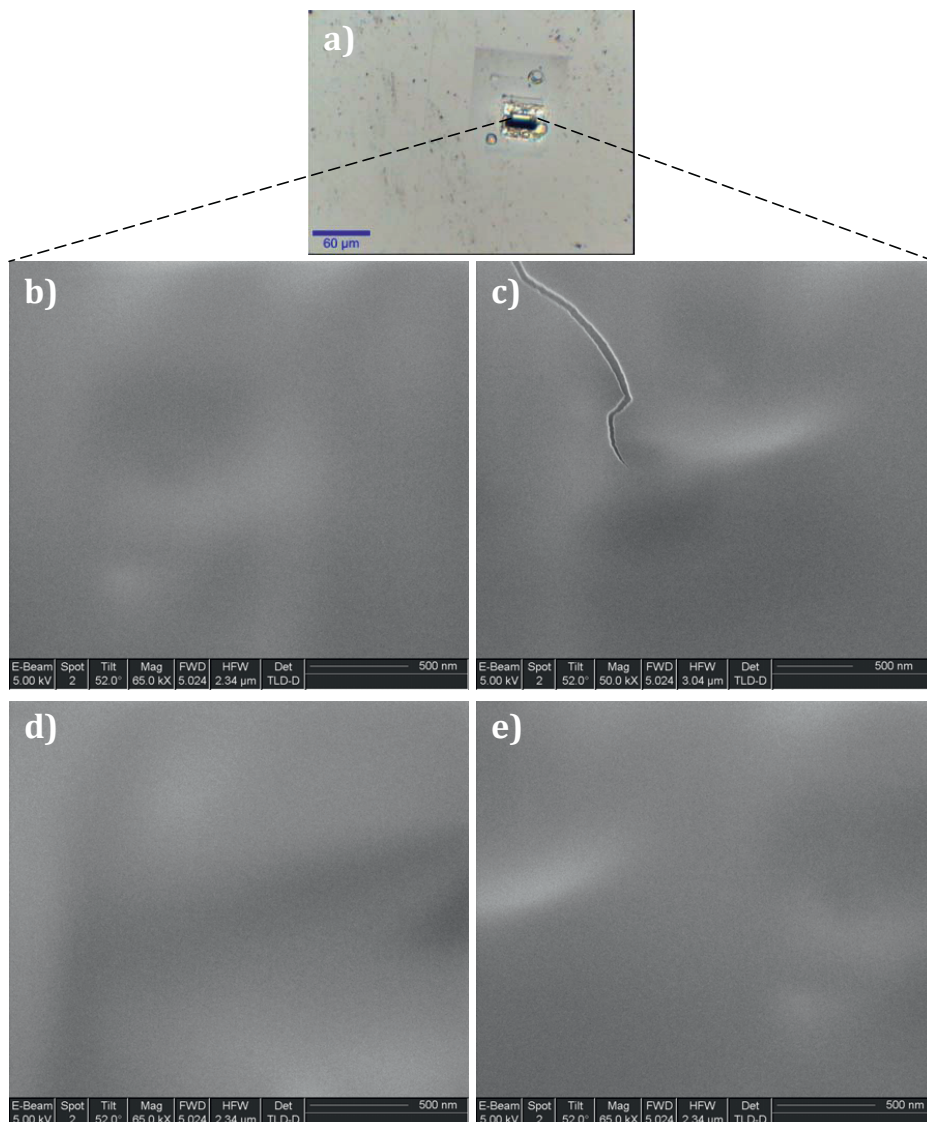

Figure 39. Images of crossections in the dispersed area taken in the 0.097 wt% CNT-composite: a) optical microscope image showing the location from which the crossectional images were taken. b-e) SEM images of crossection.

Possible explanations of the absence of CNTs on the SEM images of the dispersed area might be the following:

- SWNT are in very small bundles < 3 nm or even individual. Thus, the resolution of the SEM would not be good enough to visualize them

- As the CNT concentration in this area is supposed to be very low (indicated by Raman data) the second explanation could be that CNTs are oriented parallel to the crossectional surface and therefore not cut. However this seems to be very unlikely as no signs for orientation could be seen in the crack on the 0.6 wt% sample. Furthermore an area of approximately 7 x 18 μm was observed in the dispersed area.

4.2.2. COMBINATION OF RAMAN AND FIB DATA

To verify that the crossectional images were really taken in an agglomerate and in the dispersed area, Raman spectra were taken afterwards in closest possible proximity. The Pt - layer made it impossible to take spectra exactly from the imaged areas. Due to the FIB cutting marks these areas could be relocated without any doubt under the optical microscope of the Raman setup.

Figure 40 shows resulting spectra confirming a high CNT concentration in the agglomerate (strong Raman signal) and a low CNT concentration in the dispersed area (much weaker Raman signal). It should further be mentioned that a buckle around 1200 – 1700 cm^{-1} is observed. This is attributed to the carbon layer which was deposited on the sample during FIB preparation.
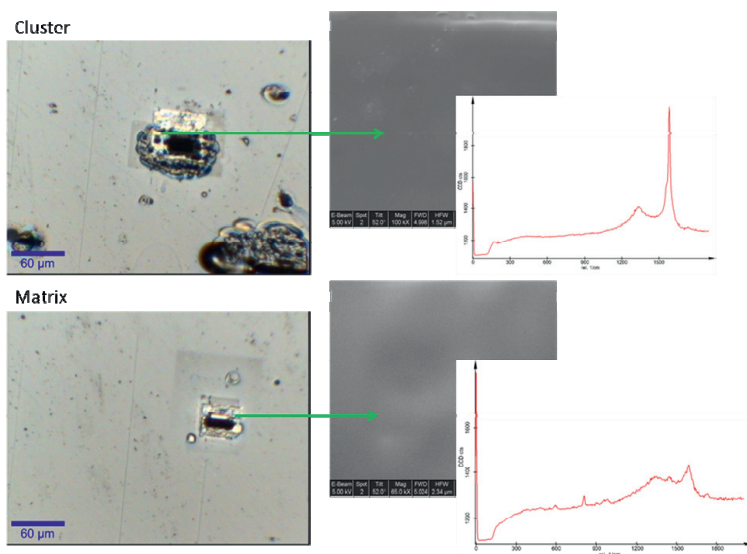
Figure 40. Optical images (left) of the surface of the composite with 0.097 w% CNT loading, SEM crossectional images (middle) and corresponding Raman spectra taken after FIB application of aggregate (upper right) and dispersed area (lower right).

4.2.3. IMAGE ANALYSIS

From the acquired images of the sample with 0.6 wt% CNT loading and the images of the agglomerate of the sample with 0.097 wt% CNT loading the number per area, diameter and area fraction of CNT bundles/white dots were determined (tables 7-9).

Table 7. Diameter values from image analysis of crossectional SEM images.

Fraction of CNT [wt%]	$D_{CNTBundle}$ [nm]			
	average	standard deviation	min	max
0,6	20,67	5,28	11,35	38,74
0,097	18,55	9,63	5,06	69,51

Table 8. Area fraction values from image analysis of crossectional SEM images.

Fraction of CNT [wt%]	A_{aCNT} [%] average
0,6	0,631
0,097	0,170

Table 9. Number of CNTs per area values from image analysis of crossectional SEM images.

Fraction of CNT [wt%]	N_{aCNT} [1/μm^2] average
0,6	21,4
0,097	6,3

An average diameter of the CNT bundles of 20.5 nm and a little bit lower, 18.5 nm, was found for the sample with 0.6 wt% and 0.097 wt% CNT loading, respectively. For the 0.097 wt% sample a much higher standard deviation was found and maximum diameters of 69.51 nm whereas minimum diameters of 5.06 nm. The area percentage of CNTs for the 0.097 wt% cluster showed with 0.17 % a much higher value than the CNT loading of the sample. This supports the conclusions from Raman spectroscopy experiments that the CNT concentration is increased in the agglomerates. For the 0.6 wt% sample an area fraction of 0.63 % was found which is close to the loading of CNTs for that sample. Again this is in agreement with previous Raman data indicating a much more homogenous distribution of the tubes with just smaller deviations. Since CNTs are molecules with a very high aspect ratio which can be more than 1000, they can be bent and differently oriented with respect to a crossectional image. Therefore interpretation of such 2D-

images of a CNT – composite system is not straight forward and has to be considered with caution.

5. SUMMARY OF PAPERS

Paper 1

This paper reports on an original experimental approach to the characterization of SWNT/polymer composites. This work deals with the multi scale characterization of nanocomposites. Covalently functionalized SWNTs were incorporated in a PMMA matrix using an in situ polymerization procedure. It is shown that their presence does not affect the radical polymerization process. Combining Brillouin and Raman spectroscopy, it was possible to associate the obtained mechanical properties of the material at the macroscopic scale to the state of functionalization of the SWNTs within the polymer matrix.

Paper 2

This work is aimed at characterization of the carbon nanotubes (CNT) distribution in polymethylmethacrylate (PMMA)–CNT composites by high-resolution Raman spectroscopy. In particular, it focuses on study of the boundary regions between the CNT aggregates and the surrounding areas where the CNTs are well dispersed in the PMMA matrix. Different laser excitation energies (1.96 and 2.33 eV) were used to preferentially probe metallic and semiconducting SWCNTs, respectively. At both photon energies, spectral line scans across the boundary regions were performed revealing a substantial drop in intensity of G^+CNT Raman mode and an increase of the D/G^+-intensity ratio. The latter testifies to a preferential dispersion of functionalized CNTs in the PMMA matrix. Certain inhomogeneities were observed by Raman spectral imaging even in the areas with well-dispersed CNTs.

Paper 3

This paper continues the previous work including analysis of the source SWCNT material before and after functionalization. Examination of the D/G^+-intensity ratio of the SWCNT material before incorporation into the composite showed a higher value for functionalized than for the raw SWCNTs. Furthermore, the metallic nanotubes exhibited a higher degree of functionalization. Raman spectral imaging revealed some inhomogeneities of the CNT distribution in the composite material: the spectra of the areas with good CNT dispersion in the composite exhibit a higher D/G^+-intensity ratio than in areas with CNT agglomerates indicating that functionalized CNTs are preferentially dispersed in the polymer matrix while non functionalized ones tend to group together in agglomerates. Furthermore significant laser heating of the SWCNTs in composites is reported resulting in a downshift of the G^+-peak position which was much more pronounced in agglomerates than in the areas with dispersed CNTs and detected at the very lowest laser irradiances.

6. SUMMARY AND CONCLUSIONS

In this work, we have carried out a resonant Raman spectroscopy study of a composite material made of a PMMA polymer host and functionalized SWCNTs and of the SWCNT material before and after functionalization. To probe semi-conducting and metallic nanotubes populations independently two different excitation energies were employed, namely 1.96 eV (probing metallic SWCNTs) and 2.33 eV (probing semi-conducting SWCNTs). As a complementary analysis method SEM/FIB was used.

Although using functionalized SWCNTs for the composite synthesis, agglomerates of SWCNTs surrounded by a more dispersed phase are observed by mapping of their Raman G-band intensity. This observation was confirmed by SEM crossectional images from the composites interior.

By performing Raman line scans starting in agglomerates and ending in the dispersed phase, information about the boundary region between the two phases can be obtained. The width of this boundary area varies with the agglomerate size and analysis of the G^+ intensity as well as of the I_D/I_{G^+} ratio indicates that the dispersed phase has a lower CNT concentration and at the same time contains preferentially functionalized SWCNTs. An examination of the D/G^+-intensity ratio of the SWCNT material before incorporation into the composite shows a higher value for functionalized than for the raw SWCNTs. CNT Raman spectra of dispersed areas in the composite manifest a higher D/G^+ intensity ratio than in agglomerated areas and even than in the SWCNT-PhMeO sample. This again indicates that functionalized SWCNTs are preferentially situated in the dispersed composite area. All these results underline the importance of functionalization so as to optimize CNT dispersion within the host.

A study of the spectral position of the G^+ Raman signal of the SWCNTs as an indicator for interaction between the nanotubes and the PMMA matrix yielded a surprising result. Experiments confirmed that laser heating gives rise to a significant downshift of the G^+-peak position with increasing power densities for agglomerated areas. Even in the dispersed phase with a much lower CNT concentration this effect was observed. This is attributed to an increase of local temperature, already observable at the lowest laser power densities for 2.33 eV irradiation. This effect might possibly lead to interpretation errors if this downshift were attributed to other effects. It is therefore very important - especially for CNTs incorporated into a non thermally or electrically conductive matrix - to use a laser power density as low as possible. As our work has shown, in those areas of a composite in which there is some level of aggregation, the heating effects are even greater and may lead even to polymer ablation. Some possible explanations of the agglomerated heating have been proposed but certainly further work is required to answer some of the still-open questions.

In the science and technology of CNT-based composite materials, Raman spectroscopy is a useful and non-destructive means for studying many aspects of the filler to host interaction. This work shows however that certain precautions are absolutely necessary.

7. FUTURE WORK

It was shown that Raman spectroscopy can provide a lot of insight to such complicated systems as functionalized SWCNT based composites. Functionalization indeed promotes the dispersion of the CNT fillers. However the residual non functionalized CNTs might still agglomerate and counteract the benefits obtained by the dispersed tubes. More efficient procedures of the functionalization and the composite synthesis should thus be developed.

Analysis of the RBM Raman mode of the CNTs in agglomerates indicated local differences in the CNTs composition. However, not enough data was collected to clarify if these differences are the exception or the rule.

Pronounced laser heating was observed in the composite material, especially in the CNT aggregates. Moreover, different spots in the dispersed area showed variations in laser heating as well indicating the possibility of a correlation of the laser heating effect with local CNT concentration. Since this effect results in different G-band positions for different spots at the same laser power it might easily lead to interpretation errors if such G-band shifts are attributed to pressure, strain or charge transfer. In order to clarify if laser heating in Raman spectroscopy experiments on CNT composites is a general problem other materials should be examined. Besides different possible reasons for the laser heating effects observed in this study a conclusive answer could not be obtained with the available data thus further experiments are necessary to address the problem of laser heating effects in CNT-based composite materials in general.

8. REFERENCES

1) L. V. Radushkevich, V. M. Lukyanovich, O strukture ugleroda, obrazujucegosja pri termi-ceskom razlozenii okisi ugleroda na zeleznom kontakte, *Zurn. Fisic. Chim.* **1952**, 26, 88.

2) S. Iijima, Helical microtubules of graphite carbon, *Nature* **1991**, 354, 56.

3) S. Ijima, T. Ichihashi, Single-shell carbon nanotubes of 1-nm diameter, *Nature* **1993**, 363, 603.

4) H. O. Pierson, *Handbook of Carbon, Graphite, Diamond and Fullerenes*, Noyes Publications, New Jersey, **1993**.

5) D. Arnett, *Supernovae and Nucleosynthesis*, Princeton University Press, Princeton, New Jersey, **1996**.

6) K. Croswell, *Alchemy of the Heavens*, Anchor Book, New York, New York, **1996**.

7) J. Bennett, M. Donahue, N. Schneider, M. Voit, *Astronomie Die kosmische Perspektive*, Pearson Studium, München, **2010**, Kapitel 17.2.

8) F. Holleman, E. Wiberg, *Lehrbuch der Anorganischen Chemie*, de Gruyter, Berlin – New York, **1985**, Kapitel 16.1.

9) K. S. Novoselov, A. K. Geim, S. V. Morozov, D. Jiang, M. I. Katsnelson, I. V. Grigorieva, S. V. Dubonos, A. A. Firsov, Two-dimensional gas of massless Dirac fermions in Graphene, *Nature* **2005**, 438, 197.

10) H. P. Boehm, A. Clauss, G. O. Fischer, U. Hofmann, Dünnste Kohlenstoff-Folien, *Z. Naturforschg.* **1962**, 17 b, 150.

11) C. N. R. Rao, A. K. Sood, K. S. Subrahmanyam, A. Govindaraj, Graphene: The New Two-Dimensional Nanomaterial, *Angew. Chem. Int. Ed.* **2009**, 48, 7752.

12) H. W. Kroto, J. R. Heath, S. C. O'Brien, R. F. Curl, R. E. Smalley, C_{60} Buckminsterfullerene, *Nature* **1985**, 318, 162.

13) P. A. Thrower, Novel Carbon Materials – What if?, *Carbon* **1999**, 37, 1677-1678.

14) E. Osawa, *Kagaku* **1970**, 25, 854.

15) H. P. Boehm, Carbon from Carbon Monoxide Disproportion on Nickel and Iron Cata-lysts: Morphological Studies and Possible Growth Mechanism, *Carbon* **1973**, 11, 583.

16) A. Oberlin, M. Endo, Filamentous Growth of Carbon Through Benzene Decomposition, *J. Cryst. Growth* **1976**, 32, 335.

17) M. Reibold, P. Paufler, A. A. Levin, W. Kochmann, N. Pätzke, D. C. Meyer, Carbon nano-tubes in an ancient Damascus sabre, *Nature* **2006**, 444, 286.

18) www.amroy.fi (accessed the 14.04.2011)

19) www.nanoscience.com (accessed the 14.04.2011)

20) www.nordicenergysolutions.org (accessed the 14.04.2011)

21) R. Saito, G. Dresselhaus, M. S. Dresselhaus, *Physical Properties of Carbon Nanotubes*, Imperial College Press, London, **1998**.

22) M. J. O'Connell, *Carbon Nanotubes: Properties and Applications*, CRC Press, Boca Raton, **2006**.

23) E. Smith, G. Dent, Modern Raman Spectroscopy: A Practical Approach, John Wiley & Sons Ltd., West Sussex, **2005**.

24) A. Jorio, M. S. Dresselhaus, R. Saito, G. F. Dresselhaus, Raman Spectroscopy in Graphene Related Systems, Wiley-VCH, Weinheim 2011.

25) C. V. Raman, K. S. Krishnan, *Nature* **1928**, 43, 873.

26) H. Kataura, Y. Kumazawa, Y. Maniwa, I. Umezu, S. Suzuki, Y. Ohtsuka, Y. Achiba, *Syn. Met.* **1999**, 103, 2555.

27) http://www.photon.t.u-tokyo.ac.jp/~maruyama/kataura/kataura.html (accessed the 26.04.2011).

28) M.S. Dresselhaus, P.C. Eklund, *Advances In Physics* **2000**, 49, 705.

29) A.M. Rao, E. Richter, S. Bandow, B. Chase, P. C. Eklund, K. A. Williams, S. Fang, K. R. Subbaswamy, M. Menon, A. Thess, R. E. Smalley, G. Dresselhaus, M. S. Dresselhaus, *Science* **1997**, 275, 187.

30) J. Maultzsch, H. Telg, S. Reich, C. Thomsen, Radial breathing mode of single-walled carbon nanotubes: Optical transition energies and chiral-index assignment, *Phys. Rev. B* **2005**, 72, 205438.

31) S. Reich, C. Thomssen, J. Maultzsch, *Carbon Nanotubes: Basic Concepts and Physical Properties*, Wiley-VCH, Weinheim **2004**.

32) U. D. Venkateswaran, E. A. Brandsen, U. Schlecht, A. M. Rao, E. Richter, I. Loa, K. Syassen, P. C. Eklund, High Pressure Studies of the Raman-Active Phonons in Carbon Nanotubes, Phys. Stat. Sol. (b) **2001**, 223, 225.

33) S. B. Cronin, A. K. Swan, M. S. Ünlü, B. B. Goldberg, M. S. Dresselhaus, M. Tinkham, Resonant Raman spectroscopy of individual metallic and semiconducting single-wall carbon nanotubes under uniaxial strain, *Phys. Rev. B* **2005**, 72, 035425.

34) N. T. Alvarez. C. Kittrell, H. K. Schmidt, R. H. Hauge, P. S. Engel, J. M. Tour, Selective photochemical functionalization of surfactant-dispersed single wall carbon nanotubes in water, *J. Am. Chem. Soc.* **2008**, 130, 1422733.

35) M. Terrones, A. G. Filho Souza, A. M. Rao, Doped carbon nanotubes: Synthesis, characterization and applications, Springer Series on Topics in Appl. Phys., 111 (eds. A. Jorio, M. S. Dresselhaus, G. Dresselhaus), Springer-Verlag, Berlin **2008**.

36) N. R. Raravikar, P. Keblinski, A. M. Rao, M. S. Dresselhaus, L. S. Schadler, P. M. Ajayan, Temperature dependence of radial breathing mode Raman frequency of single-walled carbon nanotubes, *Phys. Rev. B* **2002**, 66, 235424.

37) Y. Zhang, L. Xie, J. Zhang, Z. Wu, Z. Liu, Temperature Coefficients of Raman Frequency of Individual Single-Walled Carbon Nanotubes, *J. Phys. Chem. C* **2007**, 111, 14031.

38) F. Huang, K. T. Yue, P. Tan, S.-L. Zhang, Z. Shi, X. Zhou, Z. Gu, Temperature dependence of the Raman spectra of carbon nanotubes, *J. Appl. Phys.* **1998**, 84, 4022.

39) R. B. Capaz, C. D. Spataru, P. Tangney, M. L. Cohen, and S. G. Louie, Temperature dependence of the band gap of semiconducting carbon nanotubes, *Phys. Rev. Lett.* **2005**, 94, 036801.

40) S. B. Cronin, Y. Yin, A. Walsh, R. B. Capaz, A. Stolyarov, P. Tangney, M. L. Cohen, S. G. Louie, A. K. Swan, M. S. Ünlü, B. B. Goldberg, and M. Tinkham, Temperature dependence of the optical transition energies of carbon nanotubes: The role of electron-phonon coupling and thermal expansion, *Phys. Rev. Lett.* **2006**, 96, 127403.

41) Y. Zhang, H. Son, J. Zhang, J. Kong, Z. Liu, Laser-Heating Effect on Raman Spectra of Individual Suspended Single-Walled Carbon Nanotubes, *J. Phys. Chem. C* **2007**, 111, 1988.

42) H. Huang, R. Maruyama, K. Noda, H. Kajiura, and K. Kadono, Preferential destruction of metallic single-walled carbon nanotubes by laser irradiation, *J. Phys. Chem. B* **2006**, 110, 7316.

43) D. Olevik, A. V. Soldatov, M. Dossot, B. Vigolo, B. Humbert, E. McRae, Stability of carbon nanotubes to laser irradiation probed by Raman spectroscopy, *Phys. Stat. Sol. (b)* **2008**, *245*, 2212.

44) N. T. Byrne, Y. K. Gun'ko, Recent Advances in Research on Carbon Nanotube–Polymer Composites, *Adv. Mater.* **2010**, 22, 1672.

45) D. Eder, Carbon Nanotubes – Inorganic Hybrids, *Chem. Rev.* **2010**, 110, 1348.

46) M. M. Shokrieh, R. Rafiee, A Review of the mechanical properties of isolated carbon nanotubes and carbon nanotubes composites, *Mech. Comp. Mat.* **2010**, 46, 155.

47) Z. Spitalsky, D. Tasis, K. Papagelis, C. Galiotis, Carbon nanotube–polymer composites: Chemistry, processing, mechanical and electrical properties, *Prog. Poly. Sci.* **2010**, 35, 357.

48) T. W. Chou, L. Gao, E. T. Thorstenson, Z. Zhang, J. H. Byun, An assessment of the science and technology of carbon nanotube-based fibers and Composites, *Comp. Sci. Tech.* **2010**, 70, 1.

49) N. G. Sahoo, S. Rana, J. W. Cho, L. Li, S. H. Chan, Polymer nanocomposites based on functionalized carbon nanotubes, *Prog. Poly. Sci.* **2010**, 35, 837.

50) D. Roy, S. Bhattacharyya, A. Rachamim, A. Plati, M. L. Saboungi, Measurement of interfacial shear strength in single wall carbon nanotubes reinforced composite using Raman spectroscopy, *J. Appl. Phys.* **2010**, 107, 043501.

51) H. H. So, J. W. Cho, N. G. Sahoo, Effect of carbon nanotubes on mechanical and electrical properties of polyimide/carbon nanotubes composites, *Eur. Polym. J.* **2007**, 43, 3750.

52) B.-K. Zhu, S.-H. Xie, Z.-K. Xu, Y.-Y. Xu, Preparation and properties of the polyimide/multi-walled carbon nanotubes (MWCNTs) nanocomposites, *Comp. Sci. Tech.* **2006**, 66, 548.

53) J. Liu, M. Dossot, D. Olevik, V. Mamane, B. Vigolo, D. Abrahamsson, H. Jonsson,Y. Fort, B. Humbert,A. V. Soldatov,E. McRae, Preferential functionalisation of carbon nanotubes probed by Raman spectroscopy, *Physica E* **2008**, 40, 2343.

54) R. Graupner, Raman spectroscopy of covalently functionalized single-wall carbon nanotubes, *J. Raman Spectr.* **2007**, 38, 673.

55) M. Holzinger, J. Abraham, P. Whelan, R. Graupner, L. Ley, F. Hennrich, M. Kappes, A. Krisch *J. Am. Chem. Soc.* **2003**, 125, 8566.

56) V. G. Hadjiev, M. N. Iliev, S. Arepalli, P. Nikolaev, B. S. Files, Raman scattering test of single-wall carbon nanotube composites, *Appl. Phys. Lett.* **2001**, 78, 21.

57) T.-E. Chang, A. Kisliuk, S. M. Rhodes, W. J. Brittain, A. P. Sokolov, Conductivity and mechanical properties of well-dispersed single-wall carbon nanotube/polystyrene composite, *Polymer* **2006**, 47, 7740.

58) S. Wang, R. Liang, B. Wang, C. Zhang, Load-transfer in functionalized carbon nanotubes/polymer composites, *Chem. Phys. Lett.* **2008**, 458, 371.

59) M. Kalbác, L. Kavan, L. Dunsch, Controlled doping of double walled carbon nanotubes and conducting polymers in a composite: An in situ Raman spectroelectrochemical study, *Comp. Sci. Tech.* **2009**, 69, 1553.

60) K. E. Thomson, D. Jiang, R. O. Ritchie, A. K. Mukherjee, A preservation study of carbon nanotubes in alumina-based nanocomposites via Raman spectroscopy and nuclear magnetic resonance, *Appl. Phys. A* **2007**, 89, 651.

61) A. Bassil, P. Puech, G. Landa, W. Bacsa, S. Barrau, P. Demont, C. Lacabanne, E. Perez, R. Bacsa, E. Flahaut, A. Peigney, C. Laurent, Spectroscopic detection of carbon nanotube interaction with amphiphilic molecules in epoxy resin composites, *J. Appl. Phys.* **2005**, 97, 34303.

62) M. Lamy de la Chapelle, C. Stephan, T. P. Nguyena, S. Lefiant, C. Journet, P. Bernier, E. Munoz, A. Benito, W. K. Maser, M. Martinez, G. F. de la Fuente, T. Guillard, G. Flamant, L. Alvarez, D. Laplaze, Raman characterization of single walled carbon nanotubes and PMMA-nanotubes composites, *Syn. Met.* **1999**, 103, 2510.

63) Q. Zhao, H. D. Wagner, Raman spectroscopy of carbon-nanotube-based composites, *Phil. Trans. R. Soc. Lond. A* **2004**, 362, 2407.

64) M. Baibarac, I. Baltog, S. Lefrant, Raman evidences for the interface interactions in poly(bithiophene)/single-walled carbon nanotubes composites, *Carbon* **2009**, 47, 1389.

65) C. C. Kao, R. J. Young, A Raman spectroscopic investigation of heating effects and the deformation behaviour of epoxy/SWNT composites, *Comp. Sci. Tech.* **2004**, 64, 2291.

66) K. Maehashi, Y. Onno, K. Inoue, K. Matsumoto, Chirality selection of single-walled carbon nanotubes by laser resonance chirality selection method, *Appl. Phys. Lett.* **2004**, 85, 858.

67) B. Vigolo, V. Mamane, F. Valsaque, T. N. Ha Le, J. Thabit, J. Ghanbaja, L. Aranda, Y. Fort, E. McRae, Evidence of sidewall covalent functionalization of single-walled carbon nanotubes and its advantages for composite processing, *Carbon* **2009**, 47, 411.

68) M. Dossot, F. Gardien, V. Mamane, Y. Fort, J. Liu, B. Vigolo, B. Humbert, E. McRae, Optical Parameter to Reveal the Interplay between Covalent Functionalization and the State of Aggregation of Single-Walled Carbon Nanotubes, *J. Phys. Chem. C* **2007**, 111, 12199.

69) L. A. Giannuzi, F. A. Stevie, *Introduction to Focused Ion Beams: Instrumentation, Theory, Techniques and Practice*, Springer 2004.

70) E. Joselevich, Electronic structure and chemical reactivity of carbon nanotubes: a chemist's view, *ChemPhysChem* **2004**, 5, 619.

71) C. Wang, Q. Cao, T. Ozel, A. Gaur, J. A. Rogers, M. Shim, Electronically Selective Chemical Functionalization of Carbon Nanotubes: Correlation between Raman Spectral and Electrical Responses, *J. Am. Chem. Soc.* **2005**, 127, 11460.

72) F. Cataldo, A Raman study on radiation-damaged graphite by γ-rays, *Carbon* **2000**, 38, 623.

73) U. J. Kim, C. A. Furtado, X. Liu, G. Chen, P. C. Eklund, Raman and IR spectroscopy of chemically processed single-walled carbon nanotubes, *J. Am. Chem. Soc.* **2005**, 127, 15437.

74) M. Mases, M. Noël, G. Mercier, M. Dossot, B. Vigolo, V. Mamane, Y. Fort, A. V. Soldatov, E. McRae, *Phys. Stat. Sol. (b)* **2011**, accepted.

75) O. Beyssac, B. Goffe, J.-P. Petitet, E. Froigneux, M. Moreau, J.-N. Rouzaud, On the characterization of disordered and heterogeneous carbonaceous materials by Raman spectroscopy, *Spectrochim. Acta, Part A* **2003**, 59, 2267.

76) S.-K. Sze, N. Siddique, J. J. Sloan, R. Escribano, Raman spectroscopic characterization of carbonaceous aerosols, *Atmos. Environ.* **2001**, 35, 561.
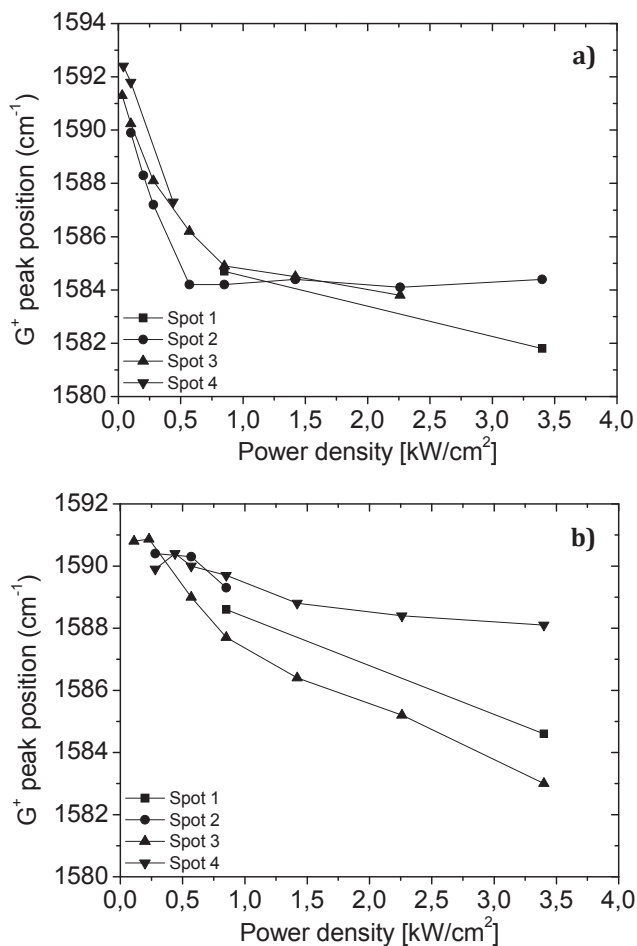
9. APPENDIX

9.1. LASER HEATING EXPERIMENTS ON CNT –PMMA COMPOSITES

2.33 eV excitation:
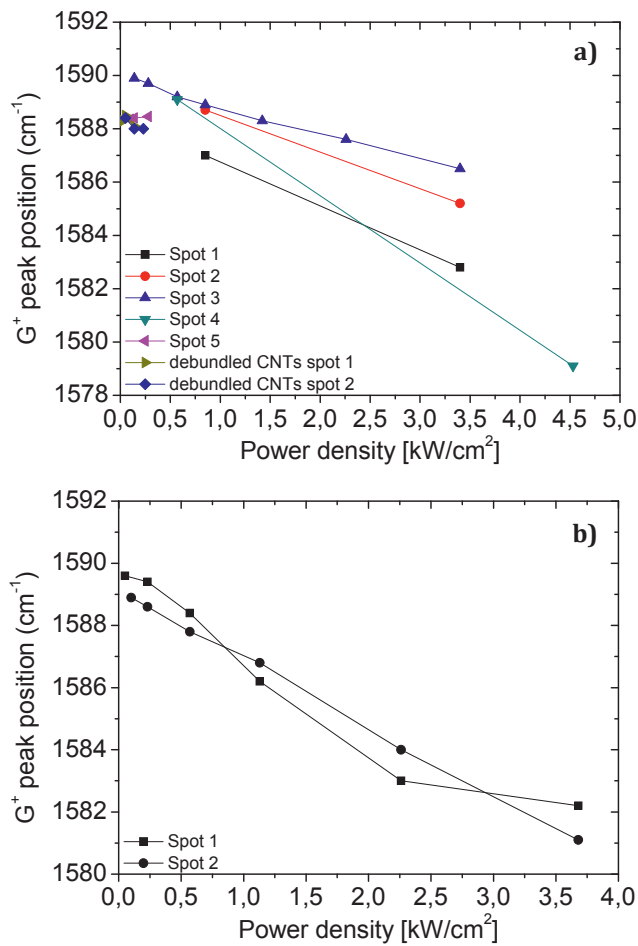
Figure A1. Experimental data from laser heating experiments for pristine CNT material before a) and after functionalization b).

Figure A2. Experimental data from laser heating experiments on composite material of a) areas with agglomerated CNTs and b) areas with dispersed CNTs b).
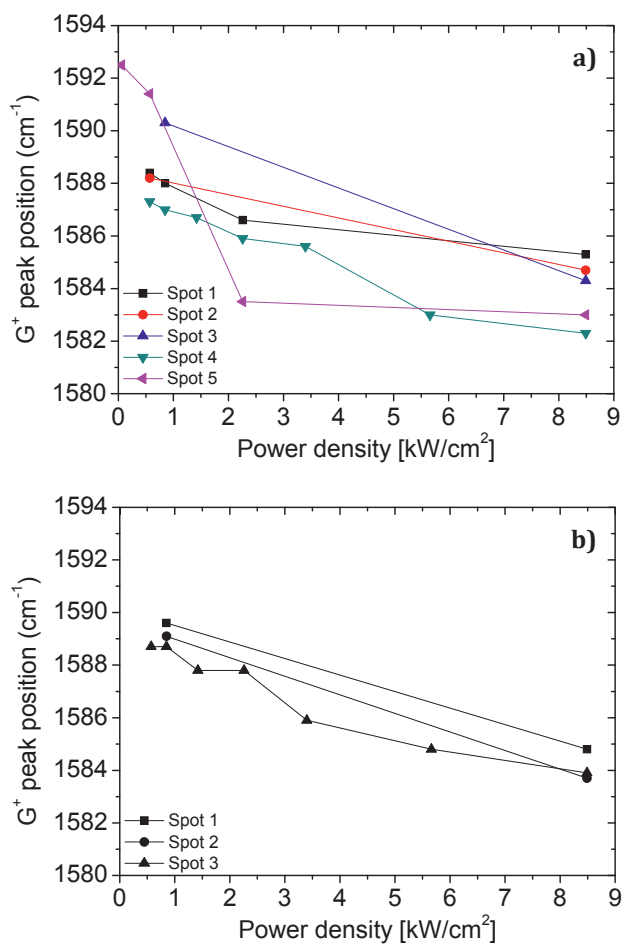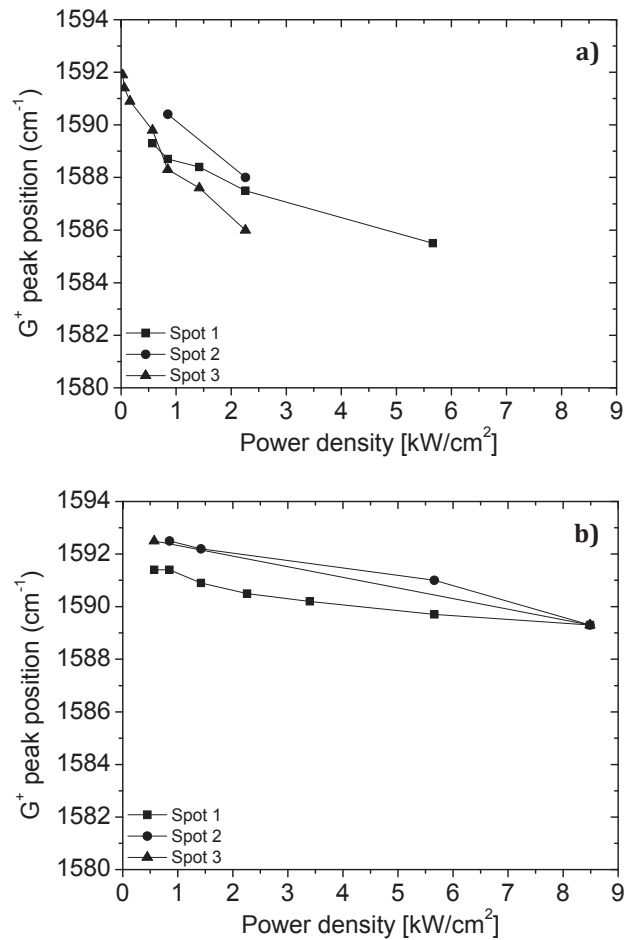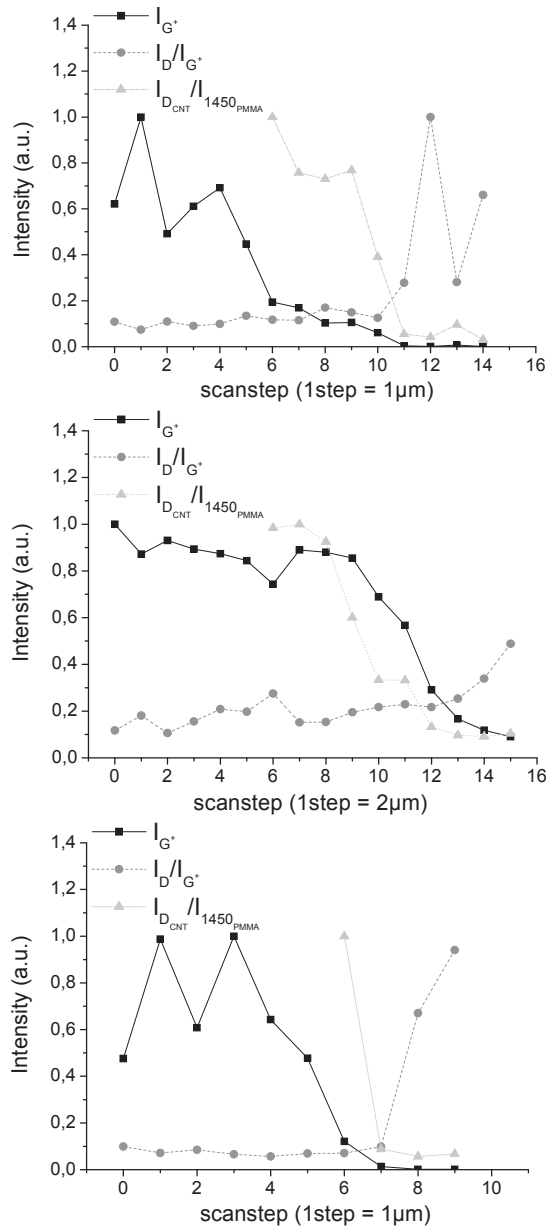
1.96 eV excitation:

Figure A3. Experimental data from laser heating experiments for pristine CNT material before a) and after functionalization b).

Figure A4. Experimental data from laser heating experiments on composite material of a) areas with agglomerated CNTs and b) areas with dispersed CNTs b).

9.2. RAMAN LINE SCANS IN THE CNT –PMMA COMPOSITES

Further experimental data of Raman line scan experiments.

Figure A5. Further experimental data obtained from Raman line scans for green laser (2.33 eV) excitation. G^+ intensities and D*/1450 intensity ratios normalized to max. I_{G^+} and max. $I_{D*}/I_{1450PMMA}$ respectively. I_{D*}/I_{G^+} ratios are not normalized.

Paper 1

Multiscale Characterization of Single-Walled Carbon Nanotube/Polymer Composites by Coupling Raman and Brillouin Spectroscopy

**Brigitte Vigolo,*,† Brice Vincent,† Julien Eschbach,† Patrice Bourson,‡ Jean-François Marêché,†
Edward McRae,† Andreas Müller,§ Alexander Soldatov,§ Jean-Marie Hiver,‖
Abdesselam Dahoun,‖ and Didier Rouxel†**

*Institut Jean Lamour, CNRS - Nancy Université - UPV Metz, BP 70239, 54506 Vandoeuvre-lès-Nancy, France,
Laboratoire Matériaux Optiques, Photoniques et Systèmes, Université de Metz et Supélec, UMR 7132,
2 rue E. Belin, 57070 Metz, France, Department of Applied Physics & Mechanical Engineering, Luleå
University of Technology, SE - 97187 Luleå, Sweden, and Institut Jean Lamour, CNRS - Nancy
Université - UPV Metz, Ecole des Mines, Parc de Saurupt, 54042 Nancy, France*

The present paper reports on an original experimental approach to the characterization of SWNT/polymer composites. This work deals with the multiscale characterization of nanocomposites. Covalently functionalized SWNTs were incorporated in a PMMA matrix using an in situ polymerization procedure. We show that their presence does not affect the radical polymerization process. Combining Brillouin and Raman spectroscopy, we were able to associate the obtained mechanical properties of the material at the macroscopic scale to the state of functionalization of the SWNTs within the polymer matrix.

1. Introduction

Carbon nanotubes (CNTs) have generated a huge amount of activity because experimental and theoretical studies have led to the prediction of many fields of application for this extraordinary molecule. In particular, the outstanding Young's modulus of SWNTs (single-walled carbon nanotubes) combined with their flexibility and lightness make them ideal fillers for high performance nanocomposites.[1] SWNTs thus incorporated inside a polymer matrix could significantly improve the properties of the polymeric materials. The main requirements for the elaboration of composites with an effective integration of a filler are (i) good interfacial properties between the CNT surface and the polymer matrix and (ii) proper dispersion of CNTs within the matrix. The difficulty is that CNTs have poor affinity for almost all solvents, melted polymers, or monomers and consequently show a high tendency to form agglomerates. Chemical treatments such as acid attack or covalent functionalization of the CNT surface appear as the most efficient ways to modify the surface properties of the CNTs and improve their incorporation within the polymer matrix.[2] However, these treatments must be done in a controlled way to avoid damaging the CNT structure and consequently alteration of their intrinsic physical properties.[3] For low functionalization levels, SWNTs within the composite may consequently be only partially dispersed. These obtained inhomogeneous composites are difficult to characterize.[4,5] In the literature, the reported elastic properties cover quite a large domain[6] and the disappointing reinforcement generally obtained is poorly understood.[7–9] The difficulty partly arises from the need for multiscale characterization of such materials.

The development of tools which are able to relate the nanoscale features of the CNTs themselves and of the CNT−matrix interface to the composite properties at a macroscopic scale is of paramount importance in the case of nanotube-based materials.[10]

We propose an original coupling between two inelastic optical scattering techniques: Brillouin and Raman spectroscopy. Working at two different frequency ranges (GHz for Brillouin scattering and THz for Raman spectroscopy), it was possible to relate structural and chemical features at the scale of the chemical bonds within the composites to their macroscopic elastic properties. Moreover, for each characterization technique, the size of the studied zone could be modified by adjusting the size of the spot irradiating the sample. We have especially paid attention to the sample heterogeneities in order to obtain reproducible results independent of the studied zone of the sample. For Brillouin experiments, the SWNT concentration in the composites is the main constraint; indeed the samples must be transparent so the SWNT concentration could not exceed 0.05 wt % in our composites. This technique is highly sensitive and robust and it allows the determination of the elastic properties of extremely small samples compared to those required for other commonly used techniques (DMA, mechanical traction, etc.).

In this work, the preparation of SWNT−poly(methyl methacrylate) composites is based on a *grafting from* process and an in situ polymerization described elsewhere.[11] Results obtained using Brillouin spectroscopy show that elastic properties of the composite are unfortunately degraded upon increasing the SWNT concentration. Common macroscopic characterization techniques such as differential scanning calorimetry (DSC) and wide angle X-ray scattering (WAXS) reveal that the polymerization process itself is not affected by the presence of SWNTs in our procedure. By means of confocal Raman spectroscopy, characteristics of the composites at micrometric and nanometric scales are discussed relative to macroscopic structural and mechanical properties.

---

* Corresponding author. Tel: +33 383684641; fax: +33 383684615, e-mail: Brigitte.Vigolo@lcsm.uhp-nancy.fr (B.V.).
† Institut Jean Lamour, CNRS - Nancy Université - UPV Metz, BP 70239, 54506 Vandoeuvre-lès-Nancy.
‡ Université de Metz et Supélec.
§ Lulea University of Technology.
‖ Institut Jean Lamour, CNRS - Nancy Université - UPV Metz, Ecole des Mines.

Single-Walled Carbon Nanotube/Polymer Composites

J. Phys. Chem. C, Vol. 113, No. 41, 2009 **17649**
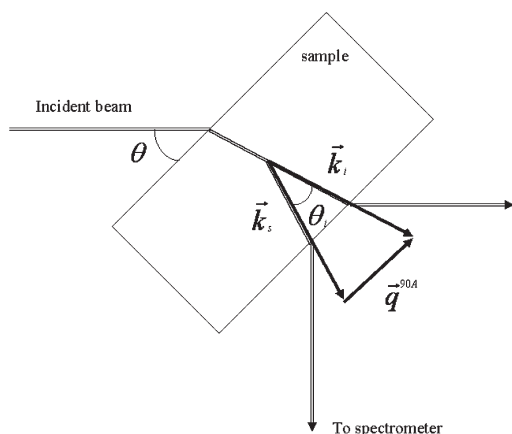
Figure 1. 90A scattering geometry where $\vec{k}_i$ is the wavevector of the incident photon, $\vec{k}_s$ is the wavevector of the detected scattered photon, and $\vec{q}^{90A}$ the wavevector of the involved phonon.

2. Experimental Section

2.1. Sample Preparation. The SWNTs used for the preparation of the composites were synthesized by an arc discharge method and provided by Carbolex Inc. We have developed a chemical procedure consisting of covalently grafting functional groups on the SWNT bundle surface. The procedure leads to low levels of functionalization in order to preserve intrinsic SWNT properties. It has been shown that the functionalized SWNTs bear only 1 function per 70−100 carbon atoms.[11] For the composite preparation, functionalized SWNTs are dispersed in a monomer solution of methyl methacrylate (MMA). Radical polymerization is directly initiated within an MMA solution using benzoyl peroxide as initiator.[12] Poly(methyl methacrylate) (PMMA) was chosen because of its transparency which allows use of the optical techniques. We have shown in previous work that this procedure is able to create covalent bonds between the SWNT surface and the PMMA chains.[11] The SWNT concentration of the obtained series of composites is varied from 0.013 to 0.6 wt %. For inelastic Brillouin scattering characterizations, only samples having the adequate transparency can be used, thus requiring concentrations no higher than 0.05%.

2.2. Analysis Techniques. For Brillouin spectroscopy, in our geometry (see Figure 1), the interaction between the incident beam and the material leads to a frequency shift (f) of the scattered laser light, directly related to the propagation velocity (v) of the acoustic phonons by the relation:

$$v = \frac{f \times \lambda_0}{\sqrt{2}} \tag{1}$$

where λ_0 is the incident wavelength.

The relation between velocity and the wave vector q is simplified as follows:

$$v = \frac{2\pi f}{q} = \frac{\lambda_0 f}{2n \sin\left(\dfrac{\theta_i}{2}\right)} \tag{2}$$

since $\sin(90 - \theta) = n \sin((\theta_i)/(2))$, where n is the refractive index of the material.

The scattered light was analyzed by a 5-pass Fabry−Perot interferometer and then detected by a photon counting photomultiplier linked to a multichannel analyzer. Our experimental setup was composed of an Ar laser (wavelength: 514.5 nm) and two Pockels cells. These cells are synchronized with the scan rate and the frequency window of the interferometer and used to attenuate the elastically scattered spectral light. The particular scattering geometry, with the incident laser beam at an angle of 45° with respect to the faces of our sample and the scattered light also collected perpendicular to the incident beam, is named 90A[13,14] (Figure 1); it permits the determination of acoustic velocity without requiring knowledge of the refractive index.[15] This is a key point because the refractive index of a nanocomposite is usually unknown and difficult to measure.

Differential scanning calorimetry (DSC) was carried out with a Perkin-Elmer DSC7 apparatus. Prior to the measurement, the sample was cycled from 20 to 150 °C to relax any residual stress within the composites, and then the DSC response was recorded over the same temperature range.

Wide-angle X-ray scattering (WAXS) was used to study the evolution of the structure of PMMA[16] as a function of the CNT concentration in the composites, by means of a 2D diffraction system (Inel, France) equipped with a copper anode. The selected voltage and current were 30 kV and 40 mA, respectively. The wavelength used was that of $K_{\alpha 1}$ copper radiation ($\lambda_{Cu\alpha 1} = 0.154$ nm), selected by means of a parabolic multilayer mirror (Osmic) and a very thin capillary. The 2D transmission pattern was recorded with a scanner which has a resolution of 25 μm. The samples were parallelepipeds with a thickness of 0.8 mm.

Two different experimental set-ups were used for Raman characterization. The first one is a Labram 010 (Jobin-Yvon) spectrometer with a confocal microscope and a cooled CCD detector. A traditional microscope, in which the whole observed field is illuminated, offers low axial resolution which does not allow depth discrimination of the images of the various planes of a thick object. The irradiating beam had a diameter of 50 μm with the 10× objective, and the irradiating wavelength used was 514.5 nm. The second experimental set-up was a confocal Raman microscope-based WiTec CRM-200 imaging system. Spectra were collected with 1 cm^{-1} resolution. The samples were excited with a 532 nm laser, and the incident power was measured directly on the microscope sample stage. For characterization of the SWNT polymer composites, the experimental conditions used for recording the spectra are of crucial importance. Heating due to laser irradiation even at commonly used power densities can induce modification or even disappearance of Raman features.[17] In order to minimize these effects, spectra shown in this paper were recorded at low power densities in the range of 0.28 kW/cm^2 to 1.7 kW/cm^2 for which the irradiation-provoked heating effects were negligible for the purpose of this work. Such effects in CNT−PMMA composites will be addressed in detail in a forthcoming publication.

3. Results

3.1. Composite Characterization at the Macroscopic Scale. The inelastic scattering of incident photons within a material results from the interaction of these incident photons with the material of interest inducing the creation or the annihilation of an acoustic phonon. The Brillouin scattering technique allows recording the scattered light as a function of its frequency (in the GHz domain). The characteristic frequency can be related to the elastic constants of the samples.[18] The main advantage of this nondestructive technique is that the required size of
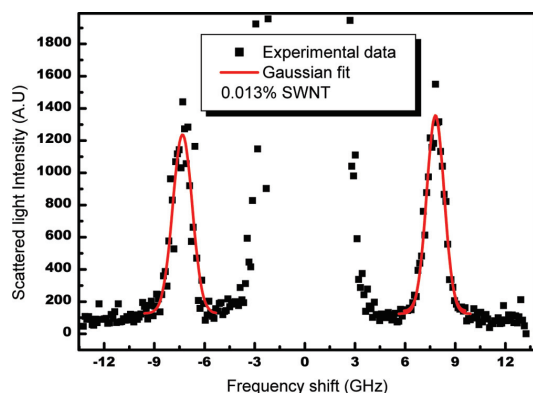
Figure 2. Typical Brillouin response of a SWNT−PMMA composite (CNT concentration 0.013 wt %).

samples is significantly smaller than for other measurement techniques such as DMA (dynamical mechanical analysis) or conventional traction tests. The reproducibility of our Brillouin measurements was straightforwardly checked by changing the position of the incident laser spot on the same sample. The "probe beam diameter" (of several hundred micrometers) was especially chosen to be large compared to the size of the aggregates formed from undispersed CNTs in order to obtain an overall elastic constant for each composite. Furthermore, measurements on two series of samples have shown similar results: both reproducibility and accuracy for the measured elastic constants were excellent. A typical Brillouin spectrum for our samples is shown in Figure 2.

The Stokes and anti-Stokes responses were systematically fitted. The resonant frequency for this sample corresponds to the maximum of the Gaussian peaks around 7.7 GHz. Considering the weak concentrations of SWNTs (less than 0.05 wt %), we assume that the composite density does not depend on the SWNT concentration and corresponds to a mean value of $\rho = 1190$ kg/m^3; the Poisson constant is fixed at $\upsilon = 0.4$ for all the samples. The Young's modulus E' can be expressed using the Brillouin characteristic frequency:

$$E' = C_{11}\frac{(1 - 2\upsilon)(1 + \upsilon)}{1 - \upsilon} \tag{3}$$

then

$$E' = \rho\left(\frac{f\lambda_0}{\sqrt{2}}\right)^2\frac{(1 - 2\upsilon)(1 + \upsilon)}{1 - \upsilon} \tag{4}$$

where $\lambda_0 = 514.5$ nm.

The mechanical properties obtained for a series of samples in which the SWNT concentration varies from 0 to 0.048 wt % are reported on Figures 3a and 3b. The mechanical properties of the composites illustrated in Figure 3 diminish linearly as the concentration of CNTs increases. Young's modulus is reduced by almost 10% for only 0.05 wt % of CNTs in the composite.

A structural investigation of the matrix in the composites was done using DSC and WAXS. Figure 4 shows the evolution of the glass transition temperature (T_g) as a function of SWNT concentration. A much wider range of concentration was

investigated than for the Brillouin scattering, up to 0.6 wt %. No significant modification of T_g (around 117 °C) is observed as the concentration of SWNTs is increased in the composites.

WAXS diagrams for the same CNT concentration domain as that for the DSC investigation are shown in Figure 5. The curves are intentionally shown without normalization to CNT concentration in the composites in order to emphasize their similarity. The presence of CNTs seems to induce no modification of the structural characteristics of PMMA chains. PMMA is amorphous at room temperature and shows the expected broadened peaks instead of well-structured sharp peaks. The most intense peak of nonsymmetric character is probably due to the presence of several contributions.[19] The main contribution around 13.6° which corresponds to 0.65 nm is related to an intermolecular distance within the PMMA matrix. The shoulder at 17° corresponding to 0.52 nm is due to the periodicity of the ester groups within PMMA chains. The large contribution around 30°, corresponding to 0.30 nm, is reported to be the mean distance between methyl and ester groups within a PMMA chain. Whatever the CNT concentration, the WAXS signature of the PMMA in the composites is in agreement with the commonly observed molecular structure of pure PMMA.

The above techniques have allowed sample characterization at a macroscopic scale; however, the results do not point to the exact origin of the observed decrease of the elastic constant as a function of the CNT concentration. Moreover, they are inconsistent with the alteration of the polymerization quality due to the presence of SWNTs as has been reported for radical polymerization processes. On the basis of DSC and WAXS analyses, the in situ polymerized PMMA matrix itself does not seem to be affected by the presence of the SWNTs in our composite preparation procedure because the characteristics (T_g and scattered peak positions) of PMMA remain unchanged as SWNTs are added to the composites. While the molecular weight of the PMMA chains was not investigated for these composites, a significant modification of the length of the polymer chains would induce a variation of T_g (inversely proportional to the molecular weight). These results are also consistent with the fact that we have not observed any modification of the polymerization kinetics with the increase of the SWNT concentration even for the most concentrated sample (0.6 wt %). These observations imply that contrary to other reported polymerization procedures,[8,9] in particular using AIBN (2,2′-azobisisobutyronitrile) as initiator, the surface of the SWNTs does not react during the polymerization process: SWNT functionalization is due only to the functionalization procedure used prior to the in situ polymerization step.

3.2. Analysis at the Micro- and Nanometric Scale. Raman features of SWNTs are sensitive to chemical treatments and especially to covalent functionalization. It is well-known that the intensity of the D band due to the introduction of disorder in the SWNT sp^2 structure increases after functionalization.[20,21] It has also been occasionally reported that a second disorder-induced band can appear as an additional feature of the overall G band.[22,23] For nonfunctionalized SWNTs, the G band has two principal components, designated the G$^-$ and G$^+$ bands. The functionalization process may induce a high-frequency shoulder located at about 1610 cm^{-1} and is referred to as the G* band. For our composites, we could more easily follow modifications of the G band which is more intense than the D band. Moreover, PMMA itself manifests a Raman peak around 1334 cm^{-1}, in the D band domain of the SWNTs.

Raman spectroscopy was used here to characterize both the PMMA component of the composite and the SWNTs incorpo-
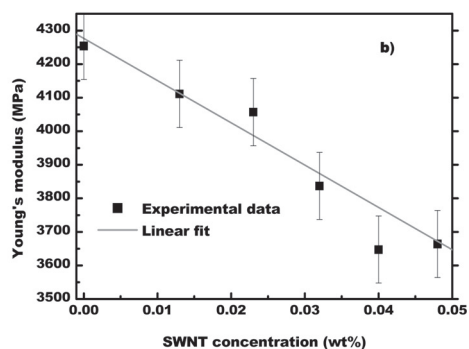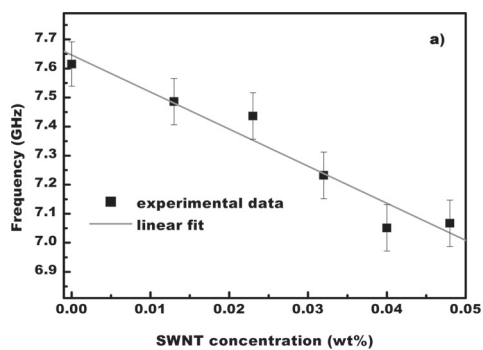
Figure 3. Mechanical properties as a function on CNT concentration in the composites: (a) characteristic frequency; (b) Young's modulus.
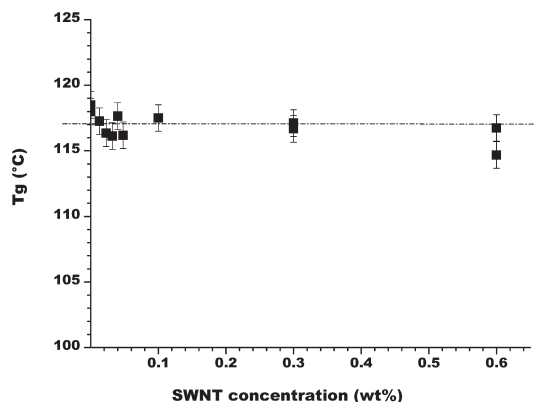

Figure 4. Evolution of T_g as a function of the CNT concentration in the composites. Dashed line is a guide for the eyes.
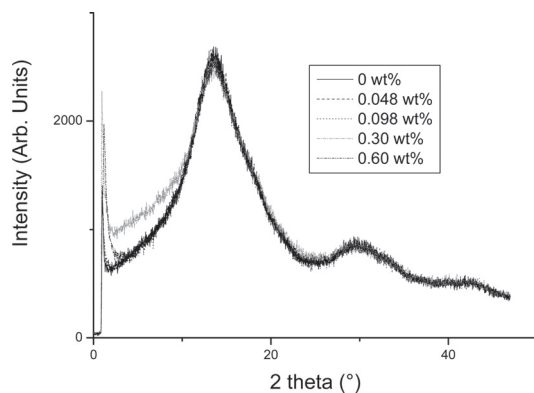

Figure 5. WAXS curves obtained on SWNT−PMMA composites. Each curve was normalized to the maximum of the major peak obtained for pure PMMA.

Figure 6. Typical Raman spectra obtained for the samples (excitation wavelength 532 nm). (a) Pristine SWNTs, (b) functionalized SWNTs, (c) aggregated SWNTs in composites, (d) dispersed SWNTs in composites, (e) pure PMMA.

rated within it. A typical spectrum of synthesized PMMA shows several bands attributed to vibrations of different groups.[24] For the wavenumber range we are interested in, the C=O stretching band appears around 1710 cm^{-1} and the C=CH bending modes at 1500 and 1460 cm^{-1}. Asymmetric deformation of CH$_2$ is shown around 1334 cm^{-1}. For incomplete polymerization, there is an additional peak around 1640 cm^{-1} corresponding to C=C stretching in MMA.[25] This bond is expected to be attacked through a radical polymerization mechanism, leading to the
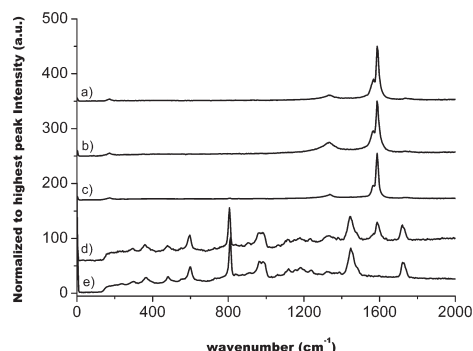
formation of PMMA during in situ polymerization. For our composites, a very weak shoulder around 1640 cm^{-1} was only visible for the most concentrated samples, meaning that in agreement with WAXS and DSC results, the polymerization is not affected by the presence of SWNTs. Figure 6 shows typical Raman spectra recorded for these composites in comparison with those of PMMA and SWNT samples. Spectrum a in Figure 6 is typical of pristine SWNTs with a RBM band in the low frequency domain; the D band and the G band are around 1350 cm^{-1} and 1600 cm^{-1}, respectively. Spectrum b corresponds to the functionalized SWNTs used in the composites studied in this work. As expected in the case of chemically modified SWNTs, the D band intensity is increased compared to that of the pristine sample. For recording spectrum c, the laser spot was focused on a large aggregate in order to record the signal due to the SWNTs belonging to the aggregates; it is similar to that of pristine SWNTs. If we focused the spot on a well dispersed zone of the composite, we obtained signals from both the PMMA (see spectrum e) and the G band of SWNTs which is visible around 1600 cm^{-1} in between two PMMA bands (spectrum d).

As mentioned above, D band modifications are commonly taken as a signature of SWNT functionalization. As one PMMA band is located within the D band zone, we focused our analysis on the G band, the modifications of which can indeed help in the characterization of functionalization levels of SWNT surface. Figure 7 shows the G band of SWNTs belonging to the aggregates (Figure 7a) and those dispersed within the matrix (Figure 7b). According to the Kataura plot,[26] only the semi-
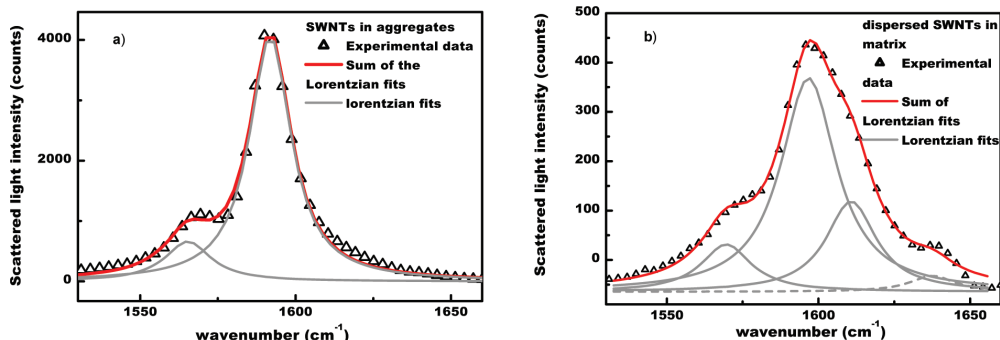
Figure 7. Shapes of the G bands of SWNTs in aggregates (a) and dispersed in matrix (b).
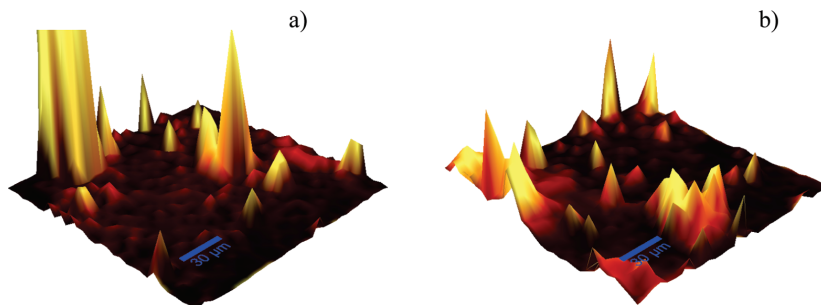

Figure 8. G$^+$ Raman intensity maps for (a) 0.013 wt %, (b) 0.097 wt % SWNT−PMMA composites (excitation wavelength 532 nm).

conducting SWNTs are in resonance when using the green laser excitation (514 or 532 nm). The G band can then be fitted with two Lorentzian peaks as in the case of pristine SWNTs, one corresponding to the G$^-$ mode located at 1566 cm^{-1} and the other to the G$^+$ mode at 1591 cm^{-1} (Figure 7a). For SWNTs dispersed within the matrix, a shoulder (referred to as the G* band) at high wavenumber is added to the conventional G band. In this case, three Lorentzian peaks are required to fit the data. The additional peak is located around 1611 cm^{-1} in Figure 7b. A weak-intensity peak (dashed line) is observed around 1636 cm^{-1}. It corresponds to the stretching of the C=C bonds of MMA monomers remaining in the composites. As a G* component is sometimes observed for defective SWNTs after funtionalization, modifications in the shape of the G band can be taken as manifestations of different states of functionalization of the SWNTs within the composites. Separation between nonfunctionalized SWNTs and functionalized SWNTs has occurred during the polymerization process, the first type aggregating and the second type being dispersed within the PMMA.

Mapping of the SWNT distribution in the composite was done using the spectral imaging mode of a WiTEC CRM 200 confocal Raman microscope with an excitation wavelength of 532 nm and a spot size of approximately 10 μm. The laser scanned over a sample surface area of 186 × 186 μm^2 and 24 × 24 Raman spectra were acquired with 10 s integration time each. Figure 8 shows the 2-D mapping of the Raman intensity of the G$^+$ component for typical surface areas of SWNT−PMMA composites. Assuming that there is no diameter-dependent CNT segregation in the composite, the intensity of this Raman mode is then proportional to the SWNT concentration at any given point (spot) in the samples, and therefore the G$^+$ intensity distribution represents that of the SWNTs in the composite.
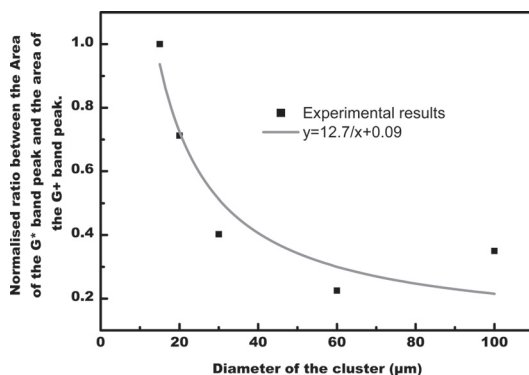

Figure 9. Evolution of the ratio between the area of the G* band and that of the G$^+$ band (I_{G*}/I_{G^+}) as a function of the diameter of the agglomerate located in the irradiated volume, i.e., the volume of the interfacial zone.

Spectral images were collected for composites with CNT concentrations of 0.013 wt %, 0.023 wt %, 0.048 wt %, and 0.097 wt %. Typical scans are shown in Figure 8 for 0.013 wt % and 0.097 wt %. The heterogeneities that are evident in Figure 8 were further investigated to gain greater insight into the state of functionalization of the SWNTs within the aggregates. Experimentally, the spot size was fixed at about 50 μm (the depth of analysis being about the same). It is thus focused on differently sized aggregates close to the sample surface. When the aggregate size is small enough, the recorded signal represents a significant contribution from the CNTs dispersed in the matrix outside the agglomerated regions. For larger sized agglomerates, the relative contribution from the better dispersed zones of the

Single-Walled Carbon Nanotube/Polymer Composites

J. Phys. Chem. C, Vol. 113, No. 41, 2009 **17653**
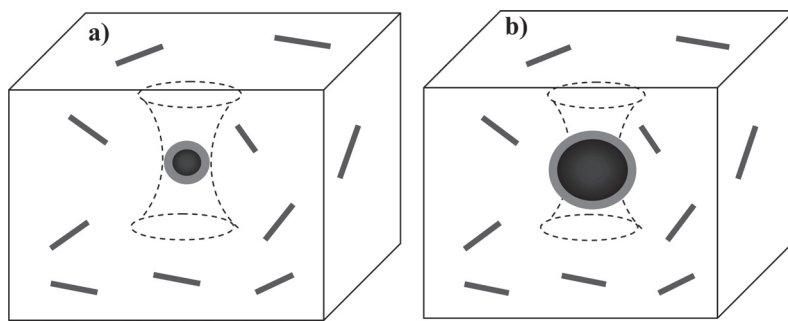
Figure 10. Scheme illustrating the irradiation geometry for Raman spectra recorded in the case of (a) aggregates smaller than the spot size and (b) aggregates larger than the spot size.

surrounding matrix diminishes. The obtained G bands of the SWNTs were analyzed using three main contributions (Lorentzian curves) corresponding to the G^-, the G^+, and the G^* bands. Figure 9 shows the variation of the ratio I_{G^*}/I_{G^+} as a function of agglomerate size over the range $15-100$ μm, for a constant spot size of 50 μm. Below 50 μm, the spot size is larger than the irradiated aggregate (Figure 10a), and for aggregates larger than 50 μm, the recorded Raman zone is smaller than the diameter of the irradiated aggregates (Figure 10b). Interestingly, for irradiated aggregates larger than the spot size in the $50-100$ μm range, the G band still has a significant G^* contribution as observed in Figure 9. The main reasons are that, first, the focused aggregate is not directly at the surface of the composite but is slightly embedded in the matrix and, second, the irradiated volume does not have a bidimensional shape but rather a cylindrical volume centered on the aggregate (Figure 10). As a result, both the SWNTs located on the aggregate surface and the SWNTs situated within the aggregate significantly contribute to the recorded Raman signal. I_{G^*}/I_{G^+} decreases as the size of the agglomerates is increased. The curve in this figure shows that the decrease is consistent with a $1/x$ law. We assume that the SWNTs which are partially functionalized or nonfunctionalized tend to remain agglomerated although the well-functionalized SWNTs are bonded to the PMMA chains within the composite. We do not take into account well dispersed SWNTs outside the aggregates because their contribution is negligible compared to that of aggregated SWNTs in much higher concentration in the aggregates. For decreased radii of the agglomerates, R_{ag}, the number of SWNTs which are partially functionalized or nonfunctionalized decreases as R_{ag}^3. For the functionalized SWNTs positioned at the agglomerated surface, their number is proportional to R_{ag}^2. The resulting behavior of I_{G^*}/I_{G^+} is then expected to follow a $1/R_{ag}$ law as illustrated in Figure 9. We have shown that CNTs well dispersed in the matrix are functionalized. The results of Figure 9 strongly suggest that SWNTs which are situated on the surface of the agglomerates are functionalized and, more importantly, their contribution to the G^* signal is much larger than those distributed in the polymer matrix, surrounding the aggregates. Even if SWNTs within the aggregates are not functionalized, it is possible that SWNT bundles close to the external surface of these aggregates are covalently bonded to the matrix through the in situ polymerization process. These SWNTs are indeed expected to behave similarly to SWNTs well dispersed within the matrix as was shown in a previous work.[11] However, these aggregates remain large inclusions which may be responsible for the decrease of the mechanical properties of these composites. As the SWNT concentration is increased, even if both that of the

aggregates and that of the dispersed functionalized bundles are simultaneously increased, the behavior of the mechanical properties remains governed by the concentration of the aggregates. While it is hoped that the well dispersed bundles inside the PMMA matrix will be responsible for the mechanical reinforcement, this effect is overcome by the inclusion of brittle zones due to the SWNT aggregates.

4. Conclusion

The homogeneous functionalization of individual CNTs which would then allow their homogeneous dispersion within a polymer matrix remains a complex hurdle to overcome. Nevertheless, this work has shown that the combination of analytical techniques allowing both nanoscale and macroscale characterization may shed light in this direction. The results presented here strongly support the idea that the smaller, better-functionalized CNT bundles, well dispersed within the matrix, play a positive role in improving Young's modulus of nanocomposites, but this may be detrimentally overcome by the presence of macroscopic agglomerates.

References and Notes

(1) Lau, K.-T.; Hui, D. *Composites, Part B:* **2002**, *33*, 263.
(2) Liu, P. *Eur. Polym. J.* **2005**, *41*, 2693.
(3) Garg, A.; Sinnott, S. B. *Chem. Phys. Lett.* **1998**, *295*, 273.
(4) Friedler, B.; Gojny, F. H.; Wichmann, M. H. G.; Nolte, M. C. M.; Schulte, K. *Compos. Sci. Technol.* **2006**, *66*, 3115.
(5) Dubois, P.; Alexandre, M. *Adv. Eng. Mater.* **2006**, *8*, 147.
(6) Ramanthan, T.; Liu, H.; Brinson, L. C. *J. Polym. Sci.* **2005**, *43*, 2269.
(7) Gorga, E.; Lau, K. K. S.; Gleason, K. K.; Cohen, R. E. *J. Appl. Polym. Sci.* **2006**, *102*, 1413.
(8) Selmi, A.; Friebel, C.; Doghri, I.; Hassis, H. *Compos. Sci. Technol.* **2007**, *67*, 2071.
(9) Zhu, L.; Narh, K. A. *Polym. Int.* **2004**, *53*, 1461.
(10) Thostenson, E. T.; Chou, T.-W. *J. Phys. D: Appl. Phys.* **2003**, *36*, 573.
(11) Vigolo, B.; Mamane, V.; Valsaque, F.; Le, T. N. H.; Thabit, J.; Ghanbaja, J.; Aranda, L.; Fort, Y.; McRae, E. *Carbon* **2009**, *47*, 411.
(12) Wigg, P. J. C.; May, P. W.; Smith, D. *Diamond Relat. Mater.* **2003**, *12*, 1766.
(13) El Hakiki, M.; Eschbach, J.; Rouxel, D.; Vincent, B.; Vialle, S.; Krüger, J. K.; Elmazria, O.; Alnot, P. *Ferroelectrics* **2007**, *351*, 1.
(14) Eschbach, J.; El Hakiki, M.; Rouxel, D.; Vincent, B.; Vialle, S.; Krüger, J. K.; Elmazria, O.; Alnot, P. Proceedings of the IEEE International Ultrasonics Symposium, Vancouver, October 3–6, 2006, p 1189.

(15) Sanctuary, R.; Bactavatchalou, R.; Müller, U.; Possart, W.; Alnot, P.; Krüger, J. K. *J. Phys. D: Appl. Phys.* **2003**, *36*, 2738.

(16) Kakudo, M.; Kasai, N. *Acta Cryst.* **1974**, *A30*, 460.

(17) Olevik, D.; Soldatov, A. V.; Dossot, M.; Vigolo, B.; Humbert, B.; McRae, E. *Phys. Status Solidi* **2008**, *245*, 2212.

(18) Eschbach, J.; Rouxel, D.; Vincent, B.; Mugnier, Y.; Galez, C.; Le Dantec, R.; Bourson, P.; Krüger, J. K.; Elmazria, O.; Alnot, P. *Mater. Sci. Eng.* **2007**, *27*, 1260.

(19) Lovell, R.; Windle, A. H. *Polymer* **1981**, *22*, 175.

(20) Graupner, R. *J. Raman Spectrosc.* **2007**, *38*, 673.

(21) Hudson, J. L.; Jian, H.; Leonerd, A. D.; Stephenson, J. J.; Tour, J. M. *Chem. Mater.* **2006**, *18*, 2766.

(22) Cataldo, F. *Carbon* **2000**, *38*, 623.

(23) Kim, U. J.; Furtado, C. A.; Liu, X.; Chen, G.; Eklund, P. C. *J. Am. Chem. Soc.* **2005**, *127*, 15437.

(24) Edwards, H. G. M.; Johal, K. S.; Johnson, A. F. *Vibr. Spectrosc.* **2006**, *41*, 160.

(25) Fischer, D.; Sahre, K.; Abdelrhim, M.; Voit, B.; Sadhu, V. B.; Pionteck, J.; Komber, H.; Hutschenreuter, J. *C.R. Chimie* **2006**, *9*–1419.

(26) Kataura, H.; Kumazawa, Y.; Maniwa, Y.; Umezu, I.; Suzuki, S.; Ohtsuka, Y.; Achiba, Y. *Synth. Met.* **1999**, *103*, 2555.

Paper 2

Raman study of inhomogeneities in carbon nanotube distribution in CNT–PMMA composites

Andreas Mueller[1], Brigitte Vigolo[2], Edward McRae[2], and Alexander V. Soldatov*,[1,3]

[1] Department of Applied Physics and Mechanical Engineering, Luleå University of Technology, 97187 Luleå, Sweden
[2] Institut Jean Lamour, CNRS – Nancy Université – UPV Metz, BP 70239, 54506 Vandoeuvre-lès-Nancy, France
[3] Department of Physics, Harvard University, Cambridge, Massachusetts 02138, USA

* Corresponding author: e-mail **alexander.soldatov@ltu.se**, Phone +46 920 491136; Fax +46 920 491074

This work is aimed at characterization of the carbon nanotube (CNT) distribution in polymethyl methacrylate (PMMA)–CNT composites by high-resolution Raman spectroscopy. In particular, we focus on study of the boundary regions between the CNT aggregates and the surrounding areas where the CNTs are well dispersed in the PMMA matrix. Different laser excitation energies (1.96 and 2.33 eV) were used to preferentially probe metallic and semiconducting SWCNTs, respectively. At both photon energies, spectral line scans across the boundary regions were performed revealing a substantial drop in intensity of G^+ CNT Raman mode and an increase of the D/G^+-intensity ratio. The latter testifies to a preferential dispersion of functionalized CNTs in the PMMA matrix. Certain inhomogeneities were observed by Raman spectral imaging even in the areas with well-dispersed CNTs.

1 Introduction Since the identification of carbon nanotubes (CNTs) by Ijima in 1991 [1], this material has become a subject of great interest and effort in science because of the outstanding physical properties it exhibits. CNTs can be thought of as graphene sheets rolled into seamless cylinders of various diameters and in principle infinite length. Depending on the number of concentrically arranged tubes, CNTs are termed single-walled (SWCNT), double-walled (DWCNT), and multi-walled (MWCNT) CNTs. Moreover SWCNTs exist as semiconducting or metallic types, depending on the orientation of the hexagonal lattice relative to the tube axis, as classified by the chiral indices (n,m). Their extraordinary mechanical, electrical, thermal, and optical properties render them very attractive for a wide range of applications [2, 3] including advanced composite materials.

However synthesis of CNT-based composite materials still remains a big challenge. In particular it remains to overcome the difficulties in achieving good nanotube dispersion within the matrix material. The fact that present synthesis routes produce SWCNTs in a bundled state due to van der Waals intertube interaction is another serious hurdle,

as SWCNT bundles do not exhibit the excellent properties of their individual components. Thus special treatment has to be applied in order to break these bundles. In an ideal composite material, the individual SWCNTs would be homogeneously dispersed in the matrix. A second issue is the interaction between the CNTs and the host: to improve the load transfer between host and filler covalent linking between the two components is desirable.

One approach to solve these problems is functionalization of the CNT source material prior to its incorporation into the polymer matrix. Optimization is required to maximize the transfer from the polymer to the CNTs but minimize the number of wall defects created by the covalent grafting of the functional groups on the CNT sidewalls. Moreover appropriate functional groups have to be chosen to assure compatibility with the polymer being used.

In order to understand and improve the microstructure of CNT composites and relate it to mechanical, electrical, or thermal properties, advanced characterization methods have to be applied. Raman spectroscopy has proven to be a powerful tool for studying both pure CNT materials [2, 4–11] and CNT-based composites [12–16]. Synthesis of the

polymethyl methacrylate (PMMA) composite material used here, based on functionalized SWCNTs, was reported recently and its study revealed inhomogeneities in the CNT distribution within the polymer and associated degradation in the mechanical properties suggested as being attributed to the presence of CNT agglomerates [17, 18]. The CNT distribution in the samples was illustrated by Raman spectral mapping of the G^+-peak intensity as a function of position.

The present work is aimed at investigation of the interface region between the SWCNT agglomerates and the areas with well-dispersed nanotubes in CNT–PMMA composites by Raman imaging and spectral line scanning across these areas. In addition, we examined inhomogeneities in the CNT distribution in the "dispersed" regions by following the G band/ PMMA Raman intensity ratio and downshift of the G band due to laser heating.

2 Experimental procedures After functionalization with phenyl–ester groups, SWCNTs were incorporated into a PMMA matrix by *in situ* polymerization [17]. A sample containing 0.097 wt.% functionalized SWCNT loading was used for this study.

Raman measurements were conducted with a WiTEC CRM 200 confocal Raman imaging system in a back-scattering geometry. In order to preferentially probe semiconducting or metallic SWCNTs and thus be able to distinguish any different behavior due to electronic structure, two different laser excitation wavelengths were used, namely 532 and 633 nm (corresponding to 2.33 and 1.96 eV, respectively). Raman spectra were collected using a 600 g/mm diffraction grating. The laser beam was focused on the sample surface onto a spot of 1 or 3.45 μm in diameter using a 100× or 20× objective, respectively. Laser powers were measured directly on the sample stage and were typically between 0.5 and 1.5 mW.

As illustrated in Fig. 1a, 2D spectral imaging allowed selecting large CNT agglomerates for further detailed examination. Raman line scans were performed starting within an agglomerate and ending in the dispersed area in order to study the boundary region. An example of such a scan – a resulting set of consecutive equally spatially separated Raman spectra – is presented in Fig. 1b. A piezo scanner permitted 1 μm scan steps.

3 Results and discussion Raman spectra from different CNT aggregates in the composite were acquired. All line scans showed the general features illustrated in Fig. 1b. Inside the agglomerated area no peaks related to the PMMA matrix are seen – only the CNTs contribute to the high intensity of the Raman spectrum. At some point a big drop in Raman intensity of the signal from CNTs occurs along with the appearance of peaks related to PMMA.

After acquisition, the Raman spectra were fitted by Lorentzian peak shapes. Typical peak fitting results of the Raman data from line scans in the aggregates of different sizes are presented in Fig. 2 for both the 1.96 and 2.33 eV excitation energies. It merits noting that the peak at 1330 cm^{-1} corresponds to a combination of the SWCNTs D-band and a small peak due to PMMA. From this point on, this combined peak will be denoted as D* to discern it from the pure D-band peak of CNTs. The G^+-peak intensity, the D*/G$^+$-intensity ratio and the intensity ratio of the D* to the PMMA peak at 1450 cm^{-1} (D*/1450-intensity ratio) are plotted against the spatial position in Fig. 2. The D*/1450-intensity ratio was chosen because it reflects the contribution of the PMMA spectrum to the overall observed Raman spectrum of the composite. G$^+$ intensity and D*/1450 ratio were normalized to their maximum values.

The Raman signal of CNTs (evidenced by the G$^+$ intensity in Fig. 2) is not only very inhomogeneous regarding different areas in the composite (agglomerated areas and dispersed areas) but also shows inhomogeneities in an agglomerated region itself in some cases (Fig. 2a). However at some given scan step a large drop in G$^+$ intensity occurs accompanied by the appearance and decrease of the D*/1450-intensity ratio. At the same time the D*/G$^+$-intensity ratio increases. After a certain transition region all three ratios stabilize at new levels. We attribute this transition region (indicated by broken lines in Fig. 2) to the boundary interface area between the agglomerates and dispersed areas.

The boundary interface width is found to be about 4 μm for an agglomerate of ~30 μm big while it is about 20 μm wide for an agglomerate of ~66 μm (Fig. 2a and b, respectively), which is indicative of its dependence on the agglomerate size. With 1.96 eV photon energy we probe predominantly the metallic nanotubes in our sample while the semiconducting ones are in resonance with 2.33 eV
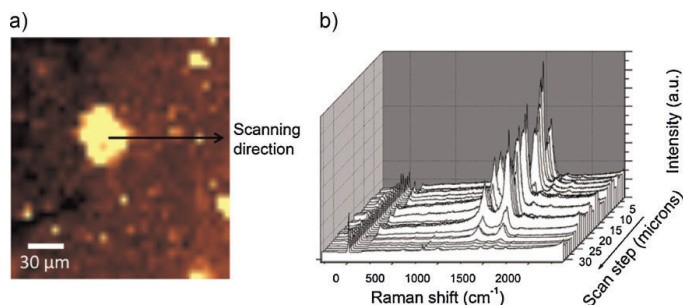
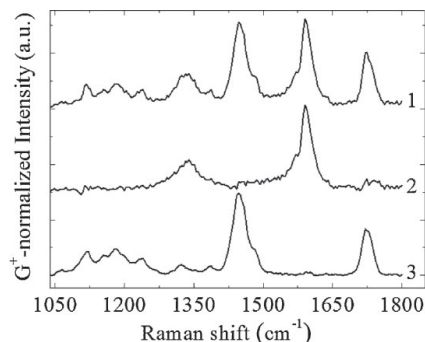Figure 1 (online color at: www.pss-b.com) Raman spectral map of maximum G$^+$ intensity in CNT–PMMA composite (a) indicating CNT aggregates (bright spots). The blue arrow denotes direction of the spectral line scan (b) starting in the aggregate and ending in the dispersed area. Each spectrum in (b) corresponds to one step scan of 1 μm. Spectra were collected at 1.96 eV photon excitation energy.
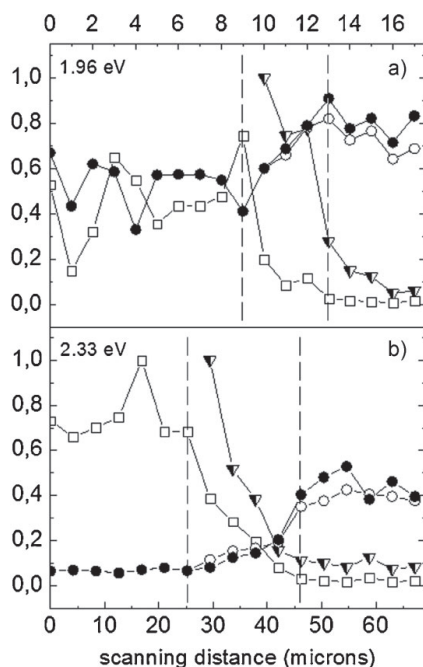
Figure 2 Raman data obtained from line scans through the aggregated/dispersed area boundary in different aggregates for (a) 1.96 eV and (b) 2.33 eV photon excitation energy. Symbol assignment: I_{G+} and $I_{D*}/I_{1450PMMA}$ (normalized to their maximum values) – empty squares and half filled triangles, respectively; I_{D*}/I_{G+} – filled circles; I_D/I_{G+} (after subtraction of PMMA contribution) – empty circles. The interface regions between agglomerate (left side) and dispersed areas (right side) are indicated by vertical lines. Note different horizontal axis scale in (a) and (b).
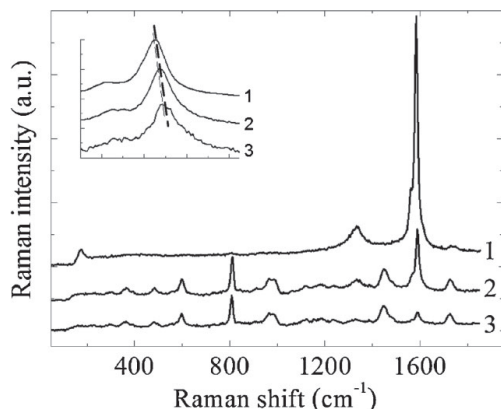

Figure 3 Raman spectra of composite dispersed area before (1) and after (2) subtraction of pure PMMA spectrum (3). Spectra collected with 2.33 eV photon excitation energy.

photons. Analysis of the line scans across the boundary interface area does not reveal any significant difference in behavior of metallic versus semiconducting CNTs – both exhibit the same overall trends, i.e., drop of I_{G+} while increase of I_{D*}/I_{G+}. However, the metallic nanotubes show a higher level of I_{D*}/I_{G+} both inside the agglomerates and in the dispersed area. This could indicate a higher degree of functionalization with phenyl–ester groups of metallic compared to the semiconducting CNTs as was shown earlier [4, 5].

As mentioned above both SWCNTs and PMMA show a peak at around 1330 cm^{-1} (Fig. 3), complicating the interpretation of the D*/G$^+$-intensity ratio. Since no PMMA peaks are observable in agglomerates, it can be assumed that this peak is only due to the CNT – signal, thus reflecting the real D band. However it is not trivial to separate the contribution of the CNT or PMMA signal to this peak in a boundary region or in the dispersed area of the composite as the PMMA contribution cannot be neglected in these cases.

This raises the question if the observed increase of the D*/G$^+$-intensity ratio could simply be due to an increase of the PMMA contribution to the spectrum. To address this issue, the PMMA contribution was removed from the composite spectrum by subtraction of a reference PMMA spectrum (Fig. 3) followed by new peak fitting. The resulting corrected D/G$^+$ values are shown together with the uncorrected ones in Fig. 2 for both excitation energies. The corrected D/G$^+$ values are indeed lower than the uncorrected values which demonstrates that the PMMA contribution cannot be neglected for dispersed regions. However the corrected values are still significantly higher than those observed in agglomerated areas. It can thus be concluded that the observed increase of the D/G$^+$-intensity ratio going from agglomerated to dispersed regions is not due to only a higher PMMA contribution in the composite spectrum. With the corrected D/G$^+$ ratio the line scans can now be fully interpreted. Firstly the drop of G$^+$ intensity indicates a decrease of CNT concentration from agglomerate to dispersed region. Furthermore, the increase of the D/G$^+$ ratio indicates a higher defect level of the SWCNTs in the dispersed area. As functionalized CNTs are generally known to exhibit increased D-band intensities [4] this observation leads us to the conclusion that the fraction of functionalized CNTs is higher in the dispersed phase than in the agglomerates.

Further we observed inhomogeneities in the dispersed area itself as indicated by different G-band intensities relative to the PMMA peaks (Fig. 4).

Moreover these intensity variations are accompanied by a difference in the G$^+$-peak position – a more intense G band exhibits a larger G$^+$-peak downshift from its position in the source CNT material. Actually this observation holds not only for the dispersed area but can be extended to the agglomerates exhibiting much larger G$^+$ downshifts.

As the detailed analysis of these observations goes beyond the scope of this article, we refer to an upcoming work which will comprise a more detailed study of the D/G$^+$-

Figure 4 Raman spectra of CNT agglomerate (1) and two different spots (2 and 3) in the dispersed area of composite collected at 15.6 kW/cm^2 with 2.33 eV photon excitation energy. Inset: G-band area of the spectra normalized to maximum G$^+$ intensity. The line drawn through G-band maxima is just guide to the eyes.

intensity ratio of both the PMMA–CNT composites and the source SWCNT material before and after functionalization [19].

4 Conclusions In summary we studied the boundary region between SWCNT aggregates and the dispersed phase of a SWCNT–PMMA composite material by Raman imaging. The width of this boundary area varies with the agglomerate size. A drop in G$^+$ intensity accompanied by an increase of the D/G$^+$ ratio was observed from aggregated to dispersed area indicating a lower CNT concentration and also that the dispersed phase contains preferentially functionalized SWCNTs. Furthermore, we observed inhomogeneities in CNT distribution even in the dispersed phase stemming from the G-band intensity difference and downshift.

References

[1] S. Ijima and T. Ichihashi, Nature **363**, 603 (1991).
[2] R. Saito, G. Dresselhaus, and M. S. Dresselhaus, Physical Properties of Carbon Nanotubes (Imperial College Press, London, 1998).
[3] M. S. Dresselhaus, G. Dresselhaus, and P. C. Eklund, Science of Fullerenes and Carbon Nanotubes (Academic Press, New York, 1996).
[4] J. Liu, M. Dossot, D. Olevik, V. Mamane, B. Vigolo, D. Abrahamsson, H. Jonsson, Y. Fort, B. Humbert, A. V. Soldatov, and E. McRae, Physica E **40**, 2343 (2008).
[5] R. J. Graupner, Raman Spectrosc. **38**, 673 (2007).
[6] M. Holzinger, J. Abraham, P. Whelan, R. Graupner, L. Ley, F. Hennrich, M. Kappes, and A. J. Krisch, J. Am. Chem. Soc. **125**, 8566 (2003).
[7] N. R. Raravikar, P. Keblinski, A. M. Rao, M. S. Dresselhaus, L. S. Schadler, and P. M. Ajayan, Phys. Rev. B **66**, 235424 (2002).
[8] Y. Zhang, L. Xie, J. Zhang, Z. Wu, and Z. Liu, J. Phys. Chem. C **111**, 14031 (2007).
[9] Y. Zhang, H. Son, J. Zhang, J. Kong, and Z. Liu, J. Phys. Chem. C **111**, 1988 (2007).
[10] U. D. Venkateswaran, E. A. Brandsen, U. Schlecht, A. M. Rao, E. Richter, I. Loa, K. Syassen, and P. C. Eklund, Phys. Status Solidi B **223**, 225 (2001).
[11] S. B. Cronin, A. K. Swan, M. S. Ünlü, B. B. Goldberg, M. S. Dresselhaus, and M. Tinkham, Phys. Rev. B **72**, 035425 (2005).
[12] A. Bassil, P. Puech, G. Landa, W. Bacsa, S. Barrau, P. Demont, C. Lacabanne, E. Perez, R. Bacsa, E. Flahaut, A. Peigney, and C. Laurent, J. Appl. Phys. **97**, 34303 (2005).
[13] M. Lamy de la Chapelle, C. Stephan, T. P. Nguyena, S. Lefrant, C. Journet, P. Bernier, E. Munoz, A. Benito, W. K. Maser, M. Martinez, G. F. de la Fuente, T. Guillard, G. Flamant, L. Alvarez, and D. Laplaze, Synth. Met. **103**, 2510 (1999).
[14] Q. Zhao and H. D. Wagner, Phil. Trans. R. Soc. Lond. A **362**, 2407 (2004).
[15] C. C. Kao and R. J. Young, Comp. Sci. Technol. **64**, 2291 (2004).
[16] V. G. Hadjiev, M. N. Iliev, S. Arepalli, P. Nikolaev, and B. S. Files, Appl. Phys. Lett. **78**, 21 (2001).
[17] B. Vigolo, V. Mamane, F. Valsaque, T. N. Ha Le, J. Thabit, J. Ghanbaja, L. Aranda, Y. Fort, and E. McRae, Carbon **47**, 411 (2009).
[18] B. Vigolo, B. Vincent, J. Eschbach, P. Bourson, J. F. Marêché, E. McRae, A. Müller, A. Soldatov, J. M. Hiver, A. Dahoun, and D. Rouxel, J. Phys. Chem. C **113**, 17648 (2009).
[19] A. Mueller, B. Vigolo, E. McRae, and A. Soldatov, unpublished.

Paper 3

Raman study of CNT – PMMA composites: some functionalization and thermal effects

Andreas Mueller,[1] Brigitte Vigolo,[2] Victor Mamane,[3] Yves Fort,[3] Edward McRae,[2]

Alexander V. Soldatov,[,1,4]*

[1] Department of Engineering Sciences & Mathematics, Lulea University of Technology, SE - 97187

Luleå, Sweden

[2] Institut Jean Lamour, CNRS - Nancy Université – UPV Metz, UMR 7198, BP 70239, 54506

Vandœuvre-lès-Nancy, France

[3] Laboratoire de Synthèse Organométallique et Réactivité, Université Henri Poincaré - Nancy

Université, UMR 7565 CNRS, BP 70239, 54506 Vandœuvre-lès-Nancy, France

[4] Department of Physics, Harvard University, Cambridge, MA-02138, USA

* Corresponding author. Tel: +46 (0)920 491136

e-mail: alexander.soldatov@ltu.se

1

Abstract.

We have carried out a resonant Raman spectroscopy study of a composite material made of a PMMA polymer host and functionalized SWCNTs and of the source SWCNT material before and after functionalization. In order to preferentially probe metallic and semiconducting SWCNTs, two laser excitation energies (1.96 and 2.33 eV) were used. Examination of the D/G$^+$-intensity ratio of the SWCNT material before incorporation into the composite showed a higher value for functionalized than for the raw SWCNTs. Furthermore, the metallic nanotubes exhibited a higher degree of functionalization. Raman spectral imaging revealed some inhomogeneities of the CNT distribution in the composite material: the spectra of the areas with good CNT dispersion in the composite exhibit a higher D/G$^+$-intensity ratio than in areas with CNT agglomerates indicating that functionalized CNTs are preferentially dispersed in the polymer matrix while non functionalized ones tend to group together in agglomerates. This underlines the importance of functionalization so as to optimize CNT dispersion within the host. We observed a significant laser heating of the SWCNTs in composites resulting in a downshift of the G$^+$-peak position which was much more pronounced in agglomerates than in the areas with dispersed CNTs and detected at the very lowest laser irradiances. Such an effect might possibly lead to Raman data interpretation errors if this downshift was attributed to other effects, for example, enhancement of CNT-host interaction in composites. We conclude that laser heating effects generally accompany Raman characterization of CNT-based composite systems especially for nanotubes incorporated into a non thermally or electrically conductive matrix and underscore the importance of monitoring these effects even at the low laser irradiance levels typically used in Raman experiments.

Keywords.

2

1. Introduction

As well documented in a number of recent review articles[1-5], composite materials are one of the most promising fields for the application of carbon nanotubes (CNTs) because their unique structure and extraordinary mechanical, electrical and thermal properties suggest them to be the perfect filler material. Among CNTs, single-walled carbon nanotubes (SWCNTs) occupy a special position. Consisting of just one graphene sheet rolled into a seamless tube, their diameters range from a few to less than one nanometer, and this results in very high aspect ratios and truly one-dimensional (1D) electronic character. Although there are many studies reporting significant improvement of various properties of composite systems fabricated by CNT incorporation[1-5], the full potential of CNTs has still not been reliably and reproducibly attained.

Two problems in particular arise during the synthesis of CNT-based composites which must be overcome. Firstly, the dispersion of the filler within many matrices is still a challenge since SWCNTs form bundles due to strong van der Waals attraction and the bundles themselves tend to agglomerate even further. Homogeneously dispersed SWCNTs within the composite are essential in order to maximally benefit from their presence.

A second issue is the interactions between the CNTs and the host matrix. For optimal load transfer between host and filler, covalent linking between the two components is desirable. However optimization is required to both maximize the load transfer from polymer to CNTs and minimize the number of wall defects created by the covalent grafting of the functional groups on the CNT sidewalls. Optimization is further required as concerns the choice of the functional group to make it compatible with the polymer being used.[1-5]

One approach to solve these two problems is functionalization of the CNT source material prior to incorporation into the host.[1,2,4,6] Roy et al.[7] reported, for instance, an increased load transfer by the use of CNT grafting by collagen which resulted in a greater critical shear stress. Others prepared carboxylic functionalized MWCNT/polyimide composites reporting much better CNT dispersion

3

and CNT-matrix interaction, both reflected in improved mechanical properties.[8,9]   In spite of these works which do indeed indicate some improved mechanical characteristics linked to the presence of the CNTs, the two above-mentioned difficulties are still serious hurdles to be overcome in a predictable and controlled manner.

For characterization of CNT-based composite systems, Raman spectroscopy is an analysis technique of interest since it requires only little or no sample preparation and may be non destructive. Moreover, Raman spectroscopy has been, and still is, extensively used to study different effects on pristine CNTs, such as those of functionalization[8,10,11] or of debundling treatments[12], temperature effects[13-16] as well as pressure or strain effects.[17,18]   This knowledge of CNTs may be exploited in analyzing composite systems incorporating CNTs. Several research groups have employed Raman spectroscopy to measure interfacial shear strength and load transfer[7,19-21] or to analyze doping by the matrix of the CNT fillers[22] while others have investigated the physical state of the CNTs, e.g. their structural integrity[23] after incorporation, the dispersion behavior[19,24,25], CNT orientation[26] or the CNT interaction with the matrix material.[27]

Frequently, the spectral positions of one of the CNT Raman features, e.g. the G-band or D-band, which are known to be sensitive to outer influences (e.g. pressure, strain, charge transfer, temperature), are used for such studies.[7,19,21,24,26,28]   However, the spectral positions of the CNT Raman modes are also known to be sensitive to incident laser power density due to heating effects.[15,29,30] Although this can seriously complicate interpretation of Raman results, very little information of these effects in composite materials is available in the literature. Kao et al.[28] did report on laser heating of SWCNTs in an epoxy incoporating non-functionaliezd SWCNTs, showing more pronounced laser heating for the raw SWCNTs powder sample than for the SWCNTs incorporated in the composite.

Using resonant Raman spectroscopy, the present work reports a detailed study of the effect of functionalization on the dispersion of CNTs within a SWCNT-PMMA composite[31] and associated

4

laser heating effects. This composite was found in earlier work[32] to exhibit some inhomogeneity regarding CNT distribution in the material and poorer mechanical properties than expected, associated with the presence of CNT agglomerates. A Raman investigation of the areas of very high CNT concentration suggested this to be correlated with a low fraction of functionalized CNTs.[33] Furthermore, in the agglomerated areas and even in some areas in the phase with well dispersed CNTs, significant G-band downshifts were observed whose origin remained unclear at that time.

In the new work presented here, the study is extended to the CNT material in its various states before incorporation in the matrix. We focus on the role of functionalization in the composite using the D/G^+ intensity ratio as a criterion for the degree of functionalization. Substantial laser heating is found to be the reason for the large G-band downshifts at different areas in the composite leading sometimes even to ablation of the polymeric material.

2. Experimental

The SWCNTs used in this study were synthesized by the electric arc discharge method and provided by Carbolex Inc. They were used without purification and in the following will be termed the "raw sample". Methoxyphenyl groups were attached to the SWCNT surface following a free radical procedure.[31,34] The obtained functionalized samples are denoted SWCNT-PhMeO. The methoxyphenyl groups were subsequently modified using two steps in order to obtain SWCNTs grafted by phenolic ester groups (SWCNT-PhEster) which are polymerizable and thus able to act as bridges between the SWCNT surface and the PMMA matrix. These two functionalization steps modify only the PhMeO- side groups which were attached to the CNTs in the first step but do not affect the nanotube's surface structure any further.[34] The composites were prepared using an in-situ polymerization process. The desired quantity of SWCNT-PhEster sample was added to an MMA solution containing 0.5 wt% of benzoyle peroxide as initiator. For homogeneization, the mixture was gently sonicated using a probe tip sonicator before polymerization initiation.

5

Raman measurements were done on raw SWCNTs, functionalized SWCNTs (SWCNT-PhMeO) and a composite sample containing 0.097 wt% SWCNT-PhEster.

A WiTEC CRM 200 confocal Raman system in backscattering geometry was used for all measurements. As in the previous work[32,33], 2.33 eV and 1.96 eV excitation energies were used (corresponding to 532 nm and 633 nm wavelengths respectively) in order to preferentially probe semiconducting or metallic SWCNTs respectively and thus be able to distinguish any different behavior due to electronic structure. Raman spectra were collected using either a 600 gr/mm or a 1800 gr/mm (for laser heating experiments) diffraction grating. Laser powers were measured directly on the sample stage and were from 0.05 to 3.68 mW. The laser beam was focused on the sample surface onto a spot of 1 or 3.45 µm in diameter using a 100X or 20X objective respectively. Spectral image scans were done according to the procedure described elsewhere[32] and Raman spectra were taken in agglomerated and dispersed areas in the composite. The spectra were peak fitted to determine the D/G^+-intensity ratio.

Fits to the D band were made with one Lorentzian peak. For fits to the G band at 2.33 eV (excitation of semiconducting tubes), three Lorentzian peaks were used to model the G^+, G^- and G* components: this was also done for the 1.96 eV spectra in addition to a Breit-Wigner-Fano lineshape since at this photon energy metallic tubes are excited. By G*, we refer to the peak sometimes observed between about 1605 and 1620 cm^{-1} either in strongly disordered carbonaceous materials or in CNTs following functionalization.

Laser heating experiments were performed using the 20X objective. High resolution Raman spectra were taken at the same spot on the sample starting with the lowest possible power to acquire a decent quality spectrum before going to higher powers. The acquired spectra were peak fitted and the G^+-peak position was plotted against laser power density.

6

3. Results

Figure 1 shows Raman spectra of the raw SWCNT and the SWCNT-PhMeO samples for 1.96 and 2.33 eV excitation energies. Based on the peak-fitted Raman spectra at both energies, Table 1 gives the ratio I_D/I_{G+}, of integrated D to G^+ band intensity (the former sensitive to the number of defects induced by the chemical treatment, the latter being the tangential vibrational mode): As observed in the table, the first functionalization step increases the ratio by a factor of about three.

When the further-functionalized SWCNT-PhEster is integrated into the PMMA matrix, these CNTs will be dispersed according to the state of functionalization of the individual bundles or tubes. The more they are functionalized, the more their dispersion will be favored. As a result, the D/G^+-intensity ratio in the CNT-composite can provide information about the spatial distribution of the functionalized CNTs in the host. Figure 2 shows representative examples of the G-band region taken on the composite in CNT-agglomerated (top) and -dispersed (middle and bottom) regions. The middle panel of figure 2 clearly illustrates the preponderant contribution of the PMMA matrix in the Raman spectrum of the dispersed area. Table 1 shows average values of the integrated I_D/I_{G+} ratio determined for a typical agglomerated and dispersed composite area.

It is interesting that analogous to raw and functionalized SWCNTs for which the latter manifest a higher D/G^+-intensity ratio, the CNTs in the dispersed parts of the composite also manifest a I_D/I_{G+}, value greater than that of the agglomerated regions: Furthermore, for both laser energies, the highest values are observed for the composite dispersed areas, the highest value of all being for the 1.96 eV irradiation which probes the metallic tubes. For both energies, the ratio for the agglomerated areas is somewhat less than those of the functionalized CNTs before introduction into the polymer matrix.

While studying these composite materials we noted a large downshift of the G-band in agglomerated areas compared to dispersed areas. Figure 3 illustrates this observation by showing two Raman spectral maps. Figure 3(a) shows the G^+-intensity manifesting the CNT concentration and Figure 3(b) shows the G^+-peak position. Areas of high CNT concentration are very closely

7

correlated with those having a large downshift of the same band. It should be noted that the G^+-peak position of the dispersed area lies in the region where it is expected for pristine CNTs, i.e. around 1588-1590 cm^{-1}.

It was found some time ago that the G-band position of CNTs is influenced by temperature: higher temperature leads to a G-band downshift.[14-17,35] Therefore laser heating experiments (as described in the experimental section) were performed for the four previously-mentioned systems: raw CNTs, functionalized CNTs, agglomerated and dispersed composite areas. After peak fitting, the G^+-peak position values were plotted against laser power density and subsequently fitted by simple linear fits for laser power densities up to 20 kW/cm^2 (at higher power densities deviation from linear behavior was observed) to obtain peak shift rates.

Figure 4 and table 2 show the results obtained. Let us first examine Figure 4. The only immediately obvious result illustrated here is that in all cases an increasing power density causes a G^+ downshift. At both laser energies, the smallest variation is noted for one of the dispersed areas within the composite and the greatest temperature sensitivity is noted for the agglomerated areas within the composite. Many more results have been utilized in establishing the average values given in Table 2. These data represent the overall behavior in spite of significant sample-to-sample variations for a given type of the four "systems" studied. The heating rates are calculated from peak shifts based on the equation[14]:

$$\Delta T = -\Delta\omega(G^+)/0.0258 \qquad (1)$$

Within a given type of sample, the spot-to-spot variations differ by less than a factor of about three except for the spots examined in the agglomerated region of the composite at the higher photon energy; raw and functionalized CNTs show nearly the same values (1.96 eV) or slightly higher values for functionalized tubes in the case of 2.33 eV excitation energy. For both excitations, the G^+-peak position shift of agglomerated regions is about 5-6 times stronger than in dispersed regions. Furthermore, as illustrated for the agglomerated area of figure 4, this strong shift observed

8

already at a very low power density, e.g., less than 0.54 kW/cm^2 which was a lower limit to acquire

a decent CNT Raman signal in the composite. In fact, we could not find a power-density (PD)

sufficiently low in which for this part of the composite, the G$^+$-peak position was fully stabilized

independent of the incident laser power density. It was found that shift rates of the dispersed regions

are about the same as for raw and functionalized CNTs (2.33 eV) or smaller (1.96 eV). Table 2

clearly illustrates that the shift rates are always higher for the higher photon energy laser light.

Finally, we observed in several experiments using this excitation energy that the G$^+$-peak position

against laser PD for agglomerates showed leveling starting at a PD > 10 kW/cm^2.

It seems that the shift rate increases with increasing G$^+$-intensity, i.e. local CNT concentration.

This is illustrated in figure 5b where we have plotted the observed G-band shift rates in three points

of the composite (see figure 5a for their Raman spectra), one in an agglomerate and two in two

different positions in the dispersed area, against their maximum G-band intensity.

We return to the plateau observed on Figure 4 for the composite cluster region using green laser

excitation. This was not observed in any other laser heating experiment done in this work. In an

additional experiment, images of the probed spot on the composite surface were taken in between

every power increase. It was observed (Figure 6) that an ablation mark appeared at the same power

density as the leveling of the G-band shift. Furthermore, Raman spectra (figure 6, left panel) show

that at a certain laser power the absolute intensity of the signal goes down. This can only be caused

either because a) the probed surface came out of focus due to ablation of material or b) the number

of scatterers, i.e. nanotubes, decreased possibly through heat-induced damage on tubes or c) a mix

of the two. The temperature of the nanotubes when the plateau started to appear was between 325

and 425 °C (estimated from G-band shift), well above the melting and boiling points of neat PMMA

which are about 160 and 200°C respectively.

9

4.   Discussion

4.1. Functionalized SWCNTs.

The functionalization procedure used allows obtaining SWCNTs that have been chemically modified as expected. However, because of the high tendency of as-produced CNTs to agglomerate, it is very difficult to obtain uniformly-functionalized tubes in any given sample. Indeed, the high surface energy associated with the van der Waals forces tends to maintain the inter-tube binding and even functionalization can generally not fully separate the bundles. In this case, the outer walls of bundles´ outer tubes are strongly grafted, as volumetric adsorption experiments have shown.[31] A second point concerning the uniformity of functionalization is that earlier works carried out by our group[10] and elsewhere[36-38] have shown that metallic or small-diameter semiconducting tubes are preferentially functionalized. As a consequence of these two considerations, any functionalized SWCNT sample contains tubes bearing different functionalization levels according to the metallic or semiconducting nature of the individual tube as well as according to their position within a bundle.

It is well known that modifications of the SWCNT structure upon covalent functionalization can be evidenced by Raman spectroscopy. Several features are considered as signatures of this. If the degree of functionalization is high enough, the intensity of the D band with respect to that of the G^+ band is expected to increase due to the addition of sidewall defects created by the attachment of functional groups. In our case, the increase of I_D/I_{G+} being as high as a factor of 3 (c.f. Table 1) allows asserting that we have efficiently grafted functions to the sidewalls of the raw samples. Such grafting may also affect the other spectral features through mass and charge transfer effects. Finally, the introduction of grafting-provoked defects may also induce a second disorder-induced band, designated G*, appearing as a high-frequency shoulder of the G band, located at about 1605-1620 cm^{-1}. This disorder-derived band has occasionally been indicated for CNTs[39-41] but has been known for a considerably longer time in less organized carbonaceous materials.[42,43]

10

4.2. *Functionalized SWCNT-based composites.*

We should note that those functionalized tubes integrated into the polymer matrix (SWCNT-PhEster) have undergone two additional steps with respect to the functionalized SWCNT-PhMeO. However, we have previously found[34] that the two additional steps affect only the end groups of the initially-grafted functions and do not have any further effect on the CNTs themselves. As indicated in §3.1, functionalization does not uniformly graft all the individual CNTs within a so-called "functionalized sample": there always remains a mix of functionalized and non-functionalized CNTs and CNT bundles. Thus the D'/G^+ intensity ratio of this sample is actually an average over the different populations.[33] D' is the disorder peak around 1350 cm^{-1} containing PMMA contribution. The experimental I_D/I_{G+} results after subtraction of PMMA contribution to the D-band using the procedure described in detail elsewhere[33] illustrated in Table 1 suggest that in the agglomerated regions of the composite, the fraction of non-functionalized CNTs is higher than in the functionalized CNT sample, i.e. I_D/I_{G+} is greater in the former than in the latter. The I_D/I_{G+} ratio of the dispersed composite region is higher than that of the functionalized sample since the fraction of functionalized tubes in the former is greater than in the latter. It is of interest to note that this behavior is true for both the metallic tubes probed by 1.96 eV excitation energy and for the semiconducting tubes probed by 2.33 eV irradiation.

This observation shows that functionalized SWCNTs are preferentially dispersed in the PMMA matrix as intended while preferentially the non- or lesser-functionalized fraction forms the aggregates.

11

4.3. Heating effects

It is known that the G^+-peak position is sensitive to pressure[18], temperature[14-17], strain[24] or charge transfer[36] and possibly provides information about interactions between CNTs and the polymer host within a composite. However, it was unexpected that a G^+-band downshift was always observed in areas showing a high CNT concentration (c.f. figure 3), i.e. areas with a lower fraction of functionalized CNTs. Logically such areas should show a lower interaction between the CNTs and the polymer matrix. We excluded charge transfer as a possible reason for the observed downshift; pressure was also unlikely to be the reason as a downshift of the G-band would imply a pressure lower than atmospheric. There is no reason here why areas of highly agglomerated CNTs should show pressures lower than those of well dispersed CNT areas. Tensile strain would also lead to a downshift of the CNT G-band but again we find no reason why areas of agglomerated CNTs should experience more tensile strain than well dispersed areas.

There may be one small effect related to the stress imposed by embedding the CNTs in the polymer host. Indeed, the G^+-peak positions of both agglomerated and dispersed areas at the lowest used laser PD are all located between 1589 and 1592.5 cm^{-1} whereas for raw and functionalized tubes the G^+-peak position is located around 1588-1590 cm^{-1}. This small upshift in the composite relative to pure CNT systems could, in agreement with Hadjiev et al. be explained by a small stress applied to the tubes during the curing of the composite.[19]

Figure 4 clearly illustrates that for a given power density, the G^+-frequency downshift is greater for the higher photon energy. Taking into account all the above considerations, we conclude that the greater downshift of agglomerated areas of the composite relative to dispersed areas can be attributed to laser induced heating effects. While equation (1) holds only for pure SWCNT systems, it most probably also provides a rough first estimation in the composites. Examining figure 4 in the light of this equation, we observe that for the given representative samples shown, beyond a power density of 10 or 20 kW/cm^2, the temperature has risen by 200 °C or more and continues to do so as

the PD increases further. This is true in all cases except at 2.33 eV for the agglomerated region within the composite. Here, the decrease in G^+-band frequency is extremely rapid, i.e., the temperature has risen very quickly, well above the melting temperature of PMMA, which is between about 130 °C and 200 °C according to the reference cited and the exact state of the polymer. In all experiments using this excitation energy, the G^+-peak position against laser PD for agglomerates showed leveling (c.f. figure 4) starting at a PD > 10 kW/cm². We explain this by the fact that at the same time ablation of the probed surface was observed which inhibited any further temperature increase and thus any further downshift of the G-band. At the same time, the absolute intensity of the CNT Raman signal went down. A reason could be defocusing resulting from the ablation of material on the surface.

One might question whether functionalization plays a role in CNT heating. From our experimental data it becomes clear that this much higher heating rate in agglomerated regions cannot be due to the functionalization of the CNTs before incorporation in the composite since as-produced and functionalized CNTs show comparable peak shift values (Table 2). Further, if one takes into account that the fraction of functionalized tubes is presumably higher in the dispersed composite area than in the agglomerated area, G^+-peak shift rates should also be higher in the dispersed area if it was due to functionalization. But this is not observed.

Laser-induced heating effects in carbon nanotubes have been noted in several previous works [14,29,30] but much less is known on thermal effects in CNT composite material. Interestingly Kao and Young[28] examined a composite material with an almost equal loading to ours (0.1%) and they employed a He-Ne laser of 633 nm wavelength. They found a lower shift rate of G' band (exhibiting qualitatively similar behaviour to G-band downshift) for the composite than for the pure CNTs and their CNT heating rates are compatible with those of the dispersed composite area in our work.

To the best of our knowledge, such a huge spatial difference in the heating behavior in a composite has never been observed elsewhere. An interesting question is the physical origin of

13

these different heating rates. We propose the following factors. As CNTs are very good light absorbers, one explanation could be the better dispersion and lower concentration of CNTs in the dispersed area which means less absorbers per unit volume resulting in less heating. If, on the other hand, we take into account that CNTs in the dispersed area exhibit a higher fraction of functionalized tubes then they might be expected to be better coupled to the matrix and thus more efficiently dissipate their heat. Thirdly the physical state of the CNTs could also have some effect. It is known that individual CNTs show much better heat dissipation than bundled CNTs. In the composite material, the smaller bundle size or perhaps even the individualized state of some CNTs in the dispersed areas would result in a lower laser heating effect as well. However for the moment we have no quantitative information on the bundle size in the dispersed area. It may well be that all these factors contribute simultaneously to some extent.

14

Conclusions

In this work, we have carried out a resonant Raman spectroscopy study of a composite material made of a PMMA polymer host and functionalized SWCNTs and of the SWCNT material before and after functionalization. Examination of the D/G^+-intensity ratio of the SWCNT material before incorporation into the composite has shown a higher value for functionalized than for the raw SWCNTs. CNT Raman spectra of dispersed areas in the composite manifest a higher D/G^+ intensity ratio than in aglomerated areas and even than in the SWCNT-PhMeO sample indicating that they contain a significant fraction of functionalized CNTs. Functionalized SWCNTs are preferentially situated in the dispersed composite area. All these results underline the importance of functionalization so as to optimize CNT dispersion within the host.

Laser heating gives rise to a significant downshift of the G^+-peak position with increasing power densities. This is attributed to an increase of local temperature, already observable at the lowest laser power densities for 2.33 eV irradiation for agglomerated areas. This effect might possibly lead to Raman data interpretation errors if this downshift was attributed to other effects, for example enhancement of CNT-host interaction in composites. We conclude that laser heating effects generally accompany Raman characterization of CNT-based composite systems as they always exhibit inhomogeneities of nanotube distribution in the matrix. It is therefore very important - especially for CNTs incorporated into a non-thermally or -electrically conductive matrix - to use a laser power density as low as possible and monitor position of G^+ peak vs laser power density on the irradiated sample surface. As our work has shown, in those areas of a composite in which there is some level of aggregation, the heating effects are even greater and may lead even to polymer ablation. Laser ablation of the material (PMMA) via CNT heat absorbers can be used for patterning of PMMA (or other polymer) matrix with micron resolution for different applications, for example, manufacturing microfluidic systems.

15

Possible explanations of the agglomerated CNT heating have been proposed but certainly further work is required to answer some of the still-open questions.

Acknowledgments

16

Figure Captions.

Figure 1. Raman spectra for raw SWCNT (upper panels) and SWCNT-PhMeO (lower panels) for the two used laser energies.

Figure 2. Raman spectra of composite agglomerated (a and b) and dispersed areas before (c and d) and after subtraction of the PMMA Raman contribution (e and f).

Figure 3. Raman maps of 0,097 wt% composite: a) plot of G^+-intensities illustrating spatial distribution of CNTs. b) plot of G^+-peak position illustrating spatial distribution of peak shift.

Figure 4. Results of representative laser heating experiments. Symbol assignment: raw CNTs – full squares, functionalized CNTs – open circles, composite aggregates – full left pointing triangles, composite dispersed area 1 – up-pointing half filled triangles, composite dispersed area 2 – down-pointing half filled triangles.

Figure 5. a) Raman spectra (2.33 eV) for agglomerate (1) and two different spots in dispersed area (2, 3). (b) Illustration of the correlation between the absolute Raman intensity and downshift of the G-band.

Figure 6. Raman spectra collected from a probed spot for increasing laser power densities (left panel); area of probed spot before and after the experiment showing the ablation mark at the laser spot position (right panel).
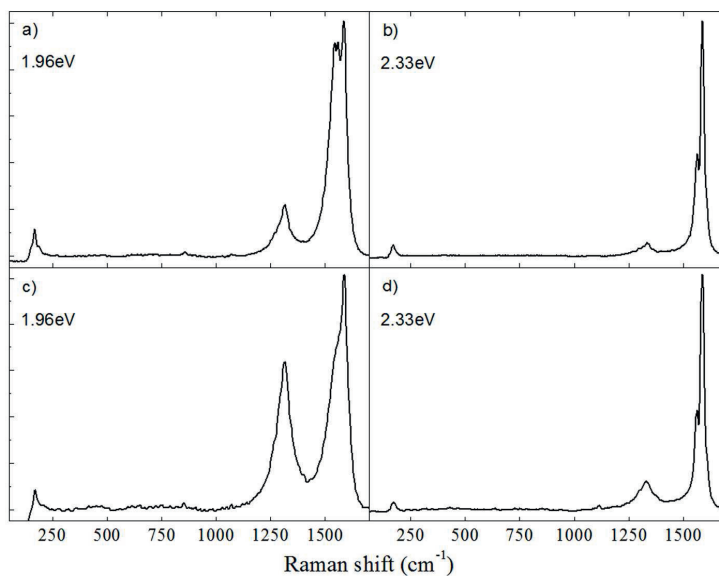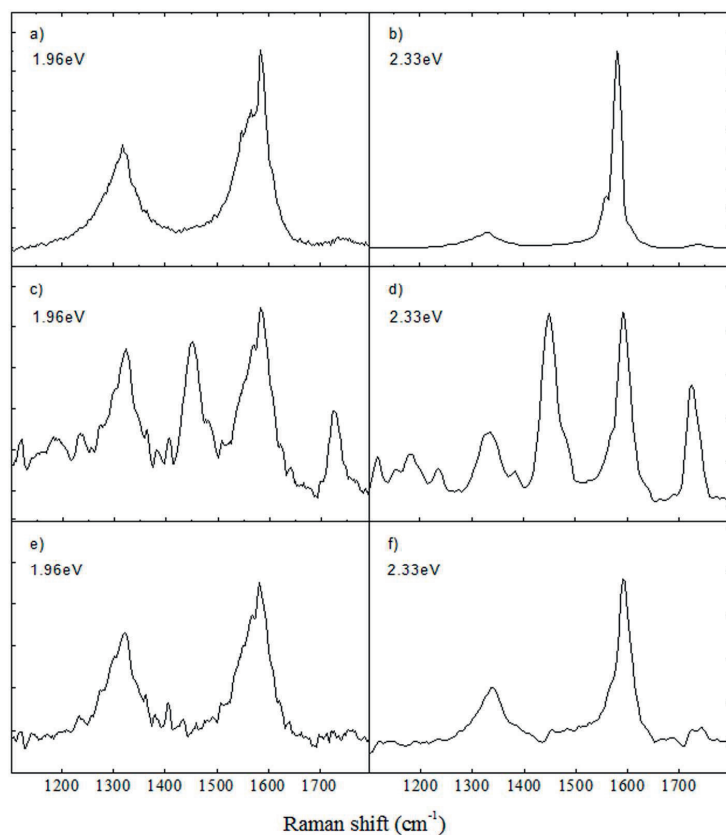
17

1
2
3
4
5
6
7
8
9
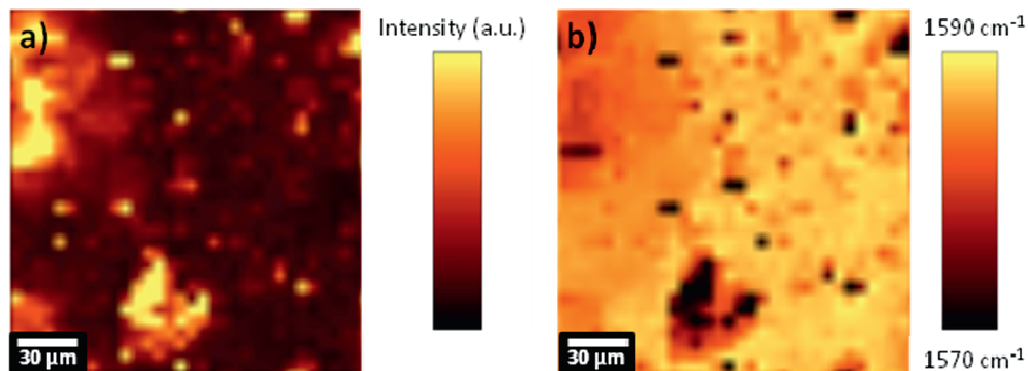10
11
12
13
14
15
16
17
18
19
20
21
22
23
24
25
26
27
28
29
30
31
32
33
34
35
36
37
38
39
40
41
42
43
44
45
46
47
48
49
50
51
52
53
54
55
56
57
58
59
60

Figure 1

1
2
3
4
5
6
7
8
9
10
11
12
13
14
15
16
17
18
19
20
21
22
23
24
25
26
27
28
29
30
31
32
33
34
35
36
37
38
39
40
41
42
43
44
45
46
47
48
49
50
51
52
53
54
55
56
57
58
59
60

Figure 2
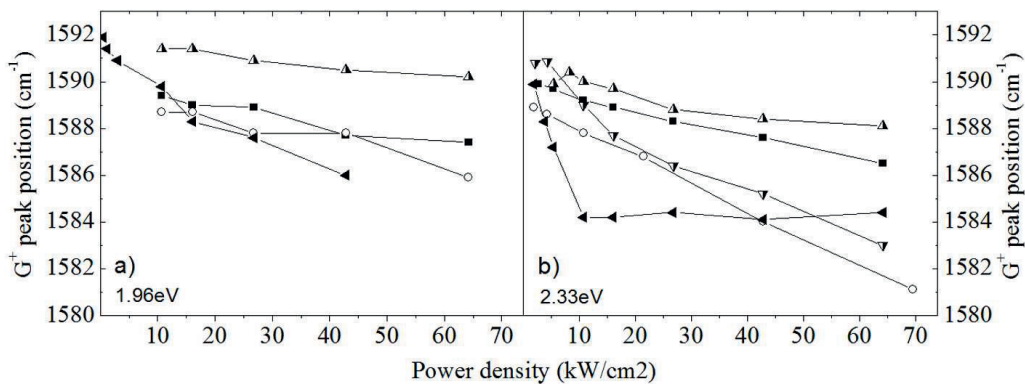
Figure 3
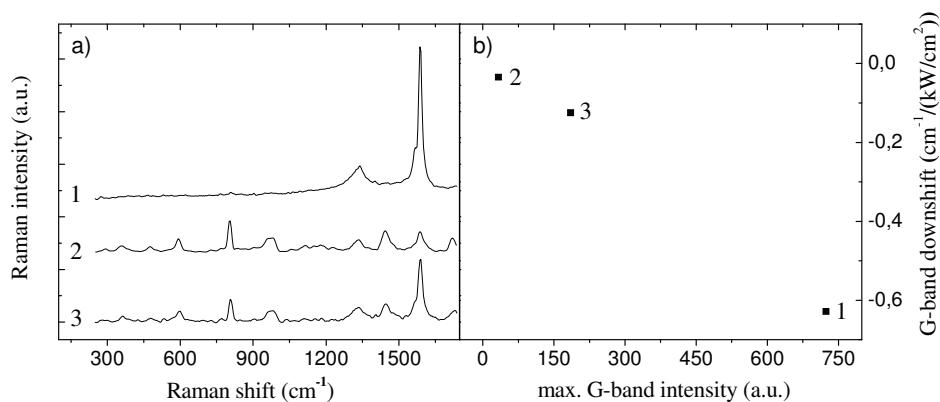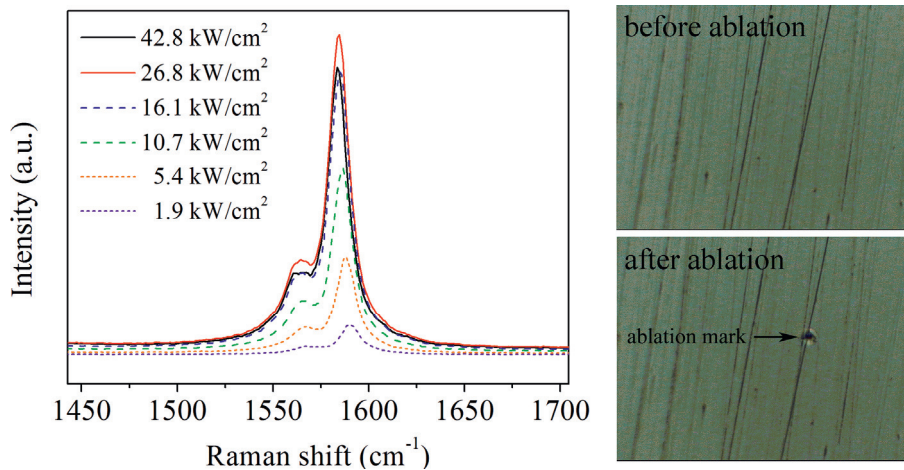
Figure 4

Figure 5

21

Figure 6

Tables.

Table 1: Average D/G$^+$ integrated peak intensity ratios of investigated systems for 2.33 and 1.96 eV excitation energies (PMMA contribution to the D-band peak was subtracted).

Table 2: Laser heating effect observed in different investigated systems for 1.96 and 2.33 eV excitation energies.

Table 1

D/G$^+$ intensity ratios for SWCNT systems	as-produced Carbolex	SWCNT-PhMeO	composite agglomerated area	composite dispersed area
2.33 eV	0.38	1.41	0.52	1.84
1.96 eV	1.23	3.68	2.02	3.90

Table 2

SWCNT systems	2.33 eV		1.96 eV	
	G$^+$-shift rate [cm^{-1}/ (kW/cm^2)]	heating rate [K/ (kW/cm^2)]	G$^+$-shift rate [cm^{-1}/ (kW/cm^2)]	heating rate [K/ (kW/cm^2)]
as-produced Carbolex	-0.077	2.98	-0.055	2.13
SWCNT-PhMeO	-0.127	4.92	-0.06	2.33
composite agglomerated area	-0.578	22.40	-0.089	3.45
composite dispersed area	-0.125	4.84	-0.031	1.20

References

[1] Byrne N. T.; Gun'ko Y. K. *Adv. Mater.* **2010**, *22*, 1672.

[2] Eder D. *Chem. Rev.* **2010**, *110*, 1348.

[3] Shokrieh M. M.; Rafiee R. *Mech. Comp. Mat.* **2010**, *46*, 155.

[4] Spitalsky Z.; Tasis D.; Papagelis K.; Galiotis C. *Prog. Poly. Sci.* **2010**, *35*, 357.

[5] Chou T. W.; Gao L.; Thorstenson E. T.; Zhang Z.; Byun J. H. *Comp. Sci. Tech.* **2010**, *70*, 1.

[6] Sahoo N. G.; Rana S.; Cho J. W.; Li L.; Chan S. H. *Prog. Poly. Sci.* **2010**, *35*, 837.

[7] Roy D.; Bhattacharyya S.; Rachamim A.; Plati A.; Saboungi M. L. *J. Appl. Phys.* **2010**, *107*, 043501.

[8] So H. H.; Cho. J. W.; Sahoo N. G. *Eur. Polym. J.* **2007**, *43*, 3750.

[9] Zhu B.-K.; Xie S.-H.; Xu Z.-K.; Xu Y.-Y. *Comp. Sci. Tech.* **2006**, *66*, 548.

[10] Liu J.; Dossot M.; Olevik D.; Mamane V.; Vigolo B.; Abrahamsson D.; Jonsson H.; Fort Y.; Humbert B.; Soldatov A.V.; McRae E. *Physica E* **2008**, *40*, 2343.

[11] Graupner R. *J. Raman Spectr.* **2007**, *38*, 673.

[12] Holzinger M.; Abraham J.; Whelan P.; Graupner R.; Ley L.; Hennrich F.; Kappes M.; Krisch A. *J. Am. Chem. Soc.* **2003**, *125*, 8566.

[13] Raravikar N. R.; Keblinski P.; Rao A. M.; Dresselhaus M. S.; Schadler L. S.; Ajayan P. M. *Phys. Rev. B* **2002**, *66*, 235424.

[14] Zhang Y.; Xie L.; Zhang J.; Wu Z.; Liu Z. *J. Phys. Chem. C* **2007**, *111*, 14031.

[15] Zhang Y.; Son H.; Zhang J.; Kong J.; Liu Z. *J. Phys. Chem. C* **2007**, *111*, 1988.

[16] Huang F.; Yue K. T.; Tan P.; Zhang S.-L.; Shi Z.; Zhou X.; Gu Z. *J. Appl. Phys.* **1998**, *84*, 4022.

[17] Venkateswaran U. D.; Brandsen E. A.; Schlecht U.; Rao A. M.; Richter E.; Loa I.; Syassen K.; Eklund P. C. *Phys. Stat. Sol. (b)* **2001**, *223*, 225.

[18] Cronin S. B.; Swan A. K.; Ünlü M. S.; Goldberg B. B.; Dresselhaus M. S.; Tinkham M. *Phys. Rev. B* **2005**, *72*, 035425.

[19] Hadjiev V. G.; Iliev M. N.; Arepalli S.; Nikolaev P.; Files B. S. *Appl. Phys. Lett.* **2001**, *78*, 21.

[20] Chang T.-E.; Kisliuk A.; Rhodes S. M.; Brittain W. J.; Sokolov A. P. *Polymer* **2006**, *47*, 7740.

[21] Wang S.; Liang R.; Wang B.; Zhang C. *Chem. Phys. Lett.* **2008**, *458*, 371.

[22] Kalbác M.; Kavan L.; Dunsch L. *Comp. Sci. Tech.* **2009**, *69*, 1553.

[23] Thomson K. E.; Jiang D.; Ritchie R. O.; Mukherjee A. K. *Appl. Phys. A* **2007**, *89*, 651.

[24] Bassil A.; Puech P.; Landa G.; Bacsa W.; Barrau S.; Demont P.; Lacabanne C.; Perez E.; Bacsa R.; Flahaut E.; Peigney A.; Laurent C. *J. Appl. Phys.* **2005**, *97*, 34303.

[25] Lamy de la Chapelle M.; Stephan C.; Nguyena T. P.; Lefiant S.; Journet C.; Bernier P.; Munoz E.; Benito A.; Maser W. K.; Martinez M.; de la Fuente G. F.; Guillard T.; Flamant G.; Alvarez L.; Laplaze D. *Syn. Met.* **1999**, *103*, 2510.

[26] Zhao Q.; Wagner H. D. *Phil. Trans. R. Soc. Lond. A* **2004**, *362*, 2407.

[27] Baibarac M.; Baltog I.; Lefrant S. *Carbon* **2009**, *47*, 1389.

[28] Kao C. C.; Young R. J. *Comp. Sci. Tech.* **2004**, *64*, 2291.

[29] Maehashi K.; Onno Y.; Inoue K.; Matsumoto K. *Appl. Phys. Lett* **2004**, *85*, 858.

[30] Huang H.; Maruyama R.; Noda K.; Kajiura H.; Kadono K. *J. Phys. Chem. B* **2006**, *110*, 7346.

[31] Vigolo B.; Mamane V.; Valsaque F.; Ha Le T. N.; Thabit J.; Ghanbaja J.; Aranda L.; Fort Y.; McRae E. *Carbon* **2009**, *47*, 411.

[32] Vigolo B.; Vincent B.; Eschbach J.; Bourson P.; Marêché J.-F.; McRae E.; Müller A.; Soldatov A.; Hiver J.-M.; Dahoun A.; Rouxel D. *J. Phys. Chem. C* **2009**, *113*, 17648.

[33] Mueller A.; Vigolo B.; McRae E.; Soldatov A. *Phys. Stat. Sol. (b)* **2010**, *247*, 2810.

[34] Dossot M.; Gardien F.; Mamane V.; Fort Y. ; Liu J.; Vigolo B.; Humbert B.; McRae E. *J. Phys. Chem. C* **2007**, *111*, 12199.

[35] Olevik D.; Soldatov A. V.; Dossot M.; Vigolo B.; Humbert B.; McRae E. *Phys. Stat. Sol. (b)* **2008**, *245*, 2212.

[36] Alvarez N. T.; Kittrell C.; Schmidt H. K.; Hauge R. H.; Engel P. S.; Tour J. M. *J. Am. Chem. Soc.* **2008**, *130*, 1422733.

[37] Joselevich E. *ChemPhysChem* **2004**, *5*, 619.

[38] Wang C.; Cao Q.; Ozel T.; Gaur A.; Rogers J. A.; Shim M. *J. Am. Chem. Soc.* **2005**, *127*, 11460.

[39] Cataldo, F. *Carbon* **2000**, *38*, 623.

[40] Kim, U. J.; Furtado, C. A.; Liu, X.; Chen, G.; Eklund, P. C. *J. Am. Chem. Soc.* **2005**, *127*, 15437.

[41] Mases M.; Noël M.; Mercier G.; Dossot M.; Vigolo B.; Mamane V.; Fort Y.; Soldatov A. V.;

McRae E. *Phys. Stat. Sol. (b)* **2011**, http://dx.doi.org/10.1002/pssb.201100082.

[42] Beyssac O.; Goffe, B.; Petitet J.-P.; Froigneux E.; Moreau M.; Rouzaud J.-N. *Spectrochim. Acta, Part A* **2003**, *59*, 2267.

[43] Sze S.-K.; Siddique N.; Sloan J.J.; Escribano R. *Atmos. Environ.* **2001**, *35*, 561.